DEVELOPMENT OF 3D PRINTED ENZYMATIC BIOFUEL CELLS FOR POWERING IMPLANTABLE BIOMEDICAL DEVICES

PhD thesis

BY KEYVAN JODEIRI

Submitted to the University of Nottingham

for the degree of Doctor of Philosophy,

March 2023

Abstract

The drive toward device miniaturisation in the field of enzyme-based bioelectronics established a need for multi-dimensional geometrically structured and highly effective microelectrodes, which are difficult to implement and manufacture in devices such as biofuel cells and sensors. Additive manufacturing coupled with electroless metal plating enables the production of three-dimensional (3D) conductive microarchitectures with high surface area for potential applications in such devices. However, interfacial delamination between the metal layer and the polymer structure is a major reliability concern, which results in device performance degradation and eventually device failure.

This thesis demonstrates a method to produce a highly conductive and robust metal layer on a 3D printed polymer microstructure with strong adhesion by introducing an interfacial adhesion layer. Prior to 3D printing, multifunctional acrylate monomers with alkoxysilane ($-Si-(OCH_3)_3$) were synthesised via the Thiol-Michael addition reaction between pentaerythritol tetraacrylate (PETA) and 3-mercaptopropyltrimethoxysilane (MPTMS) with a 1:1 stoichiometric ratio. Alkoxysilane functionality remains intact during photopolymerisation in a projection micro-stereolithography (PµSLA) system and is utilised for the sol-gel reaction with MPTMS post-functionalisation of the 3D printed microstructure to build an interfacial adhesion layer. This functionalisation leads to the implementation of abundant thiol functional groups on the surface of the 3D printed microstructure, which can act as a strong binding site for gold during electroless plating to improve interfacial adhesion.

The 3D conductive microelectrode prepared by this technique exhibited excellent conductivity of 2.2×10^7 S/m (53% of bulk gold) with strong adhesion between a gold layer and a polymer structure even after harsh sonication and adhesion tape test, which offers potential to build a robust 3D conductive microarchitecture for applications such as biosensors and biofuel cells.

As a proof-of-concept, the microelectrode with gold-coated complex lattice geometry was employed as an enzymatic glucose anode, which showed a significant increase in the current output compared to the one in the simple cube form. As the first approach, glucose oxidase was used as an enzyme. To find the optimal protocol for the enzyme immobilisation, the enzyme was first immobilised on agarose to achieve the enzyme's highest activity and stability. Then, this immobilisation protocol was applied to immobilise the enzyme on the gold electrode surface. Preliminary studies on the preparation of 3D gold diamond lattice microelectrode modified with cysteamine and glucose oxidase as a bioanode for single cell enzymatic biofuel cell (EFC) application were performed, which demonstrated high current density of 0.38 $\mu A\ cm^{-2}$ at 0.35 V in glucose solutions.

This method for fabrication of 3D conductive microelectrodes offers potential for several biological applications. Instead of using a thiol, the surface of the 3D-printed part can be functionalised with different other functional groups to create an appropriate surface for biomolecules and cell adhesion. Furthermore, the surface of thiol functionalised printed parts can be perfect for additional metal coatings, opening

the door to the creation of highly efficient and customised implantable energy harvesters and biosensors.

List of Publications, conferences, and awards

Published paper.

- **Keyvan Jodeiri**, Aleksandra Foerster, Gustavo F. Trindade, Jisun Im, Diego Carballares, Roberto Fernández-Lafuente, Marcos Pita, Antonio L. De Lacey, Christopher D. Parmenter, and Christopher Tuck. "Additively Manufactured 3D Micro-bioelectrodes for Enhanced Bioelectrocatalytic Operation." *ACS Applied Materials & Interfaces* (2023).

Conference presentation

Oral presentations

- **K. Jodeiri**, A. Foerster, Jisun Im, C. Tuck. 3D-printing of highly conductive microelectrodes for implantable electronic devices; Royal Australian Chemical Institute (RACI) Congress. Brisbane, Australia

- **K. Jodeiri**, A. Foerster, Jisun Im, C. Tuck. Surface Functionalisation and Electroless Plating Of 3D-Printed Microstructures; 241st Electrochemical Society (ECS) Meeting, Vancouver, BC, Canada

Poster presentation

- **K. Jodeiri**, A. Foerster, Jisun Im, C. Tuck. IEEE sensors 2021. An Effective Approach For 3D-Printing High-Surface-Area Microelectrodes.; Virtual Conference

- **K. Jodeiri**, A. Foerster, Jisun Im, C. Tuck. 31st Anniversary World Congress on Biosensors; Development of 3D microelectrodes using a combination of micro-stereolithography and electroless gold plating techniques; Virtual Conference

Award

- Engineering award winner in the Young Entrepreneurs Scheme (YES20) competition.

Acknowledgments

I am pleased to present my PhD thesis, and I am grateful for the support and assistance of many individuals who have made this achievement possible. First and foremost, I would like to express my heartfelt gratitude to my parents, who have given up so much to ensure that I received the best possible education and supported me unconditionally in every stage of my life. Their unwavering love, encouragement, and sacrifices have been the foundation of my success, and I am forever grateful.

I would like to express my sincere gratitude and appreciation to my supervisors, Aleksandra Foerster, Jisun Im, and Christopher Tuck, for their invaluable support and guidance during my research. Their expertise, patience, and unwavering commitment to my academic journey have been instrumental in helping me achieve my goals. Their timely and insightful feedback, as well as their willingness to answer my questions and address any challenges that arose, were essential in shaping the direction and outcomes of my research. I am truly fortunate to have had such dedicated and supportive mentors, and I am deeply grateful for their contributions to my success. Finally, I would like to acknowledge my dear friends and colleagues, Arielle Torres, Eric Lehder, Farzaneh Sameni, Negar Gilani, Nerea Bejar-Munoz, Richard Woods, and Shreeja Basak who have become my second family during my academic journey. Their support, encouragement, and humour have made my life enjoyable, and I am grateful for their friendship. Once again, thank you to everyone who has contributed to my academic success. I could not have achieved this milestone without your support, and I will forever cherish your kindness and generosity.

Table of content

List of Figures

List of acronyms

2PP	Two-Photon Photopolymerisation
3D	Three Dimensional
AM	Additive Manufacturing
BJ	Binder Jetting
CAD	Computer Aid Analysis
CFD	Computational Fluid Dynamics
CNTs	Carbon Nano-Tubes
CV	Cyclic Voltammetry
DET	Direct Electron Transfer
DLP	Digital Light Processing
DP	Degree Of Polymerisation
EFCs	Enzymatic Biofuel Cells
FIB	Focused Ion Beam
FTIR	Fourier Transform Infrared Spectroscopy
GA	Glutaraldehyde
GOx	Glucose Oxidase
MET	Mediated Electron Transfer
MP	Functionalised Monomer
MPTMS	3-Mercaptopropyltrimethoxysilane
NMR	Nuclear Magnetic Resonance Spectroscopy
OP	Over Polymerisation
PµSLA	Projection Micro-Stereolithography
PBS	Phosphate Buffered Saline
PETTA	Pentaerythritol Tetraacrylate
SEM	Scanning Electron Microscope Analysis
SLA	Stereolithography
SLM	Selective Laser Melting
SLS	Selective Laser Sintering
ToF-SIMS	Time-Of-Flight Secondary Ion Mass Spectrometry
UV	Ultraviolet
UV-Vis	Ultraviolet-Visible
VP	Vat Photopolymerisation
XPS	X-Ray Photoelectron Spectroscopy

1. Introduction

1.1. Motivation

Artificial cardiac pacemakers rescue lives and increase the quality of life. 1.25 Million permanent pacemakers are implanted globally each year, making pacemakers the most prevalent active implantable medical device.[1] Nevertheless, due to the low capacity of the implant's battery, their frequent replacement is required. Moreover, the associated surgery is often painful and causes stress to the patients. Enzymatic biofuel cells (EFCs) have been considered a possible solution to this problem since they can generate complementary electrical energy directly from the human body with the advantage of long-life performance and high electrical efficiency. Moreover, EFCs can contribute to developing implantable electronic medical devices, such as artificial organs that require large amounts of energy to function. The system can aid millions of patients worldwide suffering from serious diseases such as bradycardia, fibrillation, or diabetes.[2,3]

Typical fuel cell electrocatalysts operate between 45 and 150 °C and are made of conductive metal. These catalysts are stable and work well in acidic or basic environments. Nevertheless, they have problems with passivation and need simple fuels with high purity, like hydrogen and methanol. On the other hand, biocatalysts (enzymes) can eat and break down complex fuels (such as sucrose, fructose, etc.), and fuel blends and their catalysts do not have the same problems. Because of this, the field of enzymatic biofuel cells has evolved significantly in the last 30 years. It enables them to be used in places where traditional metal nanoparticle electrocatalysts cannot be used, such as in implantable fuel cells and biosensors. An enzyme-based

biofuel cell (EFC) is a fuel cell that uses enzymes as electrocatalysts to speed up fuel oxidation and/or the reduction of oxygen or peroxide. This turns chemical energy, like glucose, into electricity. The EFCs that use immobilised enzyme on the electrode provide a membrane-free arrangement of EFCs, opening the door for the development of electrochemical biosensors that can function without a power source and tiny power supply systems for implantable electronic devices.

1.2. Challenges with current enzymatic biofuel cells

Miniature membrane-less EFCs are anticipated to be used in implantable medical devices such as insulin pumps, hearing aids, bone stimulators, and pacemakers in the future. They may also be used as self-powered biosensors that can determine the concentration of an analyte while also supplying themselves with energy. Various compounds that cause heart disease, cancer, and blood sugar could be measured using implanted self-powered biosensors. EFCs must meet certain requirements to be used for these purposes, including being portable and lightweight, operating at body temperature, pH, and salt concentration, as well as producing adequate energy and maintaining good operational stability. Therefore, creating high-performance EFCs is still necessary due to inadequate power output, voltage output, and operational stability. These three technological challenges must be overcome to get the reliable EFCs:

1. The EFCs should have an optimum 3D structure. The smaller pores on the three-dimensional bioanode should provide enough surface area for the reaction that generates current, whilst the bigger pores often enable better mass movement.

2. Most EFCs have a much shorter lifetime than conventional lithium-ion batteries for powering pacemakers. It is therefore important that the enzyme is effectively stabilised on the electrode, so that the EFCs' lifetime can increase, reducing the need to replace them frequently.

3. The anode must support an effective electron transfer method, whether it be mediated or direct electron transfer. Therefore, understanding the relationship between porosity for fuel delivery, surface area for optimum enzyme loading, and electrical conductivity for lowering ohmic losses is crucial.

1.3.   Current state of the art

Over the past decade, the performance of EFCs has substantially increased due to the use of various nanomaterials such as carbon nanotubes (CNTs), graphene oxide (GO), noble metal nanoparticles, and conjugated polymers. These materials often have a large surface area, acceptable electrical conductivity, and biocompatibility. Their application boosts electrical signal generation and electron transfer efficiency and often offers a stable matrix for enzyme immobilisation. Nanomaterials' high surface area enables them to increase enzyme loading, enhancing the stability and activity of immobilised enzymes and boosting EFCs' efficiency. However, the main issue with the nanomaterials-based EFCs is the mass transport, which primarily affects the efficiency of the EFCs. Additionally, compared to bulk metal electrodes used in typical applications, electrodes built from nanomaterials have low conductivity due to the discreet nanoparticle formation inside the electrode. This poor conductivity will eventually cause a reduction in the electron transfer between the enzyme and

electrode. Even if the electron transfers to the nanomaterial-based electrode, it loses much energy while transferring from the electrode to the current collector. Therefore, comprehensive studies are required to enhance the catalytic surface area of the electrode, increase the mass transport within the electrode, enzyme immobilisation on the electrode, increase the lifetime of the immobilised enzyme and enhance the electron transfer between enzymes and electrode. Conducting a thorough study to adjust the conductivity and form of the electrode may be able to tackle this problem by improving the flowability of the fuel with the enzymatic electrode and the electron transfer.

1.4.   Scope of research

Although significant progress has been made to improve the performance of the EFCs (electrode modification with carbon nanotubes,[4] mesoporous materials,[5] nanoparticles,[6] conductive polymers,[7] or enzyme engineering [8]), more developments in EFCs' power density, stability, and miniaturisation are required, especially when considering their use for powering implantable medical devices. The smaller the biofuel cells involved; the lower amounts of available active electrode materials will lessen the total power density. The key to addressing the challenges is to focus on three main aspects of the EFCs:

1. **Additive manufacturing of 3D microelectrode:**

The high porosity of the electrode is required to accommodate more enzymes and provide a higher catalytic surface area. However, the excess small pores within the material create a barrier that slows down the movement of gases and liquids,

making it difficult for fuel to pass through.. Therefore, careful investigation is required to optimise the pore size and geometry of the electrode. Optimising the EFC geometry can be challenging because of the limitation of the conventional manufacturing techniques in fabricating complex structures. Additive manufacturing (AM) allows the fabrication of complex 3D geometry with control of porosity and surface area. In particular, the Vat-photopolymerisation technique can be beneficial as it can fabricate micro-sized 3D architectures with high surface area. It can offer opportunities to maximise power density and reduce the mass transport distances between the electrodes.[9] In this study, functional monomers were synthesised for 3D printing and successful metal deposition. Ink formulation and printing process were optimised to achieve the highest resolution of the printed structures.

2. Improve the conductivity of the electrode:

Two-photon polymerisation is a nanoscale vat photopolymerisation technique with a resolution of about 100 nm.[10,11] Despite the submicrometer printing accuracy, the challenge in the production of highly conductive 3D-microelectrodes still exists. To address the issue of low conductivity, alternative two-step methods for coating the VP printed polymer with metal have been investigated; however, due to poor surface adhesion, the conductivity is significantly lower than that of their bulk counterpart, and the deposited metal have been shown to peel from the substrate. To solve this problem, I have undertaken research on the printing of 3D-polymeric microstructures that can be post-functionalised and gold-coated effectively. To achieve this, the impact of surface functionalisation on coating adhesion and conductivity has been

thoroughly studied. This strategy may make it possible to connect other metals via increased surface functionalisation for several applications, including as microelectronics and catalysts.

3. Optimise the enzyme immobilisation.

The enzyme's immobilisation is a critical part of the EFC's efficiency. Proper enzyme immobilisation can increase enzyme activity, stability, and electron transfer between the electrode and the enzyme. Therefore, the effects of immobilisation procedures on the stability of the immobilised enzyme have been thoroughly examined. As a proof of concept, glucose was immobilised on the gold electrode using the optimised enzyme immobilisation procedure for application in enzymatic biofuel cells. This strategy can enable AM to improve the EFC's effectiveness and customise them according to the implantation.

1.5.   Aim and objectives

This research aims to create 3D miniaturised bio-anodes with various geometry to enhance the current output of EFCs. This work can be broken down into three main tasks with their respective objectives:

- Preparation of highly conductive 3D electrodes

    o Design suitable 3D structures

    o Fabricate 3D polymeric structures using PµSLA

    o Functionalise and characterise the surface of 3D printed polymeric structures with thiol groups

- o Optimise the electroless plating process on the surface of the 3D polymeric structures to achieve high conductivity

- o Characterise conductive surfaces

- Immobilisation and characterisation of the enzyme on the electrode surface in an optimal form

- o Functionalise the surface of the gold 3D microstructure

- o Immobilise the enzyme on the surface of the gold 3D microstructure

- o Characterise the enzyme attachment and stability

- Demonstration of bio-anode

- o Integrate electrodes within the testing device

- o Test catalytic properties of immobilised enzymes

- o Measure the current density of the bio-anode

1.6.   Research novelty and contribution to existing knowledge

To create an enzymatic biofuel cell, in the first step, the enzymes should be immobilised on the current collector to transfer the electron from enzyme to external circuit. To improve the amount of immobilised enzyme and the power density of the EFC, most scientists have employed conductive nanomaterials as a current collector as the nanomaterials provide high surface area per volume ratio. However, these nanomaterials have some issues such as less efficient mass transport, lower conductivity, and poor biocompatibility. These problems can be resolved by effective use of AM in creating of the EFCs as it can provide design freedom to control the size and shape of the pores and create parts with a large surface area. The vat-photopolymerisation method can produce precise 3D printed geometries with submicrometric resolution, which is great for creating microstructured current collectors with high surface areas. VP-based 3D printers can be divided into two main categories of UV-based and 2PP. The UV-based stereolithography methods can produce bigger components with a few micrometre precision, while two-photon photopolymerisation (2PP) can print parts from the nanoscale to few millimetres. However, this technique is not known for printing conductive materials. There have been attempts to increase the conductivity of the polymer matrix by adding conductive nanoparticles as a filler; however, this method produces printed parts with poor mechanical properties, low resolution, and limited conductivity. Considerable work has been done to prepare the surface of 3D printed polymers for coating, but, the problem of poor metal adherence and low conductivity still exists, making it

difficult to employ these materials as trustworthy microelectrodes. It has been shown that the silanisation of the substrate is a facile way to create the appropriate surface for metal deposition in order to create a strong chemical interaction between the polymer and the deposited metal. However, following knowledge gaps is still exists: First of all, there is no literature on the impact of silanisation on the conductivity and adhesion of metal coatings on 3D-printed parts. Second, no studies have been conducted on designing three-dimensional printable micro-EFCs and examining how the geometry influences their current production. This PhD research has investigated an optimal reaction condition to silanise the surface of the 3D printed microstructure, to enhance the adhesion and conductivity of the deposited metal.

For use in an EFC, the enzyme must be immobilised on the 3D printed electrode. An electrode cannot be used effectively in an EFC unless enzyme immobilisation is tuned for the enzyme stability and performance. So that, it is advised to test the enzyme immobilisation in Agarose. Various activation protocols can be used to investigate the effects of immobilisation on this support, and the protocol can then be extrapolated to the 3D-printed gold electrode. Afterwards, the electrode can be turned into a bioanode and evaluated using cyclic voltammetry to compare it with standard flat electrode.

1.7.   Thesis structure

Chapter 2: The section of "Literature review" offers a detailed analysis of the relevant literature for this topic. Enzymatic biofuel cells are discussed in the context of their background and short history. The methods used to increase the effectiveness

of enzymatic biofuel cells are reviewed after it. The evolution of printing microelectrodes using seven distinct AM processes is explained. More attention was paid to the vat-photopolymerisation approach in both direct and indirect printing of electronics. Several polymer surface functionalisation techniques and various metal coating methods have been explained. Then, the effect of the enzyme immobilisation strategy on the effectiveness of the EFC was addressed. The knowledge gaps in the literature are finally summarised.

Chapter 3: "Research Methodology" section explains the research methodology, which includes materials, equipment, methods, and characterisation techniques employed in this study.

Chapter 4 describes the optimisation of Inks formulation and 3D-printing of functional polymers using PµSLA technique. Furthermore, the effect of ink additives on printability is investigated.

Chapter 5: The methodology of surface modification of printed microstructures and gold-coating being explained in the "Surface functionalisation and electroless gold plating" section. The methods for surface characterisation used to investigate the impact of surface functionalisation on the conductivity and adhesion of gold layer deposited on 3D printed polymer structure are thoroughly explained in this chapter.

Chapter 6: To obtain the highest enzyme activity and stability on the 3D-printed gold electrode, "Enzyme immobilisation" section covers the technique utilised to optimise the enzyme immobilisation. The process used to create and characterise the

bioanode is described in "Electrocatalytic characterisation of EFC". Additive manufacturing of bioelectrodes with different geometries is demonstrated This chapter describes the effects of three distinct bioanode geometries on their power output.

Chapter 7: The thesis "Discussion" part delves into the research's significance, draws comparisons to related literature, and emphasises the research significant contribution.

Chapter 8: The section titled "Conclusion and recommendation for future work" summarises the thesis' key results, explains how the objectives were met, and what can be done in future work to exploit this research further.

CHAPTER 2

2. Literature review

2.1.   Enzymatic biofuel cells

Due to its remarkable efficiency in converting chemical energy to electricity without pollution, fuel cells are considered the source of future energy.[12,13] Fuel cells and batteries have similar physical architecture, where electrical energy is created via electrochemical reactions between fuel and oxidant. Ions are moved in the electrolyte by an anode and a cathode in both cases along with the field line. However, the main difference between fuel cells and batteries is the source of energy. Batteries are self-contained and use stored energy from chemical reactions, while fuel cells use an external source of fuel and oxygen to generate electricity. In contrast to batteries, fuel cells can provide electricity if fuel is available. At the anode, oxidised fuel (primarily hydrogen) creates electrons and protons. Electrons create a current in an external circuit. A cathodic reduction occurs when oxygen travels to the cathode and combines with produced hydrogen ions to form water. This technique produces high current densities with the appropriate catalysts. Enzymatic biofuel cells (EFCs) employ enzymes as electrocatalysts to increase fuel oxidation and/or oxygen or peroxide reduction. EFCs are more sophisticated than ordinary fuel cells Fig. 1.
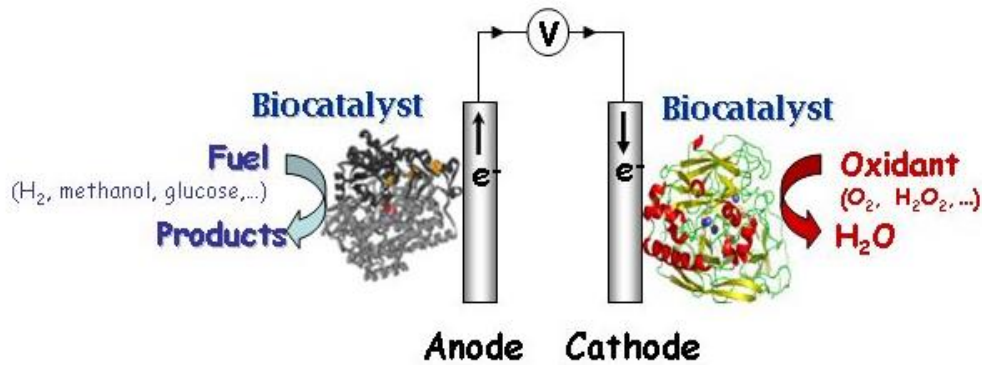
Fig. 1 Working principle of EFCs.[14] In these cells, the fuel, such as glucose or ethanol, is oxidized at the anode by the enzyme, releasing electrons and protons. Electrons flow through an external circuit, generating electrical current. The protons combine with oxygen at the cathode, producing water as a byproduct.

The most promising advantage of biocatalysts is those that effectively catalyse specific reactions under moderate circumstances and create reaction products that are typically acceptable to the host organism. All these features make the enzymes attractive for fuel cells [15]. EFCs generate energy by oxidising fuel at an enzyme-immobilised bio-anode, which delivers electrons to external circuits. At the bio-cathode, four-electron oxygen reduction produces water (Fig. 1). This reaction produces two molecules of water, as well as energy in the form of electricity:

Glucose oxidation reaction at the anode: Glucose + O_2 ➜ Gluconolactone + H^+ + e^-

Oxygen reduction reaction at the cathode: O_2 + 4 H^+ + 4e^- ➜ 2 H_2O
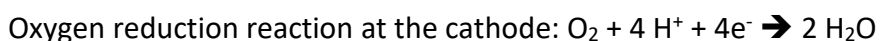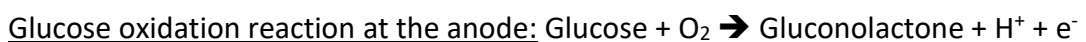
2.2.   EFCs background

The first microbial biofuel cell in 1931, by discovering the possibility of generating electricity by cultivating the bacteria.[16,17] Then this technology attract the attention of scientist from NASA, aiming to produce electricity from human waste in

space crafts. Yahiro et al.[18] (1964) were the first group to discover the idea of EFCs by reporting the ability of enzyme to catalyse the reaction of fuel cells in the presence of mediator. A decade later, Berezin et al.[19] (1978) made a significant contribution to the preparation of biocompatible EFCs by inventing the concept of direct electron transfer (DET). The DET-based bio-electrocatalysis does not require toxic mediators and can directly transfer the electron from the enzyme to the electrode.[20–22] This method allows for miniaturisation, biocompatibility, and easy production of EFCs. Low power density and limited lifespan were disadvantages of early DET-based EFCs. In the past two decades, several researchers have optimised the electrode material, enzyme immobilisation process, and enzyme efficiency to enhance the power density and employ EFCs as an implantable power source. Heller et al.[23] implanted the first EFCs in 2003, proving their viability. They obtained a power density of 2.4 $\mu W/mm^2$ by developing their miniature (7 μm $\times$ 2 cm) glucose-oxygen biofuel cell, comprised of two enzyme-coated carbon fibres, in a grape for a day. Cinquin et al.[24] (2010) demonstrated the first GOx-based EFCs implanted in an animal (rat) body in 40 days. The device was bigger but allowed a higher power density of 24.4 mW/mL, which was enough for powering pacemakers. They prepared it by immobilising glucose oxidase (GOx) and catalase on barium alginate beads and wrapping it with a dialysis tube. Halámková et al. and Szczupak et al.[25,26] (2012) were two groups using different enzyme immobilisation techniques to improve EFC stability and efficiency. They have covalently attached the enzymes on CNTs and then implanted them into a living snail and clam. In the following years, different materials, including gold nano-particles,[21]

flexible carbon fibre,[27], and multi-walled carbon nanotubes (MWCNTs)[28] have been tested as an electrode to enhance the power density. Table 1 summarises previously prepared implantable EFCs.

The typical human body produces around 100 W of electricity, and its steady presence and fuel availability offer sufficient support for EFC operation.[29] To be used as implantable or mountable EFCs in the human body, special attention should be made to overcoming issues with power output, biocompatibility, and stability of the EFCs.[29,30] Since the first full surgical implantation of an EFC in a rat in 2010, several studies on implantable EFCs have been published.[24] Chitosan-modified biocathodes in rats lasted 167 days. Rats with implanted EFCs could power a digital thermometer or LED. The pacemaker and electronic watch in cyborg lobsters can be powered by EFC.[31]

Table 1 A comparison table highlighting the shape, current collector material, enzyme type, and power density of implanted enzymatic biofuel cells developed by different researchers.

Animal/location	Shape	Length	Current collector material	The catalyst used in the biocathode	The catalyst used in the bioanode	Power density	Ref.
Rat/retroperitoneal space	Disc	-	graphite	polyphenol oxidase (PPO)	GOx	24.4 µW mL^{-1}	[24] 2010
Snail/between the body wall and internal organs	Plate	2.5 mm^2	MWCNT	Laccase	PQQ-GDH	7.45 µW 30 µW cm^{-2}	[25] 2012
Clam/dorso-posterior part	Plate	2.5 mm^2	MWCNT	Laccase	PQQ-GDH	37 µW 40 µW/cm^{-2}	[26] 2012
Rat/retroperitoneal space	wire	1.5 mm	gold nanoparticles on gold wires	Laccase	GOx	2 µW cm^{-2}	[21] 2013

Rat/jugular vein	wire	10 mm	Flexible carbon fibre (FCF)	Platinum	GOx	95 µW cm^{-2}	[27] 2013
Rat brain	plate	6mm × 5mm	MWCNT	laccase	GOx	193.5 µW cm^{-2}	[28] 2013
insect haemolymph	plate	11 mm^2	PWDF and carbon cloth	bilirubin oxidase	glucose dehydrogenase (GDH)	285 µW cm^{-2} 333 µW	[32] 2016
Rabbit/brain	Plate	50 mm^2	MWCNT	laccase	catalase	16 µW mL^{-1}	[33] 2018

Although EFC efficiency and stability have improved, most are manufactured on a macroscale, restricting their practical use to powering implanted microelectronics.[21] Additionally, the larger size of the EFCs causes a inflammatory response in the body.[34] Therefore, the miniaturisation of EFCs is vital to achieving long-term reliable energy sources. The reduction of the size of EFCs can be achieved by further improvement in the efficiency of the cells.[17,35]

When implanted long term, the body may respond with an inflammatory response in the surrounding soft tissue, which could potentially lead to chronic inflammation. It is possible, however, for the implant to become encapsulated in fibrous tissue composed primarily of collagen, which can reduce some inflammation. Thus, during implant manufacturing, care must also be taken to prevent the coagulation response from being triggered in the bloodstream. In order for enzymatic biofuel cells to be developed further for potential medical applications, understanding the body's reaction is crucial. By understanding the body's response to implanted cells, researchers can ensure that the cells are manufactured in a way that does not trigger

the coagulation response. This could include using biocompatible materials, and controlling the size of the cells.[33,35]

2.3. Miniaturisation of EFCs

The invention of micro biofuel cells might offer implanted devices with long-term power sources when battery replacement is problematic. In the past three decades, interest in small-scale power systems employing biocatalysts has grown owing to the requirement for micro-scale power for implanted medical devices. EFC research is projected to provide a miniature power source for portable, implantable, and wearable devices (Fig. 2).
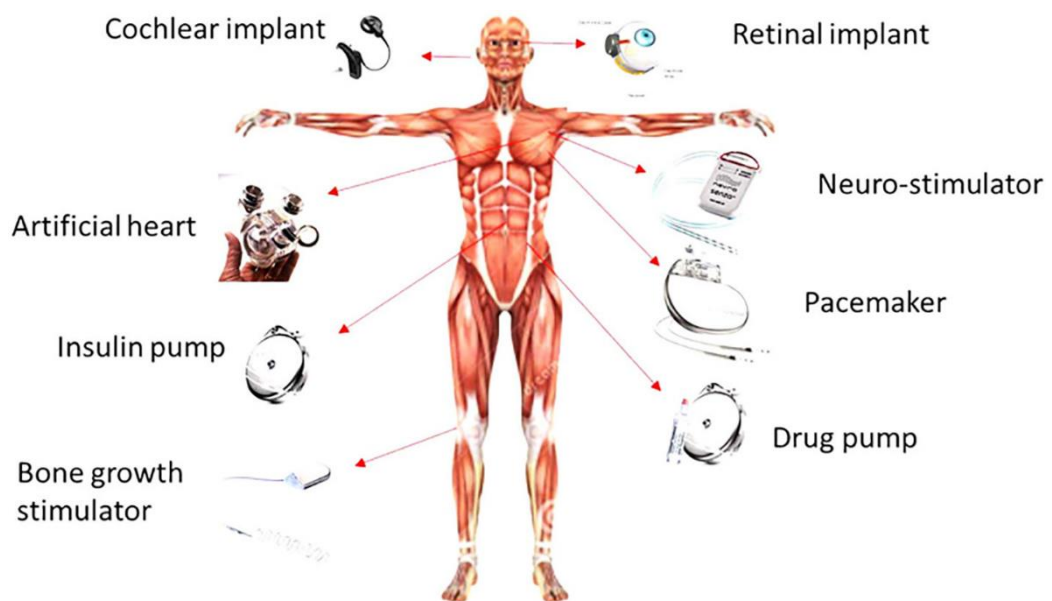
Fig. 2 Potential applications of EFCs. The use of enzyme biofuel cells as a reliable power source can power implantable electrical devices, such as pacemakers, cochlear implants, bladder stimulators, insulin pumps, wireless pressure sensors and neurostimulators, for example..[29]

Fewer active electrode materials are available with smaller EFCs, reducing energy and power generation. Miniaturising EFCs requires investigating the bioelectrodes' efficacy. EFCs with many enzymes on the electrode surface, optimal mass transport, and efficient electron transfer rates may reach maximum power density. This may be done by creating highly conductive 3D structures with a large surface area so more enzymes can be attached and selecting the optimum enzyme immobilisation technology to promote electron transport between the electrode and the attached enzyme.

2.4. Electrode with a high surface area of EFCs

The electrode's shape plays a critical role in the efficiency of the EFCs as it directly affects the amount of enzyme loading and active surface area. In this way, Viktor et al.[21] were the first group to significantly improve the geometric surface area of their implantable EFCs 100 times over unmodified electrodes by attaching the gold nanoparticles (GNPs) to the gold micro-electrode. By adding graphene plates to the electrodes instead of using bare electrodes for EFCs, Song et al. and Liu et al.[22,36] have shown that the efficiency of EFCs can be increased by seven and two times, respectively (Fig. 3). Kai et al.[37,38] used polymer moulding to create the microneedle electrode's high surface area. Results indicate improved biosensor sensitivity. Similarly, Siu and Chiao used photolithography and polymer moulding to create micropillar electrodes out of polydimethylsiloxane (PDMS). The average current density and power density increased by 4.9 and 40.5 times, respectively.[39] Chiao used

wet etching to create a silicon-based fluid channel for the EFC, which created a surface area that was more than four times larger than a simple electrode.[40]
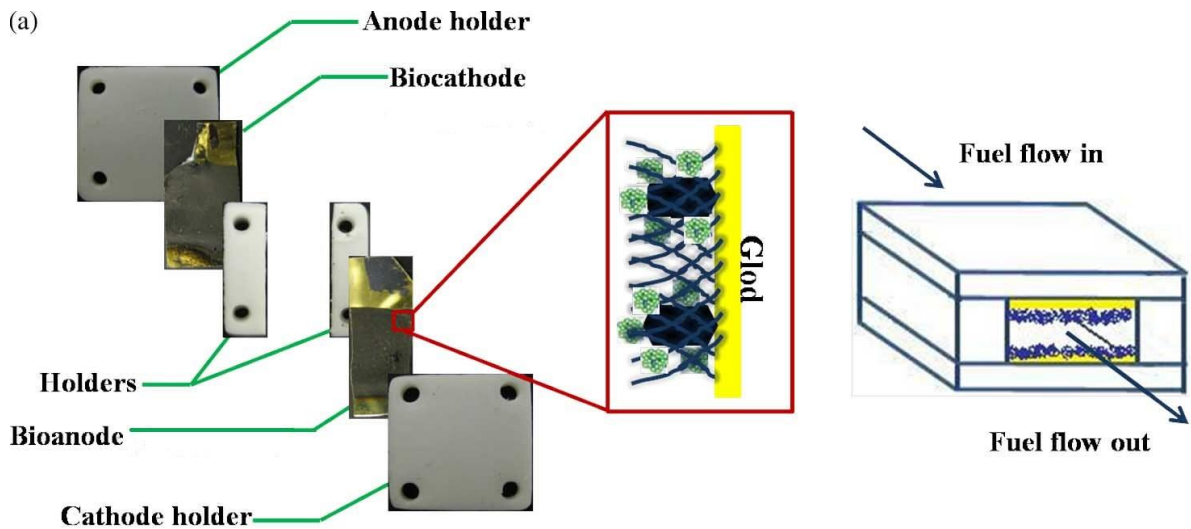
Fig. 3 Representative schematic of EFCs.[36] A schematic representation of Enzymatic Fuel Cells (EFCs) illustrating the flow of fuel through two enzyme-immobilized electrodes to generate electricity. The fuel, represented by arrows, undergoes oxidation at the anode where the enzyme is immobilized, releasing electrons.

Although EFC power density has increased by increasing the electrode's surface area, little effort has been made to optimise EFC shape to provide adequate power.[29] Additive manufacturing can address this problem by providing design freedom to fabricate electrodes in various geometries. It can create conductive metal-based bio-electrodes in 3D cellular (lattice) patterns, which substantially increases surface area, the mass transfer interface between the two sub volumes, and mechanical load support.[41]

Lattice structures offer many exceptional qualities that make them a promising option for a variety of applications, such as a lightweight construction owing to its high

specific stiffness and strength, an energy absorber due to its capacity to tolerate considerable deformation at a relatively low-stress level, and facilitating the mass (such as nutrition, oxygen, and waste) transporting within the pores.[29,42] Lattice structures have been created using several standard manufacturing processes, such as investment casting, deformation forming, and metal wire methods.[43] To produce the necessary structures, these procedures, however, demand complex machinery with exact process control and additional assembly or bonding phases. Additionally, while utilising these processes, the range of feasible designs is severely constrained. On the other hand, the specific advantages of additive manufacturing (AM) technology make it well suited to produce parts with lattice structures.

2.5.   Additive manufacturing of electrodes

Currently, subtractive methods are the technologies most often used in industry to create 3D conductive micro/nanostructures. These methods also need labour-intensive sample preparation and have a high risk of harming the samples' surfaces.[44] AM of microelectrodes is becoming more popular since it allows design flexibility and manufactures complicated conductive devices fast and affordably. The AM of electronics has been intensively researched in both industrial and research domains, and the worldwide market could reach 26.6 billion dollars by 2022, up from 14.0 billion dollars in 2017.[45]

The term "3D printed electronics" refers to a technique that either enables the incorporation of electronics into items or the direct creation of electrically conductive traces on the surfaces of the objects.[46] The AM of 3D electronics has been extensively

investigated due to their demand for application in the production of 3D integrated circuits,[47] microelectronics,[48] microelectrochemical systems,[49] sensors,[50] batteries,[51] conductive tracks,[52] and solar cells.[53] Further classifications of 3D printed electronics include 3D fully printed electronics are electronic components made using additive manufacturing techniques, in which electrically conductive elements and dielectric materials are sequentially deposited to create intricate multilayer structures (Fig. 4).[54,55] This method can enable the manufacturing of various electrical device designs without the extra use of moulds and masks, which can ease production on demand.[46]
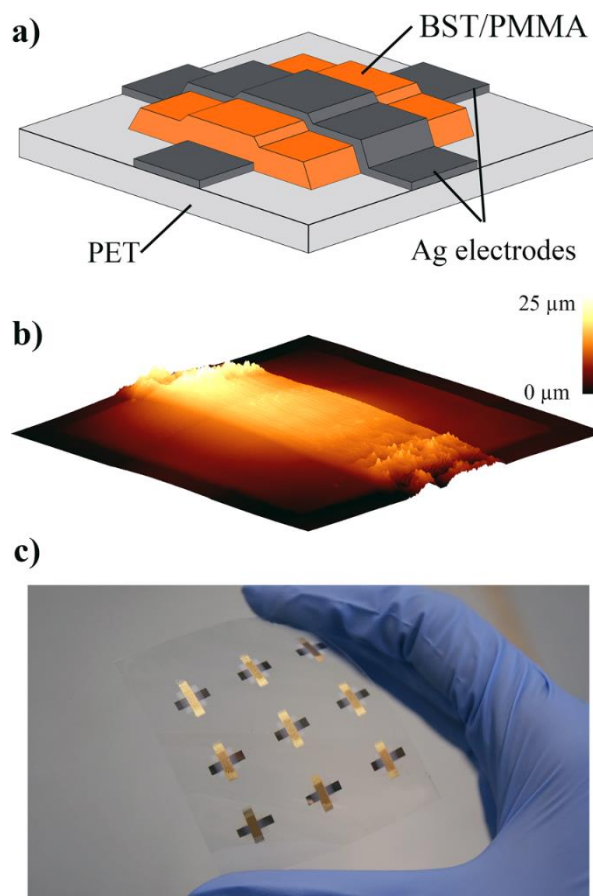
Fig. 4 (a) Schematic layout for the printed capacitors; (b) Topography of a fully printed capacitor with ink A1; (c) Picture of a PET substrate with nine printed samples.[55]

According to the ASTM, AM process can be divided into seven groups, as indicated in Fig. 5. These groups are: binder jetting, directed energy deposition, material extrusion, material jetting, powder bed fusion, sheet lamination, and vat photopolymerisation.[56] Due to the high demands for the printing of electronics, all these techniques have been extensively explored, which will be summarised in the following:
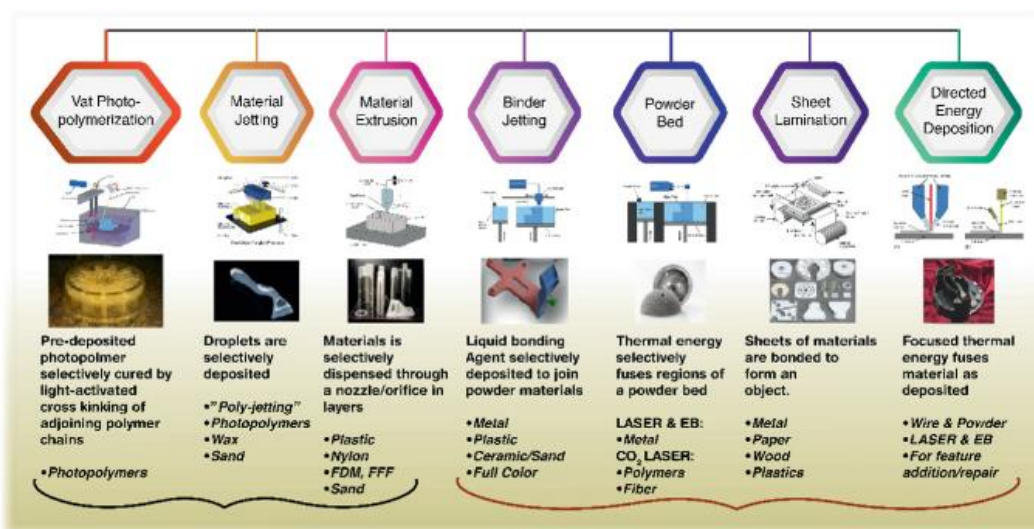
Fig. 5 Seven Additive Manufacturing techniques including fused deposition modelling, stereolithography, selective laser sintering, electron beam melting, digital light processing, and binder jetting.[57] These techniques each use a different method for building a 3D object layer by layer, such as melting, sintering, or jetting.

2.5.1. Material extrusion/Direct ink writing (DIW)

3D direct ink writing (DIW) is the most popular AM technique due to its broad range of materials, simple procedure, and low-cost process. In this filamentary printing approach, concentrated ink is extruded through a tapered cylindrical nozzle manipulated with micro- to nanoscale resolution using a three-axis, motion-controlled

stage (Fig. 6).[58,59] Printable ink for DIW is mostly high-viscosity thermoplastics such

cellulosic materials, poly(ethylene glycol)s, siloxanes, and photocurable polymers.

Ceramic particles, fibres, or other additives are added to printable slurries to provide

printed objects certain physical and chemical properties. Good printable ink has

rheological qualities that keep it from smearing.[60]
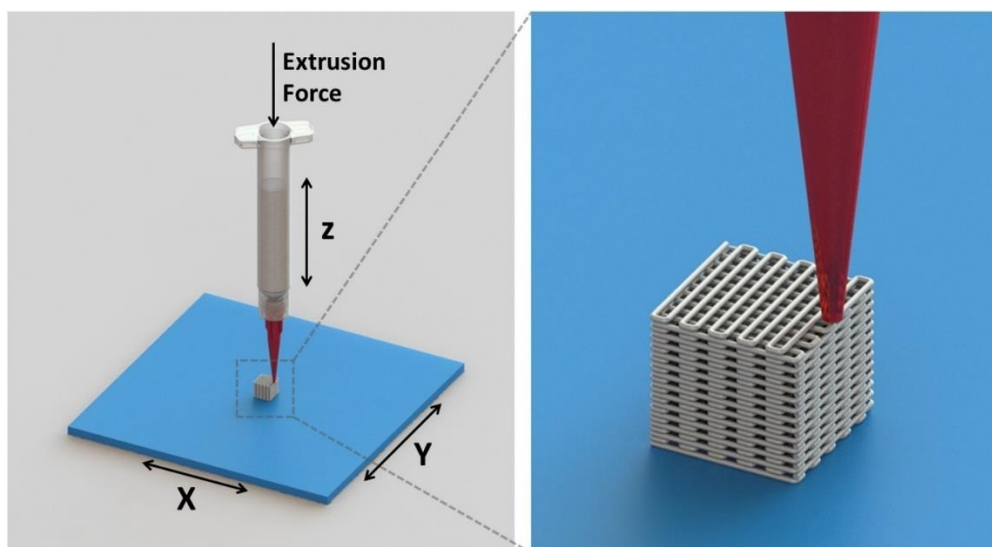
Fig. 6 Direct Ink Writing (DIW) technology schematic illustration.[59] The DIW system consists of a syringe containing the ink material, a nozzle or extrusion tip for precise deposition, and a computer-controlled stage for controlled movement. The ink material is extruded through the nozzle in a controlled manner to create three-dimensional structures layer by layer, enabling the fabrication of complex and customised objects.

In printing electrodes using DIW, a different conductive was added as a filler to

the printable ink slurry to make the printed part conductive (Table 2). Various

interdigitated electrodes with a high aspect ratio were printed in 3D using this

technology, resulting in the optimal area and volumetric capacity.[61,62] Using carbon

nanomaterials as the filler has been extensively investigated to fabricate electrodes,

providing high conductivity, stability, and biocompatibility.[63] Chandrasekaran et al.[64] construct macroscopic designs by manufacturing a printable aerogel graphene-based ink. This approach allowed for precise control of pore shape while preserving graphene's inherent benefits. The combination of graphene oxide and graphene nanoplatelets, according to Moyano et al.[65], considerably increases ink printability, mechanical properties, and conductivity of the 3d product. However, the main problem with carbon fillers is low conductivity. The higher conductivity can be achieved by adding more amount of fillers. However, this can cause low mechanical properties of the final part.[66,67]

Chao Xu et al.[68] utilised the DIW technology to effectively produce steel structures by multi-material printing of copper (which has a lower melting temperature than steel) and alumina (high thermal and chemical stability than steel). Copper permeated entirely into the pores of steel structures during sintering, resulting in a hybrid construction with a brittle 3D structure. On the other hand, Alumina was printed to serve as a removable support framework. The high conductivity is obtained due to the high-temperature sintering, which removes the polymer from the matrix and links the metals together. However, this approach's actual implementation in printing microelectrodes may be impeded by poor resolution (~250 µm). In addition, the unproportional shrinking of the printed part after sintering may lead to the deformation of the final structure.[68]

Table 2 A comparative table showcasing the conductivity of parts printed using Direct Ink Writing (DIW) technology with different filler materials in the ink preparation. .

Fillers	Conductivity (S m^{-1})	Ref.
Carbon aerogels	995	64
Graphene and graphene oxide	4205	65
TiO$_2$	66400	69
Steel	740000	68

2.5.2. Selective laser melting (SLM)

SLM is a laser-based powder bed fusion AM method. In this approach, a substrate plate is coated with metal powder in a building chamber. After powder application, a high-energy-density laser melts and fuses select locations based on processed data. After laser scanning, the platform is lowered, the second powder layer is deposited, and a new layer is scanned (Fig. 7). The process is then continued for further powder stages until all necessary components are produced.[70] Controlling processing parameters customises grain size, texture, and microstructural component morphology, altering printed components' electrical conductivity.
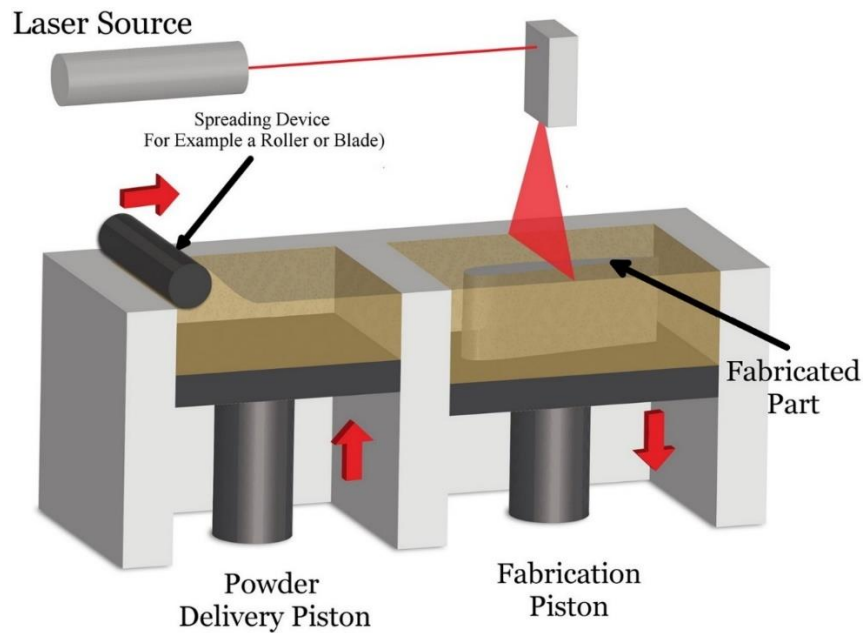
Fig. 7 Schematic presentation of Powder bed fusion.[71] The figure illustrates the key steps involved in PBF, starting with a powder bed of the chosen material. A laser or electron beam selectively melts the powder particles, fusing them together to form a solid layer. The build platform then descends, and a new layer of powder is spread, repeating the process until the entire object is fabricated. The figure demonstrates the layer-by-layer construction of three-dimensional objects through the precise melting and solidification of powder material in PBF technology.

Using SLM printing technology, Ventura et al.[72] have created a copper alloy with a density of 98%, a yield strength of up to around 590 MPa, and the conductivity of copper in its bulk form. It has been shown that 8 hours of ageing heat treatments (at 450 °C) on as-printed samples will result in a conductivity of 34.2 % of the copper in the bulk form. Even though a lengthier heat treatment could result in more conductivity, the mechanical characteristics were drastically reduced. Another study addressed this issue by looking at the laser strength, scan speed, and hatch distance to ensure optimum conductivity.[73] A narrow laser point (25 µm), fine powder (5–25 µm), and thin layer thickness (10 µm) can densify pure copper components with high

resolution and little roughness at low laser power. Pure copper components with a 99.6% relative density and 76.1% electrical conductivity are produced.[74]

SLM can provide high conductivity and mechanical properties, however printing resolution must be improved to make small conductive electrodes. Conventional SLM's lowest printed feature size is 40–200 μm, inappropriate for microelectronic devices.[75]

2.5.3. Inkjet printing

Inkjet printing is commonly utilised to make electrodes due to its high resolution and conductivity. Inkjet 3D printing uses a small nozzle on the print head to eject aerosol. As the print head moves, layers are formed. Inkjet printing offers fine surface patterning and versatility. This simple printing technology has several uses in electronics.[76,77] However, generating monodispersed conductive nanoparticles and modifying the ink's viscosity and surface tension to get the acceptable dripping behaviour is necessary for inkjet printing conductive materials.[44] Droplet sizes must be kept to a minimum in order to prevent nozzle clogging. Additionally, for the material to fulfil the requirements for jetting, its viscosity must be low, not be higher than 10-16 mPa·s.[78] Inkjet printing of microelectrodes generally involves 2D printing of conductive materials. Adding UV curable ink to the ink formulation can print 3D components, although they have limited conductivity. Low conductivity is caused by unconnected nanomaterial lines in the polymer matrix.[79]

2.6.   Vat photopolymerisation

Vat-photopolymerization is a kind of 3D printing that builds three-dimensional shapes layer by layer using a vat of liquid resin and a light source. In this method, the resin is exposed to light to solidify it, and the product is built by selectively curing each layer of resin until the thing is finished. This method is often used to precisely manufacture small, complicated pieces. One issue with 3D-printed components is that, depending on the application, they can not have the appropriate electrical conductivity. Nevertheless, electroless plating may be used to provide a conductive coating to the surface of a 3D-printed component. Without the use of an external electrical source, electroless plating is applying a metal layer to a substrate. As an alternative, a reducing agent is employed to reduce metal ions in a solution, which subsequently deposits on the part's surface. Electroless plating may be used to cover a 3D-printed item with a conductive layer, allowing for the precise and controlled creation of microelectrodes. This method is promising since it eliminates the need for costly or involved manufacturing methods and enables the production of highly accurate and customised microelectrodes. Combining 3D printing with electroless plating also makes it feasible to create intricate patterns and geometries that would otherwise be impossible to make using conventional production methods.

In the vat photopolymerisation (VP) process, photosensitive materials are carefully exposed to light to create layers of polymerised material. A 3D object is created by combining subsequent layers. Vat-photopolymerisation, regarded as the most accurate 3D printing method, has a wide manufacturing window ranging from a

few nanometres to several centimetres.[10] The primary components of photopolymer resin, which hardens due to crosslinking, are monomers and oligomers (Fig. 8). In response to curing light, photoinitiators change into radicals, interact with oligomers and monomers, and induce crosslinking that results in polymer chains.[80]
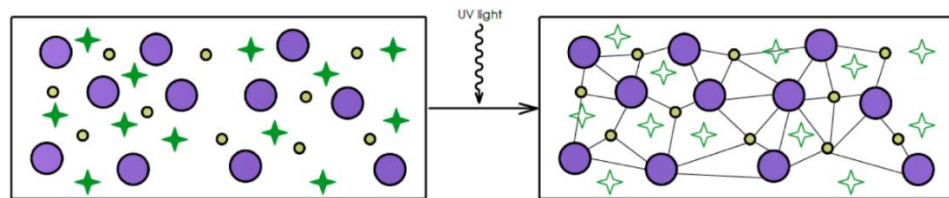
Fig. 8 A schematic representation illustrating the components of a photocurable ink. The ink consists of a photoinitiator, a photo-absorber, monomers, and/or oligomers. The photoinitiator initiates the curing process upon exposure to light, while the photo-absorber enhances light absorption for efficient curing. Monomers are the building network that polymerise and crosslink under light exposure [11]

VP methods can be classified into stereolithography (SLA), digital light processing (DLP), and two-photon polymerisation (2PP). SLA and DLP both use UV-induced polymerisation of resin. DLP employs micro-mirrors to create instant full-layer polymerisation. SLA exposes one laser point (a stacked pixel) at a time. Compared to SLA and other technologies, DLP has higher printing rates. Fig. 9 displays the SLA and DLP technologies' operating theories.
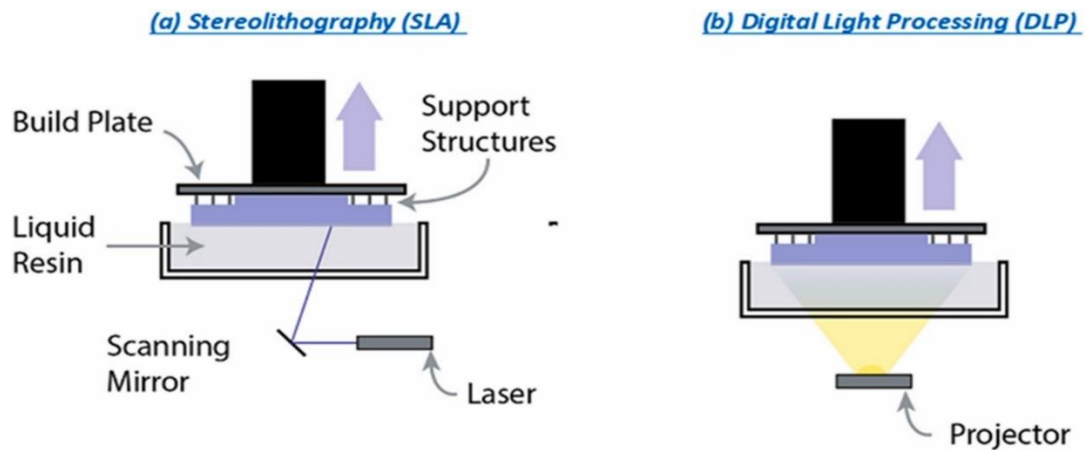
Fig. 9 A comparison of the schematics of Digital Light Processing (DLP) and Stereolithography (SLA) printers. In DLP printing, a digital micromirror device (DMD) projects light onto the entire layer simultaneously, while SLA printing employs a laser or UV light that selectively scans the surface to cure the resin.

2PP is a vat photopolymerisation-based printing method that offers superior control and print quality. The 2PP can build 100-nm-scale 3D structures. In 2PP, two photons are absorbed simultaneously by a photoinitiator, causing reactive species to form, which initiate polymerisation. Polymerisation only occurs at the laser beam focal point, which is closely controlled using high numerical aperture (NA) objective lenses. Generally, the higher the NA of an objective lens, the smaller will be its spot size due to its ability to gather light. 2PP can achieve extremely high resolution with as small as ten nanometre feature sizes using a high-NA objective lens and a short-wavelength laser. Furthermore, a femtosecond laser allows precise control of laser pulse duration and energy. These enables the fabrication of complex structures with high precision and accuracy.[81,82] After the selective photopolymerisation, the structure is exposed by washing off non-polymerised photoresist (Fig. 10).[83] This method is suitable for printing 3D structures with a high surface area. However, directly fabricating the

electrically conductive structure with this 2PP is challenging. This technique's direct printing of highly conductive structures is possible if the photoresist contains sufficient conductive materials.[45] However, a higher concentration of conductive nanomaterials, usually leads to poor mechanical properties in 3D-printed microstructures..[67] Furthermore, the metals/metal ions in the photoresist can scatter and hinder the laser light, causing unwanted polymerisation and metal nanoparticle growth during laser irradiation.[84,85] Therefore, a more careful and tedious photoresist optimisation process is required to improve conductivity and printability. The highest conductivity achieved with this technique is still 3-20 times lower than the conventionally applied bulk metals in electronics.[44] This low conductivity mainly arises from disconnected conductive nanomaterials entrapped within the polymer matrix.[79]
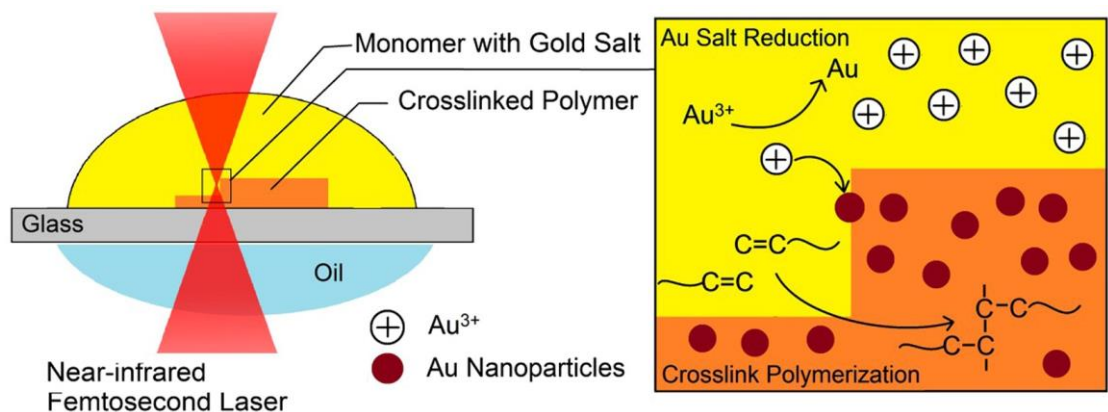
Fig. 10 An example of a typical procedure for creating nanocomposites using two-photon polymerisation and photoreduction in unison.[83] The figure illustrates the key steps, beginning with the focusing of ultrafast laser pulses onto a localized region within the resin. The high-intensity laser induces a nonlinear absorption process, allowing for precise control over the polymerization. As the resin solidifies, the build platform moves, layer by layer, creating intricate and high-resolution 3D printed structures.

This study has selected the VP method because it is the most precise method for building 3D structures. Its goal is to overcome the issues mentioned above in order to get the maximum conductivity. This study will go into depth on polymer template coating, which is one solution to this issue. By carefully functionalising the printable ink, it is possible to print a part with a functional group on the surface, creating a suitable surface for metal attachment. Extensive research is needed to develop the ink for this procedure.

2.6.1. Ink for VAT-photopolymerisation

Vat-photopolymerisation depends on light irradiation via a reservoir (vat) stocked with photocurable materials to photopolymerise liquid monomers and oligomers at a specified point on the building platform (Fig. 8). This precision printing process has significant promise for bio-electronics applications. Chemical formulas of printable resin are generally confidential and not released by makers, leaving physicochemical and mechanical properties (such as tensile strength and elongation at break) and hazard identifications (cytotoxicity) unknown. Not all commercially available photopolymerisable monomers/oligomers are acceptable for certain needs; hence, 3D-printed components cannot be made using currently available resins.[86] Therefore, there is a growing demand for novel photocurable medicinal materials. Biocompatible materials should be used in photoresist biomedical applications, such as implanted EFCs, to prevent negative consequences. The printed component should also be strong enough to avoid part breakage and metal flaking. Three components make up photocurable ink: a photoinitiator, a photoabsorber, and a monomer or

oligomer. A photoinitiator triggers monomer polymerisation by absorbing UV light and generating free radicals. The photoabsorber prevents overpolymerisation and enhances printing control.[87]

2.6.2. Monomer/oligomer
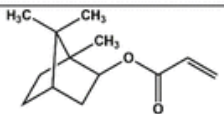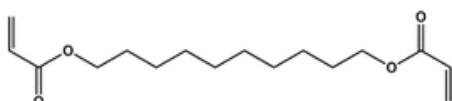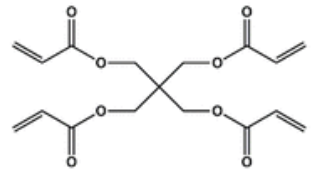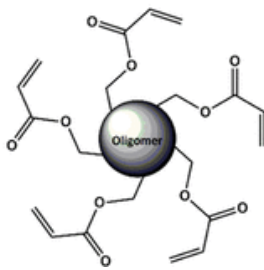
The high potential of the VP biomedical applications has led to the development of a wide variety of improved resins. Each category uses a different polymerisation method: radical polymerisation for acrylic or methacrylic resins and cationic polymerisation for epoxy or vinyl ether resins. Acrylic and methacrylic acids are popular resins as they provide rapid response times, long-term stability, and tuneable mechanical properties. Due to their cytocompatibility and ease of sterility, acrylate-based monomers are ideal for biological applications.[86–89]

The number of functionalities can affect the polymerisation by altering the reactivity of the acrylate molecules. When more functionalities are present, the molecules react more quickly, and the polymerisation will be more efficient. On the other hand, mono-functionalised acrylates have lower molecular weight, which reduces the viscosity of the resin and results in a more flexible product.[90] A larger number of double bonds ($[C=C]_0$) in the system causes the creation of a higher cross-linked polymer network, and higher cross-link densities cause the material's stiffness to rise. In this way, Voet et al.[91] showed that the cured biobased acrylate photopolymer resin (BAPR) products' Young's modulus does rise as the double-bond concentration rises (Table 3). More acrylate content in the monomer also results in higher viscosities. While larger molecular weight monomers are more flexible and less

3 D - p r i n t i n g   o f   e n z y m a t i c
b i o f u e l   c e l l s
55 | P a g e

reactive, lower molecular weight monomers have more reactivity and stiffness.[90]

Therefore, careful monomer selection is required to achieve desired viscosity and

stiffness.

Table 3 Relationship between the double bond concentration and printed part stiffness.[91] The more acrylate groups that are present, the stronger the polymer network will be and the faster the photopolymerisation reaction will occur.

Acrylate	Structural formula	BC %	f	ρ kg·dm^{-3}	M kg·mol^{-1}	$[C=C]_0^a$ mol·dm^{-3}	η Pa·s
SA5102		75	1	0.99	0.21	4.8	0.01
SA5201		60	2	0.98	0.28	7.0	0.01
SA5400		10	4	1.17	0.35	13	0.35
SA7101		70	5	1.04	1.7	2.7	17

Acrylic-based resins may be readily modified to provide the desired physical and

chemical qualities. Yee et al.[92] developed functional monomers utilising the Michael-

thiol process. PETTA, a tetrafunctional acrylate, was used to manufacture the

functionalised acrylate in a 1:1 mol ratio reaction with a thiol to ensure that the final

monomer combination contained an average of three acrylates per monomer

molecule, which is acceptable crosslinking. Since the functional groups are directly

placed onto the monomer, they should be uniformly attached to the structure. Thus,

this is also a versatile method for binding various functional groups to surfaces. Using

this approach, they could print polymers with functional groups. This functional group

may also post-functionalise. This approach is being explored for a PhD project, which

will be addressed in depth in the next chapters.

2.6.3. Photoinitiator
The photochemical process typically starts using photoinitiators with high molar

extinction coefficients at short wavelengths. The photoinitiators must be exposed to

light with the right wavelength and enough intensity to respond as intended. In the

absence of this, the chemical reaction may not occur, or it may not occur fully, leading

to subpar or uneven polymerisation performance. When exposed to UV light, the

photoinitiator decomposes, creating radical or cation-active species that would start

the reaction system's active monomers or oligomers.[93] As a result, the polymeric

mixture may be immediately transformed from a liquid to a solid by being exposed to

an appropriate UV light source. The initiating species can consist of radicals, cations,

or anions. The three most important characteristics of a photoinitiator are (i) high

absorption at the exposure wavelength and a high molar extinction coefficient, (ii) a

high quantum yield of initiating species, and (iii) a high radical reactivity towards the

monomer.[94] There are two types of type I and II initiators for free radical UV photoinitiators.[95]

Nourish type I: Usually, benzoyl-containing compounds are used as nourish type I initiators (Fig. 11). When the initiator's carbonyl absorbs a photon, it becomes excited. Excited carbon bond homolysis creates two radical fragments. 2,2-Dimethoxy-1,2-diphenyl-ethan-1-one cleaves into methoxybenzyl and benzoyl. Methoxybenzyl breaks down into methyl and methyl benzoate, whereas benzoyl initiates free radical polymerisation.
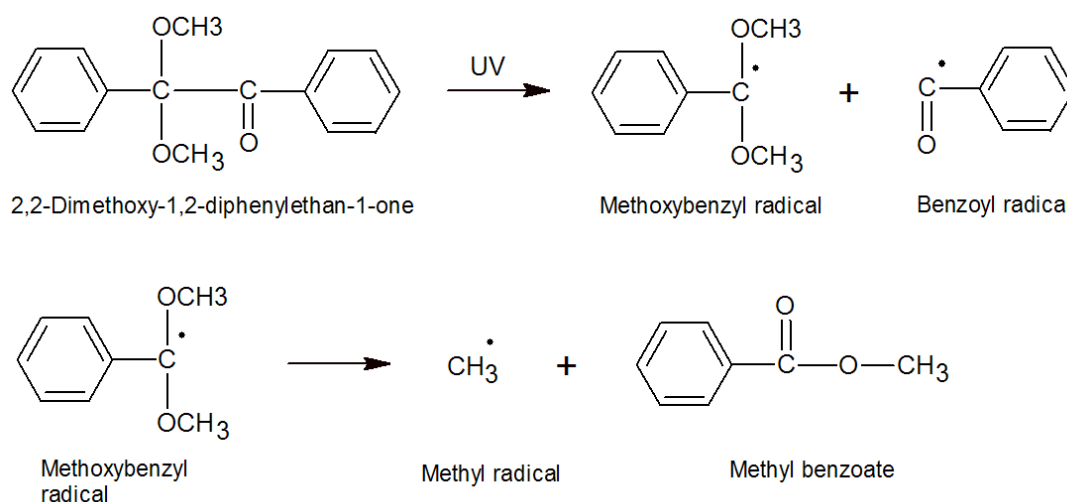
Fig. 11 Photoinitiation process in type I photoinitiators.

Nourish type II: Type II initiators absorb UV light to produce excited molecules, which steal an electron or a hydrogen atom from a donor molecule (Fig. 12). Then, a

monomer and the donor molecule interact to start the polymerisation process. Benzophenone and its derivative, isopropyl thioxanthone, and tertiary amines as donor molecules are typical type II photoinitiator complexes. The excited photoinitiators use the amines as active hydrogen donors. Hydrogen abstraction results in highly reactive alkyl-amino radicals, which then kickstart polymerisation.
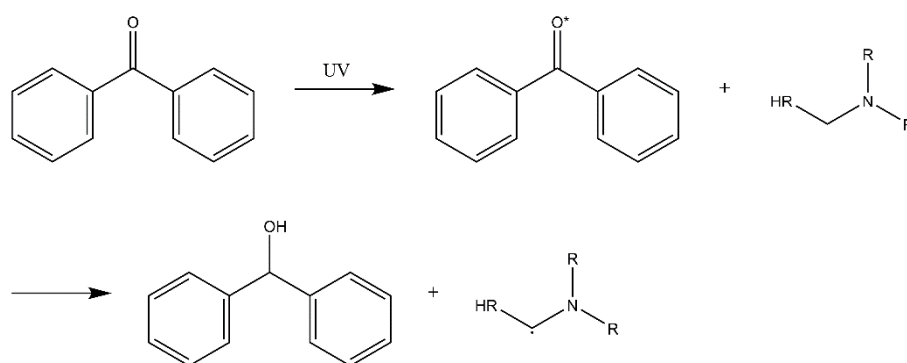
Fig. 12 Photoinitiation process in type II photoinitiators.

Type I photoinitiators do not need an amine group, unlike type II photoinitiators. Additionally, Type I photoinitiators undergo quick photolysis, producing highly reactive radicals like benzoyl and phosphoryl, which start the polymerisation process.[96] Due to their importance, numerous efforts have been made to develop appropriate photoinitiators. Kiefer et al.[97] list many photoinitiators and classify them according to the figure of merit (FOM), which relates to the photoresist sensitivity. Among these photoinitiators, Irgacure 819 (or BAPO),[98] CQ,[99] TPO,[100] and ITX[101] are commercially available with good FOM for biomedical applications. However, some of them are not appropriate for printing scaffolds for implantable applications, including

the enzymatic biofuel cells, due to their poor biocompatibility. For instance, ITX is not a promising option for tissue engineering applications due to its poor biocompatibility.[102–105] Irgacure 819 (Irg 819) is a type 1 photoinitiator with two carbonyl groups in its structure (Fig. 13).[106] Compared to TPO, IRG 819 is a more effective photoinitiator, as it generates four reactive radicals from a single molecule. Furthermore, Irg 819 exhibits a significantly higher molar extinction coefficient of 870 L/mol cm. This is substantially greater than that of CQ (33 L/mol cm).[107] Recent research conducted by Lima et al. highlighting that Irg 819 also appears to be the most promising photoinitiator for biological applications due to its excellent performance and biocompatibility.[98,108,109] This is the reason it has a variety of biomedical applications. For instance, various research using tissue engineering of bone scaffolds have employed the 3wt% of the Irg 819.[110–112] Another example is the use of 1wt% of Irg for cell culture by Warr et al.[113] One of the biggest advantages of Irg 819 is better solubility in most monomers and solvents.[95]
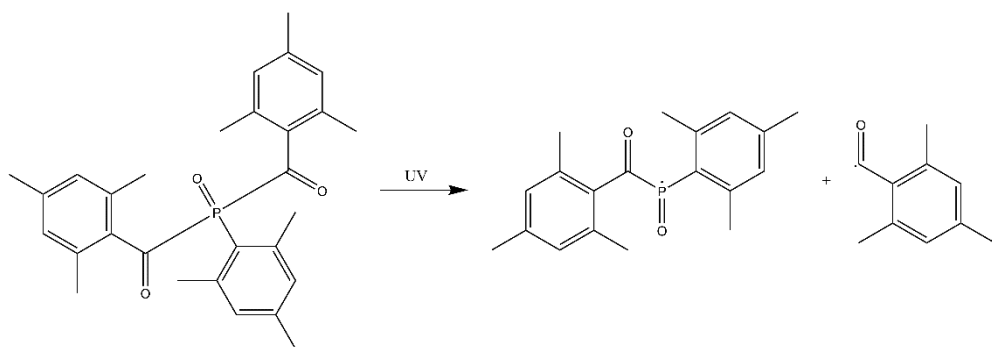
Fig. 13 Type I photoinitiation process of Irg819. Active radical molecule forms when the photoinitiator exposing to UV light.

2.6.4. Photo-absorber

In stereolithography, the light path determines the XY resolution, but light-attenuating additives that absorb extra light and constrain polymerisation to the appropriate layer thickness determine the z resolution, which improves pattern accuracy. These photoabsorber additives help to ensure that light is absorbed uniformly throughout the resin, which can increase the resolution of the 3D printed object. Without them, it is difficult to achieve the same level of detail in the finished product. However, the lack of adequate photoabsorber additives is another challenge, making it more complex or costly to improve Z resolution in the 3D photopolymerisation..[114] Because of their known genotoxic and carcinogenic properties, conventional light-blocking compounds used for photoresist patterning or creating plastic parts, such as Sudan I, are not appropriate for biomanufacturing.[115] Recently, Grigoryan et al.[114] recommended using commercial food colours, both synthetic and natural, as effective but non-toxic light absorbers for projection stereolithography. They have shown that aqueous pre-hydrogel solutions containing the ingredients tartrazine (FD&C Yellow 5, E102, a yellow food colouring), curcumin (from turmeric), or anthocyanin (from blueberries) can all produce hydrogels with a patent vessel. The discovery of these non-toxic photo absorbers for projection stereolithography can pave the way for creating popular biocompatible 3D constructions.

2.7.   Metal coating of 3D-printed polymer

Polymeric materials' flexible and stretchy to stiff and rigid mechanical qualities are employed in aerospace, automobile, and healthcare. Complex and integrated

polymeric product design requires scalable, sustainable, and resource-efficient methodologies. 3D printing allows design flexibility, flexible prototyping, and assured component quality for polymeric materials. 3D-printed polymers are employed in actuators, sensors, antennas, and medical devices. However, 3D printed polymers lack electrical conductivity, limiting their use as conductors.[116]

As mentioned in prior section, it is possible to directly print conductive 3D structures by adding conductive nanomaterials to the printing material, resulting in low conductivity. These techniques can achieve higher conductivity if adding a high load of additives. However, this will dramatically impact the printability and physical properties of the printed part. Coating the part after printing is a possible solution for this problem as it provides flexibility in manufacturing different conductive materials without affecting the printability and physical properties of the part. One critical issue with the coating is the adhesion of the deposited metal on the printed part. Therefore, surface treatment should be performed before the coating process. Without the surface treatment, the deposited metal can peel off after the coating.

2.7.1. Surface treatment of 3D-printed polymer

Different surface treatments have been used to enhance surface tension, which boosts bond strength and durability of polymer composite adhesive joints. This includes improving surface roughness and chemistry. Using physical and chemical methods, metal adsorption on substrates has been enhanced. These procedures may be split into three categories: acid etching, plasma treatment, and printable resin treatment.[117–122]

Chemically etching 3D-printed polyacrylate improves plating adhesion. Chemical etching roughens and hydrophilises the polymer's surface so the metal coating can adhere during metallisation. Through optimised acid etching, metal adherence to polymers is achieved.[123,124] In a recent study, Kim et al.[121] showed that hydrochloric acid could be used to functionalise 3D-printed pentaerythritol triacrylate (PETA). Surface carboxylate groups form when acid breaks C-C bonds (Fig. 14). The carboxylate group helps connect stabilised gold nanoparticles to electroless plating polymer.
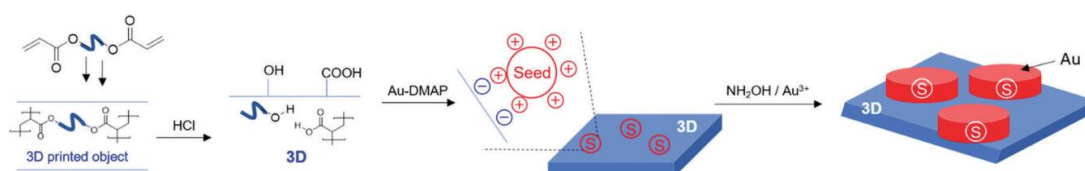
Fig. 14 process for electroless plating of the 3D-printed part using acid etching.[121] after the surface treatment, the nanoparticles seeding on the polymer surface. The particles then grow while soaking into the electroless plating solution until they join together and for a metal film.

This method generates a homogenous metal coating, but the metal's adherence to the polymer was poor, leading to peeling (Fig. 15).
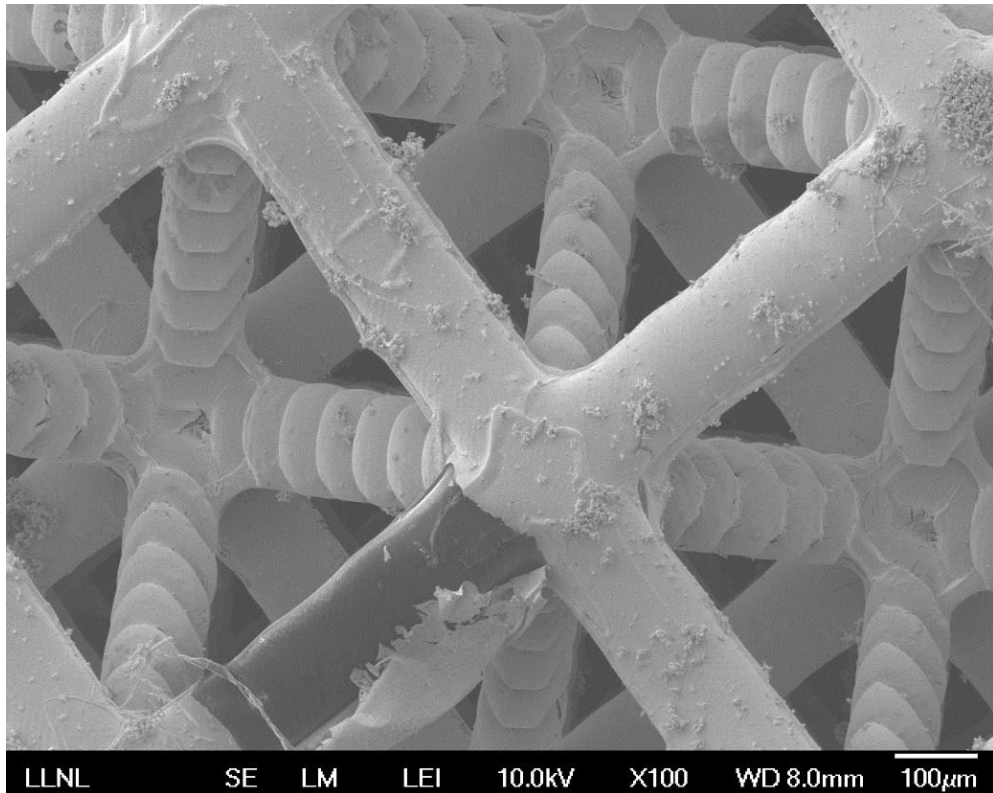
Fig. 15 SEM image of the gold coated polymer that partially peeled off. The uncoated polymer surface is dark where the gold is bright, and vice versa.[121] This image illustrates how weak adhesion between 3D-printed polymer and deposited gold leads to gold film peeling off.

PLASMA TREATMENT

Plasma is an energetic medium made up of atoms, molecules, radicals, positively and negatively charged ions, and electrons from an external source. Plasma exposure cleans, ablates, cross-links, and alters chemical properties. Plasma discharge also introduces chemical functionality based on the material and process gas. Interaction between a polymer surface and plasma may dissociate hydrogen from polymeric chains and produce free radicals. Plasma-activated radicals may interact with gas particles, adding new functional groups to polymer surfaces.[125] Vorck et al.[126]

showed how to bind a dithiol (1,2-ethanedithiol) group to a plasma-exposed polymer. The thiol attachment strongly connects the polymer and the gold nanoparticles.
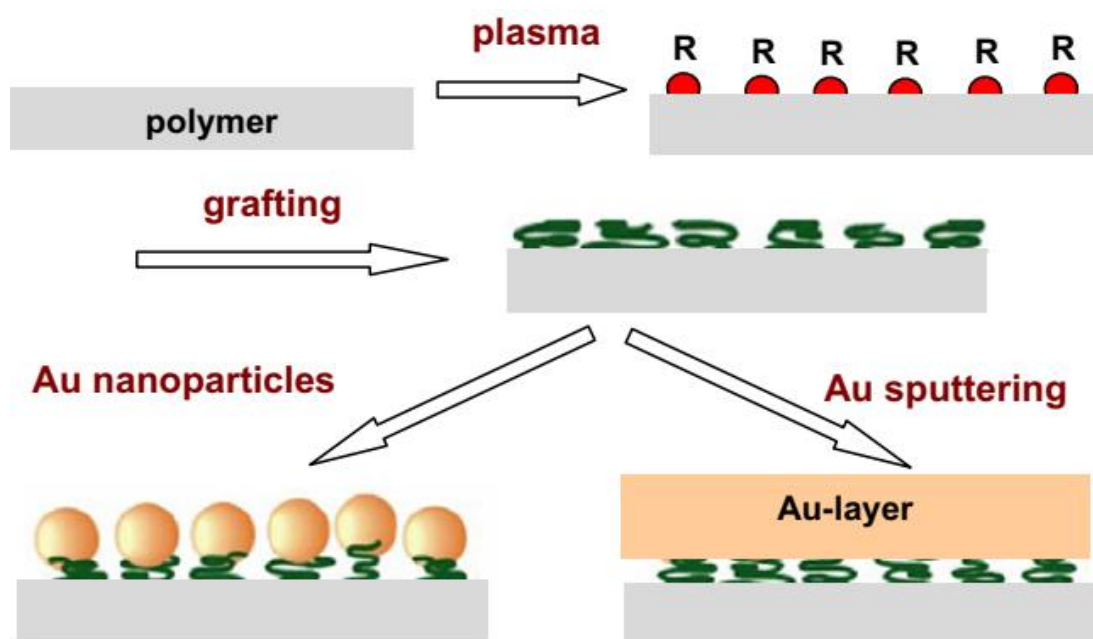
Fig. 16 Scheme of polymer modification by plasma discharge (R-radical), grafting by dithiol and by either coating with Au nano-particles or by sputtering of Au nano-layer.[126]

In this way, Yan et al.[127] successfully used plasma to treat the surface of a 3D-printed microstructure and coated it with silver. This is a simple and successful procedure for surface functionalisation, but plasma treatment of bigger, more complex 3D-printed parts is difficult owing to line-of-sight limits.[128,129] Although John et al. have shown that nitrogen plasma can penetrate into pores even as deep as 5mm, most treatment takes place on the surface of the scaffold, and the effectiveness of the treatment decreases with every millimetre of depth.[130]

This approach uses thiol-ene-based resins to print functionalised polymers in situ. Thiol-ene-modified polymers boost adhesion strength and polymer-metal compatibility, according to new study. Mandal et al.[131] modified UV-curable PTHBMA using thiol-ene chemistry. Thiol-modified PTHBMA has a greater lap shear strength than unmodified PTHBMA. Shahzadi et al.[132] recently designed and optimised thiol–acrylate resin compositions to manage polymerisation depth and obtain a surface thiol group. Free thiol groups at the surface of off-stoichiometric resin formulations were employed to immobilise gold nanoparticles (Fig. 17). In addition, thiol-ene/acrylate polymers are biocompatible and sterilisable with ethylene oxide,[133], Ideal for biomedical applications.[134] Enhanced adhesion from thiol-ene/acrylate polymer has proven success in intracortical probes that use noble metals, such as gold, to monitor brain activity.[135]
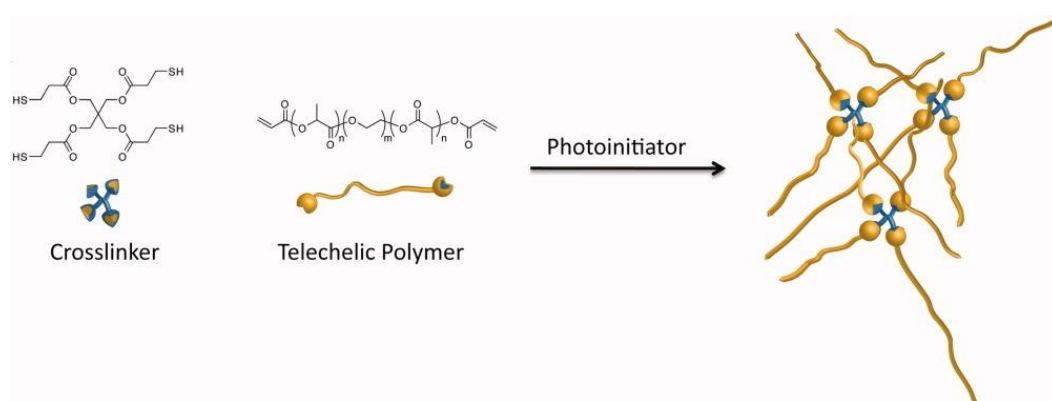
Fig. 17 Polymerisation of thiol-ene base resin.[136] The thiol-contained molecule reacts with acrylates and form a crosslink with monomers.

This surface functionalisation approach is feasible since the excess thiol group is directly displayed on the surface. However, most of the thiol groups in the resin are consumed in the interaction with the acrylate group, leaving less free thiol on the surface.[92,137] Adding an excess quantity of thiol-based cross-linker such as multiactylate molecule may improve the likelihood of thiol group on polymer surface, however thiol-ene systems have inferior mechanical qualities than acrylate-based systems because crosslink density decreases along with volume shrinkage. Since volume shrinkage depends entirely on the number of double bonds that react and is unaffected by thiol concentration, fewer double bonds are available to cause volume contraction.[138]

Another approach is that the multifunctional monomers are pre-functionalising with various groups via the thiol-Michael addition reaction prior to printing (Fig. 18). The functionalised acrylate monomers are then mixed with a photoinitiator in an appropriate solvent and used to fabricate the 3D structure.[92] This methodology relies on carefully selecting the monomers so that the necessary functional groups are not consumed during the polymerisation process. The functional groups exist on the surface since they are directly attached to the monomer. This is a versatile approach to attaching various functional groups on the surface of the polymer, as shown in Fig. 18. This technique has been looked into via this PhD study since it demonstrates a reliable methodology to add a significant quantity of thiol to the polymer's surface.
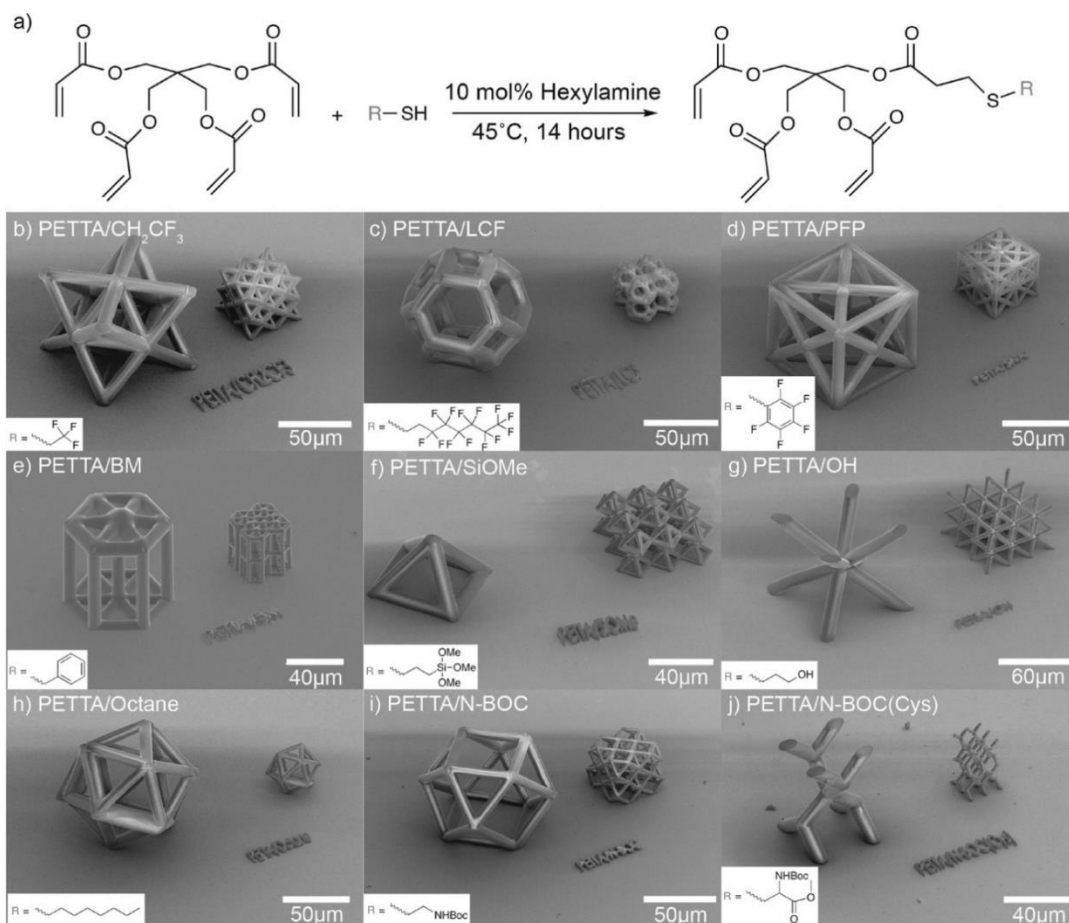
Fig. 18 a) Chemical composition of the functional monomers produced by the thiol-Michael reaction between pentaerythritol tetraacrylate and a thiol. A sample product is shown. PETTA/CH$_2$CF$_3$, PETTA/LCF, PETTA/PFP, PETTA/BM, PETTA/MP, g) PETTA/OH, h) PETTA/octane, I PETTA/N-BOC, and j) PETTA/N-BOC are used in the architecture of the materials (Cys). The inset in each panel shows a linked functional group.[92]

2.7.2. Electroless plating

To overcome this problem with low conductivity of the printed polymer, different coating methods (vapour phase deposition [139] micro electroplatings,[140,141], and sputter deposition[142]) have been developed to coat fabricated polymeric microstructures with conductive materials. The electroless plating approach has been most attractive because it is a simple, rapid, flexible, and low-cost process that can

deposit many metals onto polymeric templates. The resulting metal 3D structures obtained with this process and reported in the literature have demonstrated advantages in their controllability and well-defined size and shapes.[44,121,122,143–145]

This technique is an autocatalytic deposition procedure that coats nonconductive surfaces uniformly with thick metallic layers due to the reduction of metallic ions from a liquid electrolyte.[146] A continuous and compact metal coating on the substrate's surface can provide EP high conductivity.[147–149] Various reducing agents, including sodium borohydride,[150] vitamin C,[151] and hydroxylamine,[121] have been used. Among them, weaker reducing agents have shown more uniform metal deposition. This is because the strong reducing agents can synthesise unwanted metal nanoparticles in the solution rather than grow the seeds on the polymer. Using this approach, Kim et al.[152] have homogenously coated the 3D-printed microstructures with gold. This method used electroless gold plating at room temperature using an aqueous solution of $HAuCl_4$ and $NH_2OH.HCl$. (Fig. 14).

According to Kim et al., the uniform gold coating has been observed with SEM images. However, the slight pealing exists in Fig. 15 that can be due to the less affinity of the carboxylic acid group to the gold.

2.8.   Enzyme power output in the EFCs

Low EFC output limits their application options. EFCs are less powerful than metal-catalysed fuel cells and lithium-ion batteries. Most EFCs have 1 to 1000 μW cm^-^{2} power densities, with a few exceeding 1 mW cm^{-2}.[30] This poor power density may be traced back to three distinct areas: electron transport from enzyme to electrode,

catalytic surface area, and stability of enzyme activity. A combination of tailoring electrode materials, enzymes, and their interfaces, as well as smart configuration design, is needed to solve these issues.[3]

The power output by EFCs has increased dramatically over the past decade, allowing them to power implantable or portable devices.[153,154] Such advancements have been based mainly on a better knowledge of the parameters that control enzyme electrical wiring and the utilisation of conductive materials with a high surface area/volume ratio that may enhance enzyme loading. Studies have extensively looked into the use of new nano- and mesoporous materials for enzyme hosting, their functionalisation to improve enzyme wiring, modelling of pore structure and its effects on enzyme electroactivity and loading, and the role of high surface area in improving bioelectrode stability and enzyme loading.[155]

Most high-power density EFCs utilise carbon nanomaterials (CNM)-based electrodes.[30] As a result, CNMs, including Bucky paper carbon felt, carbon cloth, carbon black, CNTs, carbon fibre, graphene, porous carbon, carbon nanodots, and their mixes, have been widely used to make bioelectrodes. Their advantages include low cost, industrial scalability, a wide working potential window, chemical stability, hierarchical micro/nanostructures, and flexible structures. Because of the high specific surface area of CNMs, they can hold a lot of enzymes.[30] Although using CNMs-based high-surface-area electrodes allows for much higher current densities, there are still two significant challenges.

First and foremost, the toxicity of CNMs, particularly in implanted applications, should be addressed. Chronic diseases may result from long-term exposure to CNMs from portable devices.[30,156–158] Second, high enzyme loading does not necessarily equate to increased current density, the excess high enzyme concentrations may hinder fuel diffusion.[30,159,160] The previous study show that, due to enzyme loading in the large pores (150 nm) and better mass transfer, the larger holes (150 nm) produced higher current density than the smaller pores (35 nm).[161] Furthermore, some natural enzymes that can catalyse glucose reaction in EFCs, such as GOx, are unable to conduct DET on CNT or graphene-based electrodes because they are heavily glycosylated with a FAD group that is too deeply buried to allow direct ET.[162,163]

2.8.1.   Electron transfer (ET)

ET rate determines EFC power output. Electron transfer between enzyme and electrode might be direct (DET) or mediated (MET) (Fig. 19). Both have pros and cons. DET transports electrons directly to the electrode for bioelectrocatalysis, unlike MET, which needs a toxic external redox mediator. Due to enzyme properties, DET is simple and affordable, allowing near-zero overvoltage. The DET is more reliable and more suited for biological EFC development than the MET.[30,164] Using a high-conductivity electrode may aid increase current output by facilitating ET between enzyme and electrode and preventing energy loss through electrode-to-external-circuit transfer. For this reason, immobilising the enzyme on porous gold electrodes has gained interest because to its superior electrical conductivity, chemical stability, and biocompatibility. Au electrodes can also be easily functionalised via self-assembled

monolayers of thiol, diazonium grafting, and electropolymerisation.[30] In addition, the interaction between the enzyme and the gold nanoparticles was more beneficial for electron transfer than CNTs.[162,163,165]

According to Marcus' hypothesis, ET is controlled by reorganisation energy and donor-acceptor distance, which reduces by an order of magnitude for every 2.3 Å.[165,166] An upper threshold of 15 Å is required for DET to be effective. Thus, the enzyme's structure and conformation contain a cofactor near the electrode, boosting the ET rate and bioelectrode current density. On the other hand, many cofactors and active sites are locked inside insulating protein shells, presenting a barrier to successful long-distance ET rates.[166,167] This issue may be addressed by employing appropriate enzyme immobilisation, electrode surface modification for correct enzyme orientation, and enzyme engineering to bring the enzyme cofactor closer to the electrode surface, all of which will help DET for high-current-density bioelectrodes.
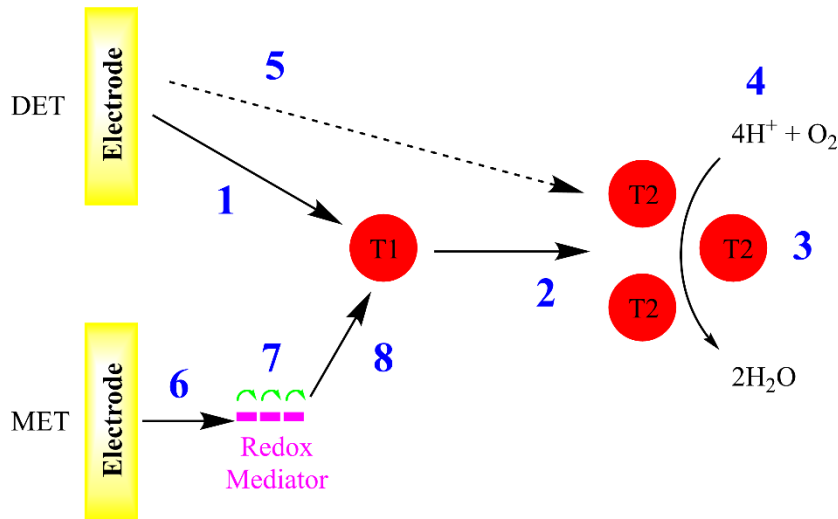
Fig. 19 Direct electron transfer (DET) and mediated electron transfer (MET) for immobilised. Electron transfers from electrode to T1; Steps 2–4: IET; Steps 3–4: O$_2$ reduction; Step 5: Hypothetical electron transfer from electrode to trinuclear cluster. Steps 6-8: Electron transport from electrode to redox mediator, then from redox mediator to T1.[168,169]

2.8.2. Enzyme stability

Enzyme stability influences EFC lifetime and power output. Stability is an enzyme's capacity to keep its active structural form despite disruptions like temperature increases.[170] Free enzymes present in nature are not stable, and many factors affect their activity.[171,172] Therefore, the enzyme immobilisation technique plays a pivotal role in both efficiency and biocompatibility of implantable EFCs.

A number of factors, including an enzyme's intrinsic instability, immobilisation-induced denaturation, conformational change, reorientation, and chemical inactivation, as well as inadequate enzyme/electrode contact, may lead to the relative instability of an enzymatic electrode.[168] Appropriate enzyme immobilisation fixes this

problem. Immobilising the right enzyme on conductive electrodes can increase enzyme loading, enzyme-substrate interaction, and electron transport.

2.8.3. Enzyme immobilisation techniques on the electrode

Enzyme activity, stability, and electron transport may be improved via electrode immobilisation. Immobilisation impacts bioelectrode stability by inhibiting enzyme dissociation.[173] This is because rigidifying the immobilised structure of an enzyme may prevent it from denature. As show in Fig. 20, enzyme immobilisation can be classified in four main section which will be summarised in following sections.[30,174]
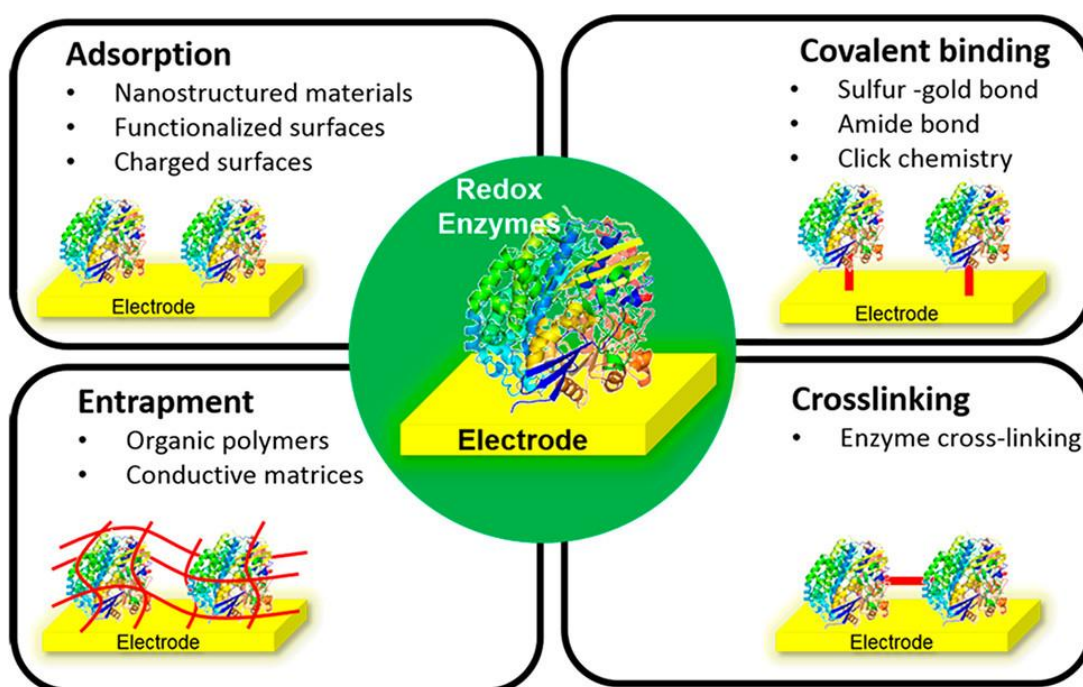
Fig. 20 Four main enzyme immobilisation techniques.[30] Adsorption: Enzymes bind to solid supports non-covalently, allowing separation. Covalent bonding: When enzymes are covalently attached to a solid support, they form a strong and permanent bond that ensures their stability and activity. Encapsulation: Enzymes are enclosed within a porous matrix or microcapsules, providing a protective environment for enzyme activity. Crosslinking: Enzymes are linked to solid supports using crosslinking agents, preventing enzyme release.

Adsorption:

Physical adsorption is the easiest approach to immobilising enzymes. For example, nucleic acids on the glucose oxidase enzymes are highly negatively charged and therefore can be readily adsorbed to electrode surfaces that are positively charged [175] or modified with a functional group such as amine,[176,177] and thiol,[178] through the ion exchange process.[179,180] On the other hand, positively charged enzymes can be immobilised onto negatively charged surfaces, such as silica or hydroxyapatite.[181] It is also possible to use the hydrophobic properties exhibited by many proteins to promote their adsorption onto hydrophobic surfaces. On hydrophobic surfaces, the enzyme-surface interaction may initially take longer to occur, as hydrophobic regions of the enzyme need to overcome the unfavourable water environment. Even so, once the enzyme adheres to the surface, there is a risk of denaturation due to the exposure of the internal hydrophobic core. This can disrupt the enzyme's structure and reduce its activity. On the other hand, hydrophilic surfaces retain enzyme structure and activity. The hydrophilic nature of the surface promotes favourable interactions with the aqueous environment, allowing the enzyme to maintain its native conformation and functionality. In this way, enzyme immobilisation on hydrophilic surfaces is more stable and effective.[182] However, adsorbed enzyme stability is often lower than other immobilisation approaches. In addition, immobilised enzyme bioanode stability depends on reaction conditions.[183]

Entrapment:

Entrapping enzymes within polymer matrices, organic and inorganic frameworks and immobilising them on the electrode surface may minimise leaching while preventing denaturation and conformational changes to the enzyme. With excellent enzyme activity and stability, entrapment is a relatively straightforward process.[184] Enzymes can be preserved in active forms by being placed in membrane-like matrices, such as hydrogel,[185] lipids,[186] and agarose,[187] which can replicate the natural environment of enzymes.[188] Such matrices cannot be employed for bioelectrocatalysis directly since they often have low conductivity.

High conductivity materials like CNTs and redox mediators like ferricyanide and ABTS have encapsulated the enzyme when making an enzymatic biofuel cell (Fig. 21).[189] El et al.[190] have demonstrated that 60 days of continuous monitoring of an MWCNT bioelectrode resulted in a constant current response, with more than 70% of the initial current remaining after six months of storage. However, this method has mass transfer issues. Therefore, designing a material with bigger pores and matrix is crucial. Matrix defects also may cause enzyme leaching, and porous materials leak fast.[183]
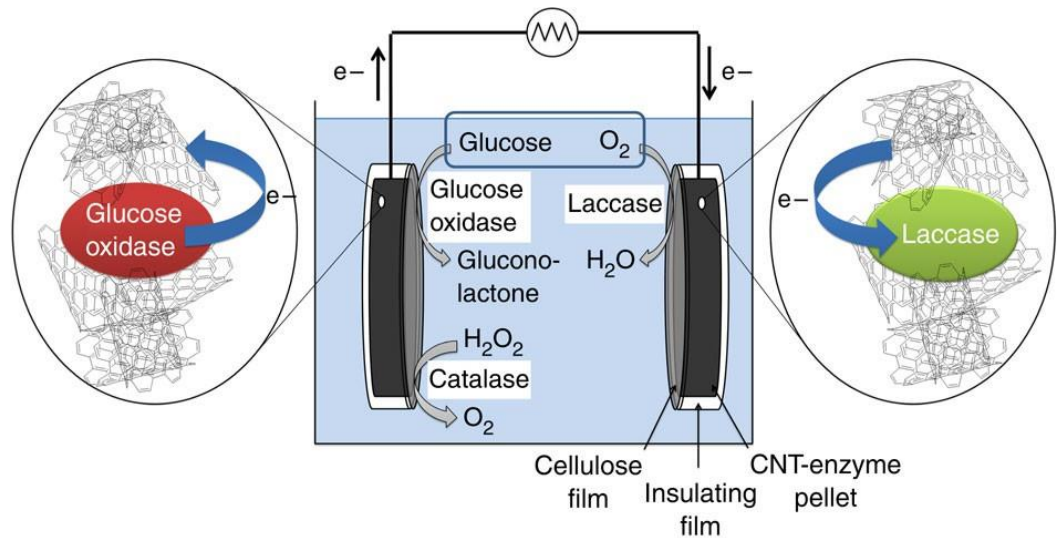
Fig. 21 Entrapping the enzyme within CNTs in full EFCs. The electrons are transferred from the GOX to the CNT during the anode conversion of glucose to gluconolactone. Catalase converts hydrogen peroxide into oxygen and water. After electrons are transferred from CNT to laccase, dioxygen is transformed into the water at the cathode.[189]

Crosslinking:

Cross-linking is a straightforward and efficient approach for immobilising enzymes on electrodes. Because the procedure is based on bi- or multifunctional reagent ligands, rigid enzymatic aggregation, which reduces enzyme leaching and increases stability, should be predicted.[191] A glutaraldehyde-crosslinking enzyme is remarkably stable. In the absence of glutaraldehyde, the catalytic current dropped and was substantially lower.[192,193] This may be because glutaraldehyde continuously reacts with enzyme molecules, resulting in their deformation and subsequent rigidification.

Cross-linking is a stable, reusable, and volumetric immobilisation approach for solid surfaces. Recent research found that enzyme precipitated coating (EPC) offers

excellent enzyme loading, activity, stability, and reusability.[194] This approach crosslinks enzymes on nanomaterials. Kim et al.[4] recently generated EFCs using an enhanced EPC technique, demonstrating the maximum enzyme activity with no GOx activity decrease during 270 days. However, heterogeneous enzyme orientation distribution, especially with cross-linkers, may delay ET speeds. This approach forms multiple layers of enzymes, increasing the distance between the outer layers and electrode and blocking electron transport (Fig. 22). In addition, the mass transport and loss the enzyme activity are two other main issues with this approach in the case of forming large enzyme clusters.[30,195]
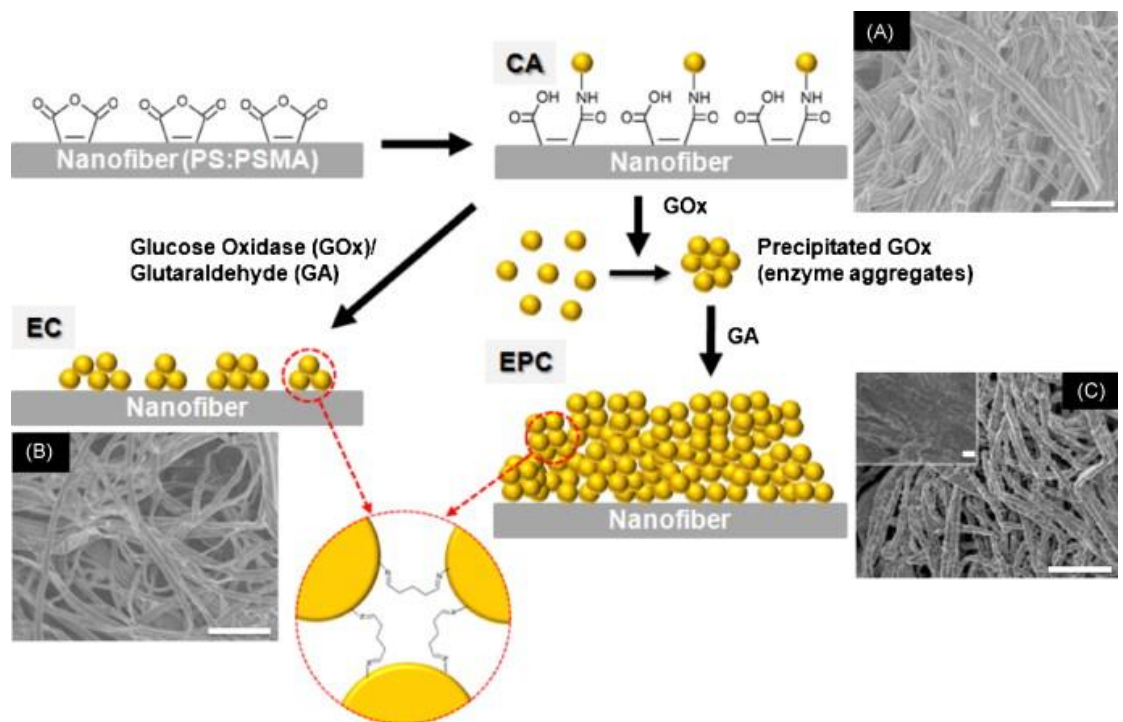
Fig. 22 is a schematic illustration of three different approaches to GOx immobilisation on MWCNTs. (a) covalent attachment (CA-GOx), (b) enzyme coating (EC-GOx), and (c) enzyme precipitate coating (EPC-GOx).[196]

Covalent binding:

The most common and efficient technique for immobilising enzymes is covalent binding. Creating amide bonds between carboxylic and amino groups, crosslinking with glutaraldehyde, or the EDC/NHS reaction on functionalised electrodes are typical methods to bind enzymes onto electrode surfaces.[197–202] Once a covalent connection is created, it is resistant to ionic strength and pH, which break non-covalently bonded molecules' adhesion to a surface.[203] Because of these characteristics, covalent functionalisation is appropriate for applications requiring long-term or continuous measurement modes, where bond stability contributes to signal stability over time and single-use sensing applications. Gutierrez-Sanchez et al.[198] demonstrated that the immobilised enzyme using this approach preserved more than 80% of the original current after 4000 s continuous measurement, whereas only 20% remained at the enzyme physically adsorbed onto mercaptohexanoic acid functionalised Au electrode. Immobilisation may reduce enzyme activity. This activity decrease may be caused by enzyme deformation from support interactions. Covalent immobilisation also affects interfacial electron transport and, ultimately, the lifespan of bioelectrodes.[30] Climent et al.[204] state the distance between the enzyme and electrode affects its current density. To improve electron transfer, the distance between the enzyme and current collector should be shorter than 8 carbons (12 angstroms). n < 8 reaches saturation, and n > 8 seems to drop exponentially for each additional carbon atom.

Covalent functionalisation chemistry relies on the surface, and biological components, so many procedures are investigated. These approaches may be characterised as random functionalisation protocols connecting randomly oriented biomolecules to the surface or oriented functionalisation procedures, which constrain binding orientation to certain and often desirable poses.

ENZYME IMMOBILISATION WITH RANDOM ORIENTATION

Random covalent immobilisation takes the use of biomolecules' surface functional groups. Primary amines like lysine residues are mainly targeted in GOx immobilisation due to their biomolecular frequency and nucleophilicity.[205] This approach is flexible and can be used to immobilise various enzymes. Immobilising the enzyme with the random orientation demonstrates excellent enzyme stability, as it can retain 88 per cent of its activity after 21 days.[206] This is because it results in multipoint attachment of the enzyme since more than one surface functional group is involved in bond formation and causes the firm attachment of the enzyme on the support.[207]

Several studies have been conducted, and numerous crosslinkers have been introduced because the surface binding linkers significantly impact the electrocatalytic enzyme performance. These chemicals primarily target three main biological functioning groups: amines,[191] carboxylates,[208] and thiols.[209] Some of the most widespread cross-linkers are 1-ethyl-3-(3-(dimethylamino)propyl)carbodiimide/N-hydroxysuccinimide (EDC/NHS), which cross-links carboxylates to amines,[206] and succinimidyl 4-(*N*-maleimidomethyl)cyclohexane-1-carboxylate (SMCC), which

connects thiols and amines (Fig. 23A).[210] Most cross-linking chemicals used today are heterobifunctional, limiting unwanted surface group cross-linking.[203] Glutaraldehyde cross-linking, one of the first techniques for enzyme immobilisation, works by firmly cross-linking amines via two amine-aldehyde bindings and promotes multipoint linkages (Fig. 23B).[205] For this reason, glutaraldehyde has been hailed as a an adaptable immobilisation crosslinker for the covalent attachment of enzymes. The glutaraldehyde and the enzyme have been immobilised using two different techniques.

- Without an enzyme, the crosslinking agent reacts with functional groups on the electrode surface, eliminating unreacted chemicals. Enzymes can then react with surface-bound cross-linker. This technique ensures a stable, uniform monolayer of immobilised biomolecules without protein aggregation (Fig. 23A).

- The enzyme first immobilises on the electrode with physical interaction, and then the glutaraldehyde is added to provide a crosslinking covalent bond.
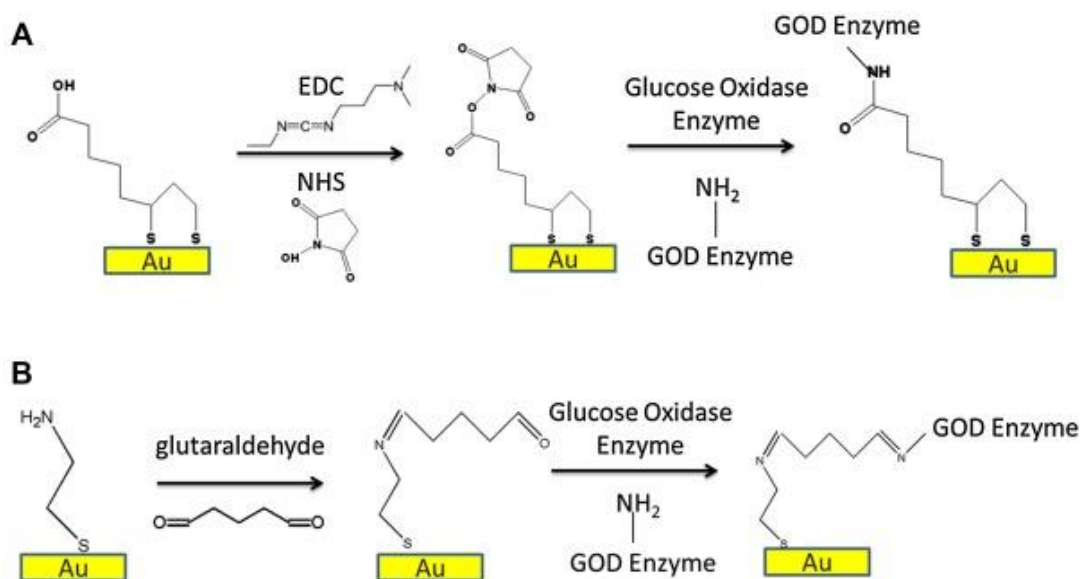
Fig. 23 A typical enzyme immobilisation methods used for random enzyme attachment on the gold: (A) EDC/NHS cross-linking, and (B) glutaraldehyde cross-linking.[206]

SPECIFIC ENZYME IMMOBILISATION

Although the excellent stability, versatility, and activity of the enzyme immobilisation with random orientation looks promising, the relative positions of the immobilised enzymes are random, and the orientations of the enzyme distribution are not uniform.[211] As a result, the enzyme's active site may be masked, or the distance between the active site and the electrode may be more than 15 Å (required distance for DET), affecting the ET between the electrode and the enzyme. In certain circumstances, immobilisation may reduce the stability of the enzyme, such as when the support may interact with the enzyme unfavourably.[174] Immobilisation of enzymes with specific orientation has been extensively investigated to enhance DET, stability,

and activity. These researches aimed to keep the enzyme's active site near the current collector to minimise the electron transfer distance.

ENZYME ENGINEERING TO ATTACH BINDING TAGS

Oriented covalent immobilisation is often chosen in these circumstances because it inserts binding tags at certain locations in the biomolecule to precisely regulate the placement of the covalent bond to the surface. The specific reactivity of these tags and the chosen electrode surface govern the functionalisation approach. The addition of binding tags that are easily attached during solid-state synthesis procedures is rather simple in the case of nucleic acid oligomers and peptides, and many industrial suppliers have the option to attach typical tags to termini, such as amines, thiols, azides, and more. The connected biomolecule is subsequently covalently bound to the sensing surface using these tags in processes similar to those previously reported. However, since conventional methods often make proteins, applying protein engineering techniques to add the required binding tags for orientated covalent functionalisation may be essential. For instance, orientated immobilisation may be achieved by introducing cysteine at specified sites in proteins using enzyme mutagenesis procedures and directly attach on the gold electrode (Fig. 24).[212] Zhang et al.[213] provided a dicysteine tag at the N-terminus of a D-sorbitol dehydrogenase in a recent example of cysteine tagging, enabling directed attachment of this protein to a vinylphenyl-coated surface. Lee et al.[214] tagged the streptococcal enzyme's N-terminus with cysteine residues for thiol–gold reactions. The thiol group on the cysteine molecule can make a strong covalent bond with gold, enabling the

enzyme's active site to stay close to the electrode. The thiol group on the enzyme bonds directly to the gold, unlike previous enzyme covalent immobilisation techniques. This method has been used to study enzyme immobilisation in various enzymes, including laccase,[215] glucose oxidase,[212] dehydrogenases,[216] and nitroreductase.[217]

However, this strategy has several flaws. A Cys-tag, for example, requires complex enzyme engineering. Multi-step enzyme mutation increases chemical cost and immobilisation time. This enzyme mutation may also impact stability and activity.[211] Mutations reduce specific activity by 45–85% compared to naturally produced enzymes, especially when active site residues are mutated.[218] In addition, enzyme attachment with a cys-tag depends on a single covalent link between the cysteine and electrode; hence, enzyme attachment reduces significantly since only one spot on the enzyme may bind to the gold electrode.
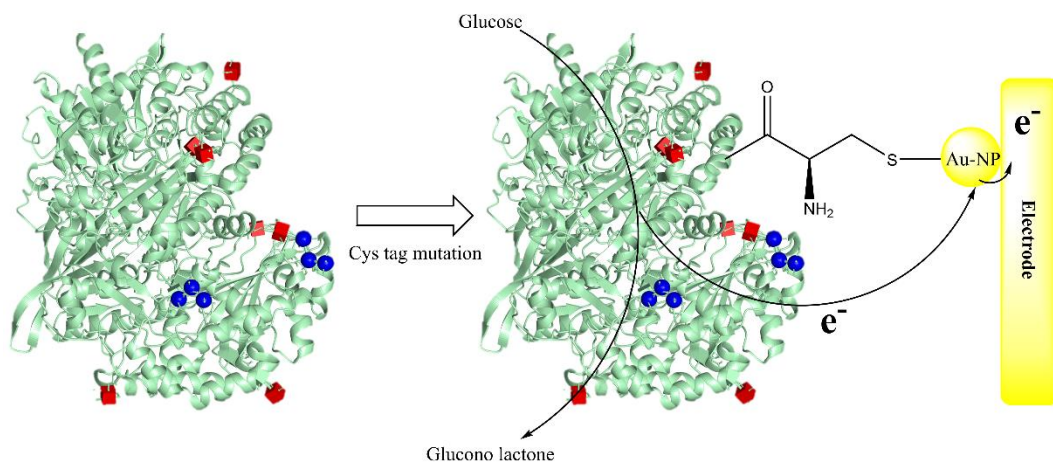
Fig. 24 Graph showing how genetically altered glucose oxidase is utilised to immobilise gold nanoparticles.[212] **Through the engineering techniques, GOx has been modified with Cys to possess specific binding properties that facilitate the immobilization of AuNPs.**

SELF-ASSEMBLED MONOLAYERS (SAMS)

One important element that has been used to induce orientation to the enzyme is the charge distribution on the protein surfaces.[30] The surface functionalisation of a gold electrode through the Self-assembled monolayers (SAM) offers various positive/negative/hydrophobic terminal functional groups, such as –COOH, –NH$_2$, –SO$_3$H, –CH$_3$, and –OH, which may affect enzyme orientation due charged functional groups of the electrode surface and charged amino acid residues of the enzyme according to its surface dipole moment.[211,219] Different functional groups on the surface of the enzyme can be introduced to change the orientation of the enzyme for immobilisation. For example, the ratio values for modified gold surfaces with aminoethylphenyl and carboxyethylphenyl layers indicate that the tilt angle of Laccase is higher in the case of a positively charged aminoethylphenyl layer (Fig. 25).[220]

This molecularly oriented laccase cathode showed 37% higher power density and 43% higher current density than the randomly bound laccase cathode.[221] SAM on the electrode surface protects enzymes from metal-enzyme interactions or an electric double layer at the electrode solution interface.[204]
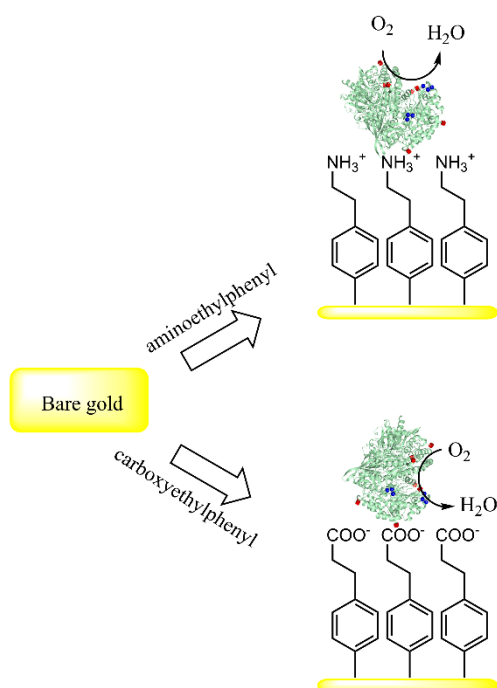
Fig. 25 Enzyme orientation with a different functional group on the gold surface.[220] **The figure shows the angle of the immobilised enzyme alters based on the type of the functional group on the substrate surface.**

Rüdiger et al.[219,222] immobilised hydrogenase on a gold electrode using this approach. 4-amino thiophenol was employed to functionalise the gold plate. The functionalised gold was then soaked in an enzyme solution to adsorb hydrogenase. Next, an EDC/NHS reaction was done on the gold electrode to cross-link the enzyme

and amine group (Fig. 26). Cyclic voltammetry demonstrated a considerable increase in DET due to the electrostatic impact of 4-aminothiophenol groups on gold.
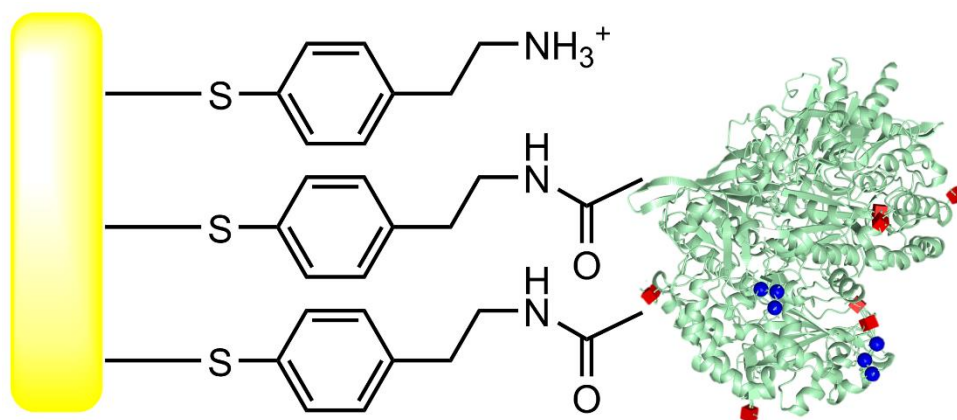
Fig. 26 Enzyme immobilisation through the Olaf et al.[222] process. To immobilize the enzyme, a 4-amino thiophenol amine is used to functionalize the gold surface with amine group.

SAM techniques are attractive candidates for surface tailoring because of their simple preparation from millimolar thiol solutions. Adsorption usually ends at the level of monolayer coverage, with a surface coverage on the order of pmol.cm^{-2}. However, the kind of thiol molecules, nature of the metal surface, immobilisation duration, and thiol concentration[223] all influence the layer's surface coverage, compactness, and organisation. By reducing pinhole flaws or conformational errors in the alkane chains, longer adsorption times and longer thiol chains are anticipated to produce a more structured SAM layer.[211,224]

The reduction of aryl-based diazonium salts is another common technique for preparing functionalised surfaces on carbon and gold electrodes (Fig. 27).[211,220] It is a

promising technique to amine-functionalise the substrate surface as it is capable of forming a stable bond with the substrate. The formation of mixed monolayers promotes surface functionalisation by repeated electrochemical reductions of a mixture of diazonium salts.[225–227] The disadvantage is the difficulty of halting the reaction at forming a monolayer. ET requires balancing a high ET rate and adequate organisation to create a regulated SAM. Electron grafting of aryl compounds on electrode surfaces involves generating and attaching highly reactive aryl radicals.[228] Pita et al.[227] functionalised the surface with amine groups by first immersing it in an azonium salt solution. After that, the electrodes were modified using 6-mercapto-1-hexanol (MH). This method provided several advantages to the modified surface. First, it covered areas not affected by diazonium salt, inhibiting enzyme physical adsorption, which may have led to its denaturation and diminished O_2 electro-redox reduction's potential. MH scraped out any biological waste that had adhered to the electrode. Third, a polar functional group (hydroxyl) that may establish hydrogen bonds, created by linking strong anchoring groups (aminophenyl rings) with flexible chains in the electrode nanolayer, should help immobilise protein molecules. As these enzymes oxidise substrates containing hydroxyl groups, hydroxyl groups on the electrode nanolayer may also promote enzyme orientation, as shown for cellobiose dehydrogenase.[202,227] This method improved the number of properly orientated laccase molecules seven-fold. (Fig. 27).
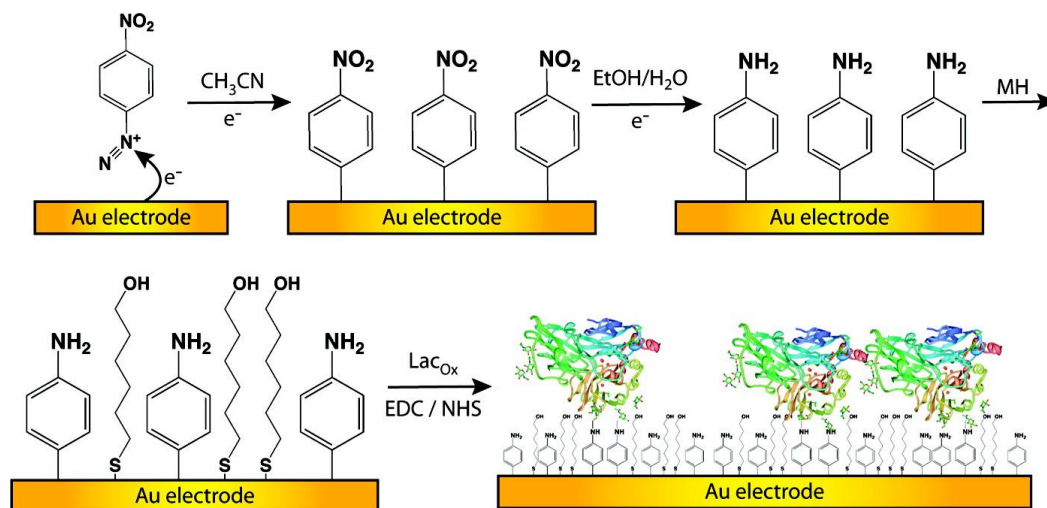
Fig. 27 Enzyme immobilisation through the Pita et al.[227] process. Gold plates were first immersed in an azonium salt solution to functionalize them with amine groups. MH was then used to modify the electrodes.

ENZYME ORIENTATION ADJUSTMENT

WITH THE PH

Changing the immobilisation pH may modify the orientation of enzyme molecules on the support, as protein group reactivity with the support is pH-dependent.[229] Dos Santos et al.[230] immobilised chymotrypsin on agarose at pH 5.0 to 10.0. Immobilisation decreased activity by up to 50% at pH 7 but had no effect at pH 5. This made the enzyme 4-5 times more stable than a formulation of glyoxyl agarose, which is stable and, in some cases, more active than the free enzyme (170 per cent for the enzyme immobilised at pH 10). By locating the region where multipoint covalent immobilisation is easiest, which varies across enzymes, it may be possible to shift the immobilisation orientation by adjusting the pH (Fig. 28). For instance, De Andrades et al.[231] found that Pectinex Ultra Clear glucose oxidase was the most stable at pH 5.0.

On the other hand, immobilisation of the same enzyme but from A. niger at pH 7.0 results in the highest stability. Tiago et al.[232] observed the enzyme's maximum stability at pH 5.0. This variance in pH immobilisation stability was likely mediated by enzyme orientation. The free enzyme was more stable than the immobilised enzyme at pH 7 but not at pHs 5 and 9. (by a 2 or a 6-fold ratio, respectively).
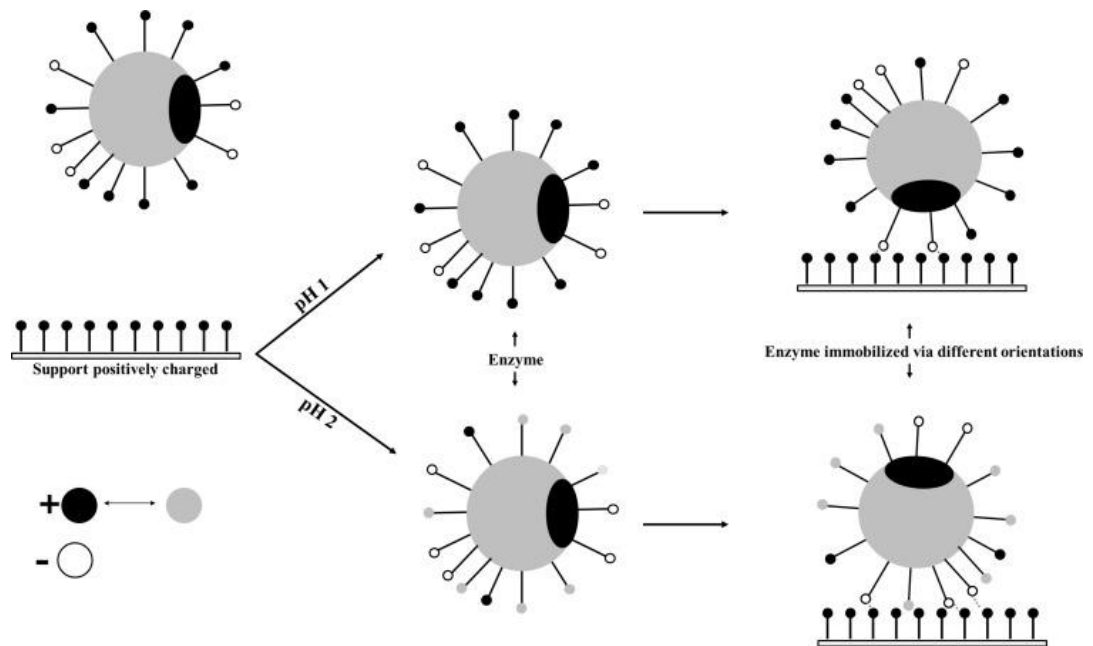
Fig. 28 The influence of immobilisation pH on enzyme surface orientation.[232] **The figure suggests that variations in pH can potentially alter the enzyme's surface charge, and eventually conformation and positioning of the enzyme molecules, thereby impacting their catalytic activity and overall performance in the immobilised state.**

2.9.   Knowledge gap

Significant research has been conducted over the last 20 years to enhance the immobilisation of the enzyme and employ nanomaterials as current collectors to boost the effectiveness of the EFCs. Even though the current density of EFCs has increased noticeably, the majority of EFCs created in literature are nanomaterials

made in simple disc or plate geometries, which hinders mass transfer and renders ET ineffective owing to weak conductivity. This problem may be resolved if a high conductivity 3D printed electrode can be produced. Among the techniques we've spoken about here, VP procedures provide the highest printing resolution. Although having high resolution, the properties of 3D-printed objects are influenced by as-mentioned variety of factors.[10] Particularly, the past efforts to create 3D electrodes using VP were not practical because of the printed part's poor mechanical qualities and low conductivity.[44] To employ VP for printing of the microelectrode in the implantable EFCs, further work must be done to obtain both high resolution and conductivity of the printed parts. This work sought to close this knowledge gap by attempting to find optimum silanisation reaction for effective metal deposition to achieve highest coating conductivity and adhesion.

A main challenge in coating the printed polymer with conductive metal is the low affinity between the metal and the printed part. This causes the metal film to peel off after coating. This problem may be resolved by properly functionalising the printed component with thiol. It has been shown that the metal adhesion can be considerably increased by salinizing the surfaces for thiol functionalisation. Therefore, several investigations have focused on assembling silane monolayers and multilayers for both rough and smooth surfaces. However, the influence of silanisation on the metal coating of the complicated 3D printed item has not yet been explored. There is no study being conducted to discover whether or not there is a relationship between the silanisation reaction conditions and the quality of the metal coating, and no link

between the adhesion and conductivity of the metal on the complex 3D-printed polymer is being completely explored. This knowledge gap may be closed by trying to print a silane- functionalised ink using DLP-based methods and analysing the surface chemistry of silanised 3D printed components.

The enzyme has to be immobilised on the electrode to serve as an EFC. Numerous efforts have been made to correctly immobilise the enzyme to increase its stability, activity, and ET. However, the optimum approach to attaching the enzyme to the gold electrode has not been compared thoroughly. This issue may be resolved by first determining the optimum method for immobilising the enzyme by testing it on Agarose and then extrapolating the protocol to the electrode that was 3D printed.

2.10. Conclusion of literature review

The most significant section of this literature review discusses the prospect of using various additive manufacturing (AM) methods to print microelectrodes and the immobilisation of enzymes on scaffolds for use in biomedical and industrial applications. Due to technology advancements, 3D printing has developed into a practical, effective, and affordable technique for creating customised electronics, hence supporting their uses in biosensing, biotransformation, and biological power production. Immobilised enzyme and substrate mass transfer as well as immobilised enzyme activity can be enhanced by more logical enzyme immobilisation processes and improved electrode design and manufacturing technology. Therefore, it is required to further improve the 3D printing materials for electrode creation and the

3 D - p r i n t i n g   o f   e n z y m a t i c
b i o f u e l   c e l l s
92 | P a g e

enzyme immobilisation technique. In the last ten years, conductive structure creation using 3D printing and enzyme immobilisation techniques has advanced significantly. Yet, various obstacles must be overcome in order to promote the technology to become a powerful instrument for developing EFCs.

First, although there have been many studies describing 3D-printed electrodes, there are still only a limited number of materials and printing methods that suitable for printing parts with high resolution and conductivity. To maximise catalytic surface area and immobilised enzyme quantity, high resolution is needed to build miniature porous structures with a large number of interconnected pores, while high conductivity is needed to improve electron communication between the enzyme and the current collector.[5,233] The incorporation of conductive nanoparticles into photosensitive ink is challenging because excessive nanomaterial loading of the photoresist is required to obtain adequate conductivity, and this affects the mechanical qualities of the printed part and the printing resolution of the photoresist.[67,84,85] Therefore, it is better to coat the 3D-printed polymer with metal to get both high conductivity and mechanical qualities.[10,121] To do this, it is necessary to perform more research and study on the printing materials, 3D printed part modification techniques, and metal adhesion on the 3D printed.

Second, when the enzyme is oriented optimally, it will function most effectively. The amount of electron transfer will decrease if the enzyme's active region is located distant from the electrode. In order to immobilise the enzyme with the optimum orientation, the immobilisation process should be controlled. Finding an optimised

protocol for enzyme immobilisation seems to be the most practical option when compared to other selective enzyme immobilisation techniques since it has no negative effects on the stability and function of the enzyme. Enzyme immobilisation on the natural substrate (e.g. agarose) can be tested and optimised in a straightforward and inexpensive manner.[207,234] This technique was used as part of this PhD research to determine whether immobilised enzymes were stable in a variety of functional groups. A pH test was also conducted on the stability of immobilised enzyme..[234]

In conclusion, the advent of 3D printing technology in EFC fabrication presents promising new avenues for developing implantable energy harvesting and biosensing applications in the industrial and medical sectors. Further research and improvement of enzyme immobilisation and material development for 3D printing will allow for improved efficiency, reduced costs, and customise the EFCs, which is challenging to accomplish with existing methods of EFCs manufacturing.

CHAPTER 3

3. Research Methodology

The method used to create the 3D enzymatic biofuel cells is summarised in Fig. 29; a more thorough explanation will be provided in the following sections.

Printable ink formulation	Surface functionalisation for gold coating	Enzyme immobilisation	Electrocatalytic characterisation
• Preparation of functional monomer • Optimising photoinitiator and photoabsorber concentration • Optimising the PµSLA printing parameters	• Optimising the surface functionalisation reaction time to achieve best coating adhesion and conductivity	• Finding the best functional group • Exploring the effect of pH on enzyme stability • Explore the immobilised enzyme activity and stability	• Setup the microelectrode • immobilise the enzyme • Cyclic voltametry analysis

Fig. 29 Schematic of the research methodology. The first step was to develop a functionalised printable ink. Second, the surface of the printed part was functionalised with thiol and then coated with gold. As a third step, an optimum enzyme immobilisation protocol was discovered. Lastly, the protocol was used to immobilise the enzyme on a 3D gold electrode to be used as an enzymatic bioanode.

3.1.   Materials

Irgacure®819, the photoinitiator used, was purchased from BASF. Apart ABTS, Agarose, and Horseradish peroxidase, all other chemicals were bought from Sigma-Aldrich and used without further purification. For the creation of the functional ink, tetraacrylate monomer, (3-mercaptopropyl) trimethoxysilane (95%) monomer functionalizing agent, hexylamine (99%) catalyst, and curcumin 98% (a photoabsorber) were used. The MPTMS sol-gel was made using ethanol (99.9%), hydrochloric acid (0.1 M), and thiol group to functionalise the surface of the printed part. The gold electroless plating solution was made using Gold(III) chloride trihydrate

(99.9%) and Hydroxylamine hydrochloride (99.9%) as a reducing agent. To optimise the enzyme immobilisation method, glucose oxidase ($\geq$ 100,000 units/g) from Aspergillus niger was used as a model enzyme and was bought from Sigma-Aldrich. We utilised and bought agarose from Agarose Bead Technologies to identify the best protocol for the enzyme immobilisation. The surface of the substrate was activated for the enzyme immobilisation using a solution of 25% Glutaraldehyde grade I, ethylenediamine, and cysteamine. Horseradish peroxidase (268 U/mg of protein) from Thermo Scientific, 2,2'-azino-bis(3-ethylbenzothiazoline-6-sulfonic acid) (ABTS) from Mannheim, and D-(+)-Glucose from Sigma-Aldrich were used for the enzyme activity test. The dielectric polymer paste and ferrocene methanol were acquired from Sun Chemical and Sigma-Aldrich, respectively, and used without further purification. Silver paint (RS PRO Conductive Lacquer) was bought from RS Components. Deionised (DI) water was used to make all of our aqueous solutions.

3.2. Methods

3.2.1. Synthesis of multifunctional acrylate monomer

The functional monomer was first made following Yee et al.[92] synthesis methods. The monomer was then combined with the different amount of the photoinitiator and photoabsorber to create photocurable ink for 3D printing. Briefly, equal moles of PETA (1.0 Equiv., 3 g, 8.51 mmol) and MPTMS (1.0 Equiv. 1.5 mL, 8.51 mmol) were stirred vigorously for five minutes. Hexylamine (0.1 Equiv., 0.111 mL, 0.85 mmol) was then added slowly, and the mixture was stirred overnight at 40 °C.

^{1}H NMR (500 MHz, CDCl$_3$) δ 6.45 – 6.35 (m, 2H), 6.15 – 6.06 (m, 2H), 5.91 – 5.82 (m, 2H), 4.31 – 4.09 (m, 8H), 3.71 – 3.63 (m, 1H), 3.56 (s, 9H), 3.52 – 3.42 (m, 1H), 2.80 – 2.68 (m, 3H), 2.66 – 2.50 (m, 4H), 1.74 – 1.65 (m, 2H), 1.63 (s, 1H), 1.26 (d, J = 15.3 Hz, 1H), 0.74 (dd, J = 9.7, 6.8 Hz, 2H). ^{13}C NMR (126 MHz, CDCl$_3$) δ 131.67, 127.48, 62.30, 50.43, 41.98, 34.50, 26.52, 22.76, 8.42.

3.2.2. Preparation of photocurable resin

The photocurable resin was prepared by adding curcumin of 0.5 wt% as a photoabsorber to the MP monomer. The mixture was stirred at 60°C for overnight. Then, Irgacure 819 of 1 wt% as a photoinitiator was added to the mixture. The reaction container was wrapped with aluminium foil to prevent photoreaction. The resin was stirred at room temperature for 12 h before printing.

3.2.3. Degree of polymerisation

The degree of polymerisation (DP) was determined by Fourier-transform infrared spectroscopy (FT-IR 4200, Shimadzu Co., Kyoto, Japan). Irgacure 819 was added to the MP monomer at different concentrations (0.5, 0.75, 1.0, 1.25, 1.5, and 1.75 wt%). The prepared photocurable resin was placed in a 40 μL standard aluminium sample pan and then photopolymerised using a UV lamp (396 nm) for 2 seconds. FT-IR spectra of cured polymer and uncured resin were analysed to calculate DP based on the peak areas of unsaturated C=C bond at 1650 cm^{-1} and a carbonyl group (C=O) at 1730 cm^{-1} using Equation 1.

$$\text{Equation 1} \quad \%DP = 1 - \frac{[Abs(C=C)]_{Polymer}}{[Abs(C=C)]_{monomer}} \times 100 = 1 -$$

$$\frac{[\int(C=C)/\int(C=O)]_{polymer} - [\int(C=C)/\int(C=O)]_{monomer}}{[\int(C=C)/\int(C=O)]_{monomer}} \times 100$$

3.2.4. 3D printing of microstructures

A projection micro stereolithography (PµSLA) system (nano Arch™ S130 by Boston Microfabrication (BMF) Precision Technology Inc.) was used to manufacture 3D polymeric microstructures. First, 3D lattice models with different surface areas and porosities were generated by AutoCAD software and digitally sliced into multiple layers with a 10 µm thickness of a single layer using BMF slicing software. Photopolymerisation in the PµSLA system was performed under UV laser exposure with the intensity of 80 mW/cm^2. The exposure time for the first layer was set at 10 seconds to increase the adhesion of a printed sample on the stage. The remaining layers were built with an irradiation time of 2 seconds and the delay time of 5 seconds for each layer. After printing, the sample was washed with acetone for 30 seconds to remove the residual resin. The 3D printed sample was then submerged in ethanol overnight to remove unreacted monomers trapped inside the polymer matrix.

3.2.5. Evaluation of spatial resolution of 3D printed structure

The spatial resolution of a 3D printed structure was evaluated by quantifying over polymerisation (OP) of a bridge shape model structure in z-direction using an optical microscope and ImageJ software. The OP was calculated using Equation 2.[235]

$$Equation\ 2\ \ OP = \left(\frac{t_{act} \times h_{des}}{t_{des} \times h_{act}} - 1\right) \times 100$$

where t_{act} is the thickness of the printed overhang, t_{des} is the thickness of the designed overhanging (0.2 mm), h_{act} is the height of the printed bridge, and h_{des} is the height of the designed bridge (0.84 mm).

Angular accuracy was determined by comparing the designed component's angle to the printed part's angle using the model structure of body-centred cubic (BCC) lattice (Fig. 37G). The angle of the printed part was measured from the scanning electron microscope (SEM) image using Autodesk Netfabb 2021 software. The following equation was used to calculate the angular precision:

Equation 3 $Angular\ precision = \frac{Angle\ of\ the\ designed\ part}{Angle\ of\ printed\ part} \times 100$

3.2.6. Thiol-functionalisation of 3D polymer structures

The 3D-printed polymer has shown that the material's surface contains significant silanol groups used in the subsequent surface treatment procedure to provide the ideal surface for gold coating. The reaction time for surface functionalisation was optimised to provide the maximum adhesion and conductivity of the coating. The sol-gel method was utilised to introduce thiol groups on the surface of the 3D printed structure by following the protocol described by Jia et al.[236] Briefly, the mixture of MPTMS with water at a 1:4 volume ratio, 10% (v/v) of ethanol and 3.3% (v/v) of 0.1 M hydrochloric acid was stirred at room temperature for 30 minutes. The resulting mixture was stored under ambient conditions for two hours.

The 3D printed polymer structure was submerged in the prepared MPTMS solution for surface modification. The reaction time from one hour to three days was investigated to find the optimal reaction time for introducing the highest thiol functional groups. The sample was then immersed in ethanol for 12 hours to ensure that unreacted MPTMS molecules were removed entirely.

3.2.7. Electroless gold plating

The electroless gold plating process began with a seeding step that involved immersing the thiol functionalised polymer (SG-MP) microstructures in the gold nanoparticle solution (5.5×10^{13} particles/mL) for 30 minutes and then sonicating the solution for one minute in degas mode to remove any trapped bubbles within the 3D printed lattice structure. The sample was thoroughly washed with water three times using a bath sonicator in the delicate mode to remove unattached gold nanoparticles. After the seeding step, the sample was submerged in 0.5 mL $HAuCl_4.3H_2O$ solution (5 mg/mL) and sonicated for 10 seconds in degas mode. The electroless plating process was initiated by adding 0.5 mL of hydroxylamine solution (40 mg/mL) as a reducing agent and sonicating the solution in a delicate mode. The electroless plating reaction was completed within 7 minutes. The gold-coated microstructure was then washed with deionised water three times.

3.2.8. Mechanical adhesion test

The mechanical adhesion between the deposited gold and the polymer substrate was measured by sticking a high-performance clear 3M scotch tape to a 3D-printed metallised polymer and then sharply peeling it off at an angle of 90 degrees. The sample was analysed with EDX mapping before and after the tape test to measure the adhesion of the deposited gold (Fig. 49). From EDX mapping images, the area of gold was calculated using ImageJ software. The adhesion of the deposited gold was determined using the following equation:

Equation 4 $Adhesion\ of\ deposited\ gold =$

$$\frac{Area\ of\ remained\ gold\ after\ tape\ test}{Area\ of\ deposited\ gold\ before\ tape\ test} \times 100$$

3.2.9. Enzyme immobilisation

In order to get the enzyme immobilisation, the gold surface was first functionalised by immersing it in a 1M solution of cysteamine over the night while shaking it on the roller. After thorough washing, the electrode was placed in a PBS buffer solution containing 5 µg/mL of the GOx enzyme in 5 mM PBS for an hour. The electrode was then washed to remove unimmobilised enzymes. The electrode was then immersed into the 1% (v/v) glutaraldehyde diluted in 50 mM of PBS at pH 7.0, and the mixture was shaken for an hour to modify the amino groups on the enzyme and support and permit the reaction between these groups located in the enzyme and the gold. The immobilised enzyme was then washed and resuspended overnight in PBS pH 8 (100mM) to maximise the enzyme-support reaction. The amount of immobilised enzyme was estimated by comparing the activity of the enzyme solution before and after the enzyme immobilisation process.

3.2.10.   Preparation   of   monoaminoethyl-N-ethyl-agarose (MANAE-agarose) supports

Monoaminoethyl-N-ethyl-agarose (MANAE-agarose) was prepared according to Fernandez-Lafuente et al.[237] This support was made by adding 200 ml of 2 M ethylenediamine (EDA) solution at pH 10 to 35 g of glyoxyl-agarose support that was already made. After 2 hours of moderate agitation, a final concentration of 10 mg/ml

sodium borohydride was added. After 2 hours of gentle agitation, the MANAE-agarose support was rinsed with 100 mM acetate buffer pH 4, 100 mM borate buffer pH 9, and then distilled water.

3.2.11. Preparation of glutaraldehyde supports

According to Vieira et al.[238], glutaraldehyde support was created by activating the primary amino groups of MANAE-agarose. 20 grams of MANAE-agarose were suspended in 22.4 millilitres of 200 millimoles of sodium phosphate buffer with a pH of 7. Following the addition of 33.6 ml of a 25% glutaraldehyde solution, the system was stirred gently for 16 hours at room temperature. The activated support was afterwards rinsed with water and vacuum-dried.

3.3.   Equipment
3.3.1. PµSLA

3D polymeric microstructures were created using projection micro stereolithography (PµSLA) equipment (nano ArchTM S130 by Boston Microfabrication (BMF) Precision Technology Inc.). First, using BMF slicing software, 3D lattice models with various surface areas and porosities were digitally sliced into several layers, each layer having a thickness of 10 micrometres. The PµSLA system's photopolymerisation process was carried out using a UV laser with an intensity of 80 mW/cm2. To ensure that a printed sample adhered well to the stage, the exposure period for the first layer was set at 10 seconds. The subsequent layers were constructed with a delay time of 5 seconds between each layer and an irradiation period of 2 seconds. To remove any remaining resin, the sample was rinsed with acetone for 30 seconds after printing. To eliminate unreacted monomers trapped within the polymer matrix, the 3D printed sample was subsequently immersed in ethanol for over night.

3.3.2. NMR

^1H and ^{13}C NMR Spectroscopy: NMR spectra were taken in deuterated chloroform on a Varian 500 MHz spectrometer. ^1H and ^{13}C chemical shifts were referenced relative to $CDCl_3$ (δ = 7.26 for ^1H and δ = 77.16 for ^{13}C). ^{19}F chemical shifts were referenced automatically by the VnmrJ software program.

3.3.3. FIB-SEM

FIB-SEM (Zeiss crossbeam 550 microscope) was used to examine the cross-section of the conductive 3D gold microstructure and measure the thickness of the coated gold layer. In the microscope, the sample was tilted at an angle of 54 degrees.

The Ga$^+$ beam was used to dig the rectangle (20 μm × 5 μm) at 30 nA. The Ga$^+$ laser was then used for trenching the surface slice by slice. During SEM imaging, the in-lens backscattered detector was operated at 2 kV to acquire cross-section images.

3.3.4. SEM

SEM (Hitachi TM 3030) coupled with an energy-dispersive X-ray (EDX) analyser was used to examine the printing resolution, uniformity of gold layer and chemical composition of 3D gold-deposited polymer microstructures.

3.3.5. XPS

The samples were analysed using the Kratos AXIS ULTRA with a monochromatic Al kα X-ray source (1486.6 eV) operated at 10 mA emission current and 12 kV anode potential (120 W). The spectra were acquired with the Kratos VISION II software. A charge neutraliser filament was used to prevent surface charging. The survey spectra (binding energy range from 1400 eV to -5 eV) were acquired at a pass energy of 80 eV, a step of 0.5 eV and a sweep time of 20 minutes and used to estimate the total atomic % of the detected elements. The high-resolution spectra at pass energy of 20 eV, a step of 0.1 eV, and sweep times of 10 minutes were also acquired for photoelectron peaks from the detected elements. The spectra were charge corrected to the C 1s peak (adventitious carbon) set to 284.8 eV. Casa XPS software (version 2.3.19 PR1.0) was used for peak fitting and quantification.

3.3.6. ToF-SIMS

ToF-SIMS was carried out using a ToF-SIMS IV instrument (IONTOF GmbH). Secondary ion mass spectra were acquired using a 25 keV Bi^{3+} primary ion beam delivering 0.3 pA in negative ion polarity mode. The primary ion beam was raster

scanned over different areas with the total ion dose kept under the static limit of 10^{13} ions/cm^2 for surface analysis. The ToF analyser was set with 200 μs cycle time, resulting in a mass range between 0 and 3490 mass units and a low-energy (20 eV) electron flood gun was employed to neutralise charge build-up. ToF-SIMS depth profiling was done in dual-beam mode by raster scanning the 25 keV Bi^{3+} primary ion beam over a 100 × 100 μm^2 region at the centre of 300 × 300 μm^2 sputter craters formed using a 5 keV Ar$_{1400}$ gas cluster ion beam (GCIB) delivering 1.5 nA (higher depth resolution for near surface analysis) and 5 keV Ar$_{1900}$ GCIB delivering 12 nA (lower depth resolution for reaching buried interface). The measurement was performed in the "non-interlaced" mode with a low-energy (20 eV) electron flood gun employed to neutralise charge build-up. Data analysis was done using SurfaceLab 7.1. All ToF-SIMS intensity maps were normalised by total ion counts to correct for topographic features and subsequently normalised by the maximum profile intensity of each secondary ion. Optical profilometry was used to determine crater depths after ToF-SIMS depth profiling experiments and calibrate the depth scale in combination with information obtained by FIB-SEM. Scans were obtained using a Zeta-20 optical microscope (Zeta Instruments) in a Z range of 4.6 μm. The number of steps was set to 328, allowing for a *z*-step size of 14 nm.

3.3.7. Mechanical adhesion test

The mechanical adhesion between the deposited gold and the polymer substrate was measured by sticking a high-performance clear 3M scotch tape to a 3D-printed metallised polymer and then sharply peeling it off at an angle of 90 degrees.

The sample was analysed with EDX mapping before and after the tape test to measure the adhesion of the deposited gold. From EDX mapping images, the area of gold was calculated using ImageJ software. The adhesion of the deposited gold was determined using the following equation:

Equation 5 $Adhesion\ of\ deposited\ gold =$

$$\frac{Area\ of\ remained\ gold\ after\ tape\ test}{Area\ of\ deposited\ gold\ before\ tape\ test} \times 100$$

3.3.8. Conductivity measurements

The conductive 3D gold electrode (2 mm × 2 mm × 0.5 mm) was manufactured, and its sheet resistance (R_s) was measured using the Van der Pauw technique.[239] Horizontal resistance (R_H) and vertical resistance (R_V) were measured using a four-probe micromanipulator system (Micromanipulator, model MM 450PM) and a source meter (Keithley 2400, Tektronix Inc., Shanghai, China) and R_s was calculated using Equation 6. The average R_s was taken from three independent measurements.

The conductivity (σ) of the deposited gold was calculated using Equation 7, where the ρ is the resistivity and t is the thickness of the gold film acquired from FIB-SEM analysis.

Equation 6 R_s: $e^{-\pi R_H/\pi R_S} + e^{-\pi R_v/\pi R_S} = 1$

Equation 7 $\sigma = \dfrac{1}{R_s t}$

3.3.9. Enzyme activity determination

The activity of GOx was determined by recording the increase in absorbance at 414 nm produced by the oxidation of the ABTS® (ε 414 = 36,000 M^{-1} cm^{-1} under these

conditions) using a spectrophotometer V-730 Jasco (Madrid, Spain) thermoregulated at 25 ºC with magnetic stirring. The ABTS® assay was performed using 1.8 mL of 100 mM of PBS at pH 7.0 containing 0.5 mL of *D*-Glucose at 1M, 100 µL of ABTS® at 10 mg/mL prepared in 100 mM of PBS at pH 7.0 and 50 µL of horseradish peroxidase at 0.1 mg/mL prepared in 100 mM of PBS at pH 6.0. It was checked that the activity values were maintained if using half or double of peroxidase, confirming that the activity depends only on the amount of glucose oxidase. The reaction started when 50 µL of the solution was added. One unit (U) of activity was defined as the amount of enzyme that oxidises 1 µmol of substrate per minute under the specified conditions.

3.3.10.   Electrochemical characterisation

This gold-coated microelectrode was used to create an enzymatic bioanode. The enzyme immobilisation was first tested on agarose to determine the best methodology for immobilizing the enzyme. The optimum reaction protocol was then applied to the enzyme immobilised on a gold electrode. A cyclic voltametry test was performed on the gold electrode that had been immobilised with an enzyme to measure the electrode's current output.

All electrochemical characterisations were performed using an Autolab PGSTAT30 potentiostat/galvanostat from Metrohm Autolab (Utrecht, The Netherlands) employing a three-electrode setup with a bioanode electrode as a working electrode, a platinum mesh as a counter electrode, and the Ag/AgCl (3 M KCl) as a reference electrode. To prepare the working electrode, an insulated copper wire

was connected to the gold-coated electrode using silver paint and insulated with a dielectric polymer before the enzyme immobilisation process.

The electrodes were immersed in phosphate buffer saline (PBS) (100 mM) pH 7.0. Before characterising the anode, N_2 was bubbled into the electrochemical cell for 10 min. Ferrocene methanol (0.5 mM) and glucose (50 mM) were added to the buffer as a mediator and a substrate, respectively. Cyclic voltammetry (CV) was used for electrochemical analysis at a scan rate of 10 mV/s. All potentials are presented in relation to the standard hydrogen electrode (SHE).

CHAPTER 4

4. Inks formulation and 3D-printing of functional polymers

4.1. Introduction

Three-dimensional (3D) conductive microstructures fabrication has gained great interest in the past decade for use in microelectronics applications,[240,241] micro/nano-electrochemical systems[242] and sensors.[48,243,244] 3D microelectrodes have a large surface area to volume ratio, which increases the catalytic surface and improves the efficiency of enzymatic biofuel cells and electrochemical sensing sensitivity.[245–247] In addition, the electrodes' 3D structure is beneficial for bioelectrochemistry and tissue engineering applications since they more closely resemble the three-dimensional structure of cells.[246,248,249] Moreover, a high surface area is required for better overall electrode performance. Ideal 3D microelectrodes are sought after for their low electrical resistivity, structural and chemical stability, repeatability, and low production costs.

Extensive research has been done on several manufacturing techniques, including injection moulding,[250,251] electroplatings,[252,253] screen printing[254] and microfluidics[255] to manufacture 3D-microelectrodes. However, all these techniques are restricted in their practical use due to their poor conductivity, high cost, and limited manufacturability. Because of these factors, subtractive techniques are still used to manufacture 3D microelectrodes, which are time-consuming, limited geometries, and are prone to surface damage.[44] In contrast to subtractive

manufacturing, additive manufacturing (AM) employs several additive processes to build arbitrarily complex structures of different sizes.

As mentioned in the literature review, various AM methods such as extrusion,[256,257] powder bed fusion,[258] inkjet printing,[259] were used to make 3D microelectrodes. However, all these techniques for manufacturing microstructures have a limited resolution and electrical conductivity. For example, Blasco et al.[260] effectively printed highly conductive microstructures using Direct laser writing (DLW), creating conductive lines as small as 1 micrometer. It consists of a one-step process where the intense heat generated by the closely confined laser spot converts metal salts to metal atoms and forms nuclei (seeds) for future development into nanoparticles. However, the resistance value produced by DLW was much higher than the value typically utilised in electronics,[44] mainly due to separate metallic lines within the polymer matrix.[79] Additionally, the DLW cannot print arbitrary 3D shapes with a high resolution because the nanoparticles generated in the photoresist scatter and obstruct laser light, leading to unwanted polymerisation and metal nanoparticle formation during laser irradiation,[84,85] Thus, improving conductivity and printability with this technique requires an extensive and sophisticated photoresist formulation procedure.

Furthermore, this strategy is effective only if the working area of the target does not exceed the size of the structure, which is usually is few hundred micrometers. A building with a larger dimension must be created from separate parts and then

stitched together in a precise sequence. This method fabricates inter-part connections, influencing the structure's print speed, integrity, and conductivity.

Projection micro stereolithography (PμSLA) is another AM method that has recently gained much interest as it can create 3D components in a wide range of sizes, from the microscale to the macroscale. The PμSLA has proven beneficial in several areas such as tissue engineering,[114,261,262] optical components,[263] anti-counterfeiting labellings,[264] and manufacturing of bioinspired engineering materials and structures.[265–267] In this technique, the 3D-designed part first converts to 2D patterns, projecting on the resin surface (Fig. 30 B). This process repeats to the UV projector on the next layer on the platform. The procedure repeats until the whole structure is built. This technique has also attempted to create conductive 3D structures with this technique by adding conductive nanomaterials into the photocurable resin.[67,268] The printed part's poor conductivity prevented it from being used as an electrode in real applications.

The method for producing 3D-printed polymers with functional groups on their surfaces—surfaces that are easily modified with additional functional groups for metal attachments—is described in this chapter. The photocurable resin was formulated by adding photo initiators with varying quantities to get the highest level of photopolymerisation. To provide the controllability in photopolymerisation throughout the printing process, curcumin, a biocompatible photo absorber, was then added. Then, all printing settings were optimised to achieve a compromise between printing speed and quality (Fig. 30 B). This approach may create 3D-printed parts that

can subsequently be functionalised with the appropriate chemical group to bind organic or inorganic molecules (Fig. 30 C).
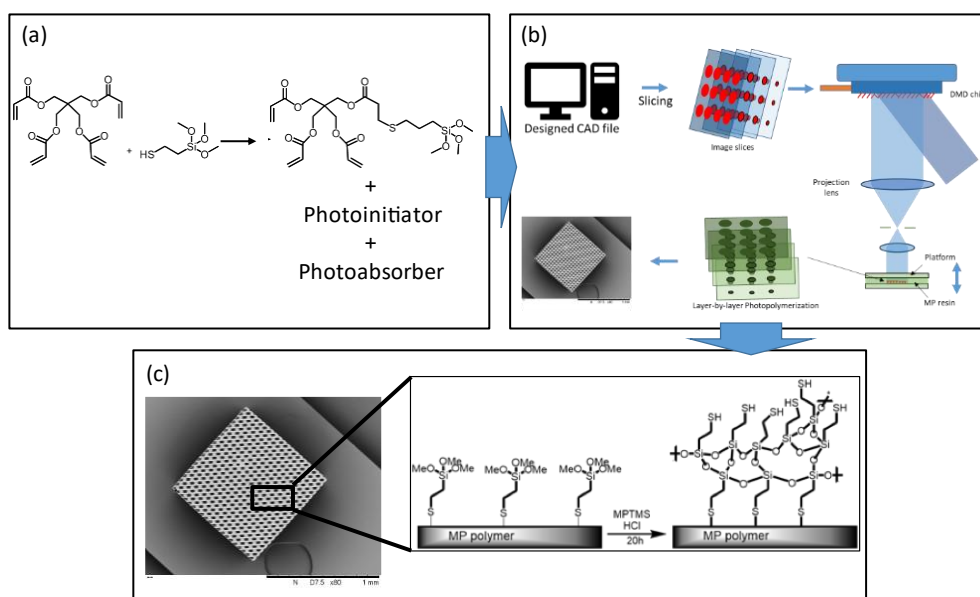
Fig. 30 Process for the preparation of conductive 3D-microstructures: (A) Preparation of functional resin for the Michael-thiol reaction between PETTA and MPTMS, (B) 3D-printing of functional resin using PµSLA, (C) surface functionalisation via sol-gel reaction

4.2. Photocurable ink formulation

As indicated in section 2.6.1, the photocurable ink comprises three main components: acrylic monomer, photoinitiator, and photoabsorber. These ink components were carefully chosen for this project, and each concentration was optimised to provide the part's optimum printability, physical qualities, and chemical properties.

4.2.1. Monomer Preparation

Acrylate monomers are often used as a monomer in all vat-photopolymerisation techniques (for the reasons explained in section 2.6.2). However, most printed

polymers do not feature functional groups like thiol and amine groups on the surface to improve coating adherence after photocuring these traditional monomers. Michael-thiol reaction was also used by Yee et al. to produce a series of PETTA derivatives functionalised with different groups to be used as functional monomers. Such photoresist provided PETTA's admirable crosslinking and writing resolution while producing a surface with various functions of quite diverse kinds.[85,92] The functionalised acrylate was synthesised by reacting the multifunctional acrylate, PETTA, with a thiol via the thiol-Michael reaction in a 1:1 molar ratio. Using a 1:1 molar ratio, they ensured that the final monomer mixture had an average of three acrylates per one monomer molecule, sufficient for effective crosslinking. It is feasible to add a silanol group to the monomer molecules by careful monomer design, allowing them to remain on the surface after printing. The presence of trimethoxysilane on the polymer surface opens up the option of using MPTMS sol-gel chemistry to attach thiol groups to the surface of these structures. Therefore, the (3-Mercaptopropyl) trimethoxysilane (MPTMS) was chosen to be reacted with PETTA, as shown in Fig. 30A.

^{1}H and ^{13}C NMR analysis revealed the successful thiol-Michael reaction for the monomer synthesis. Fig. 31 shows the chemical structures of PETTA and MPTMS functionalised PETTA (MP). The signals at 50.5 ppm and 8.25 ppm attributed to the carbons for methoxy and $SiCH_2$, respectively (Fig. 31b). Fig. 31f confirmed the existence of MPTMS molecules in the monomer. In Fig. 31 a, c, d, and e, the presence of signals shifts attributed to CH_2 at 170.73, 34.60, 26.62, and 22.86 ppm verified the

MPTMS addition on PETTA structures, which are not present in the PETTA prior to

functionalisation.
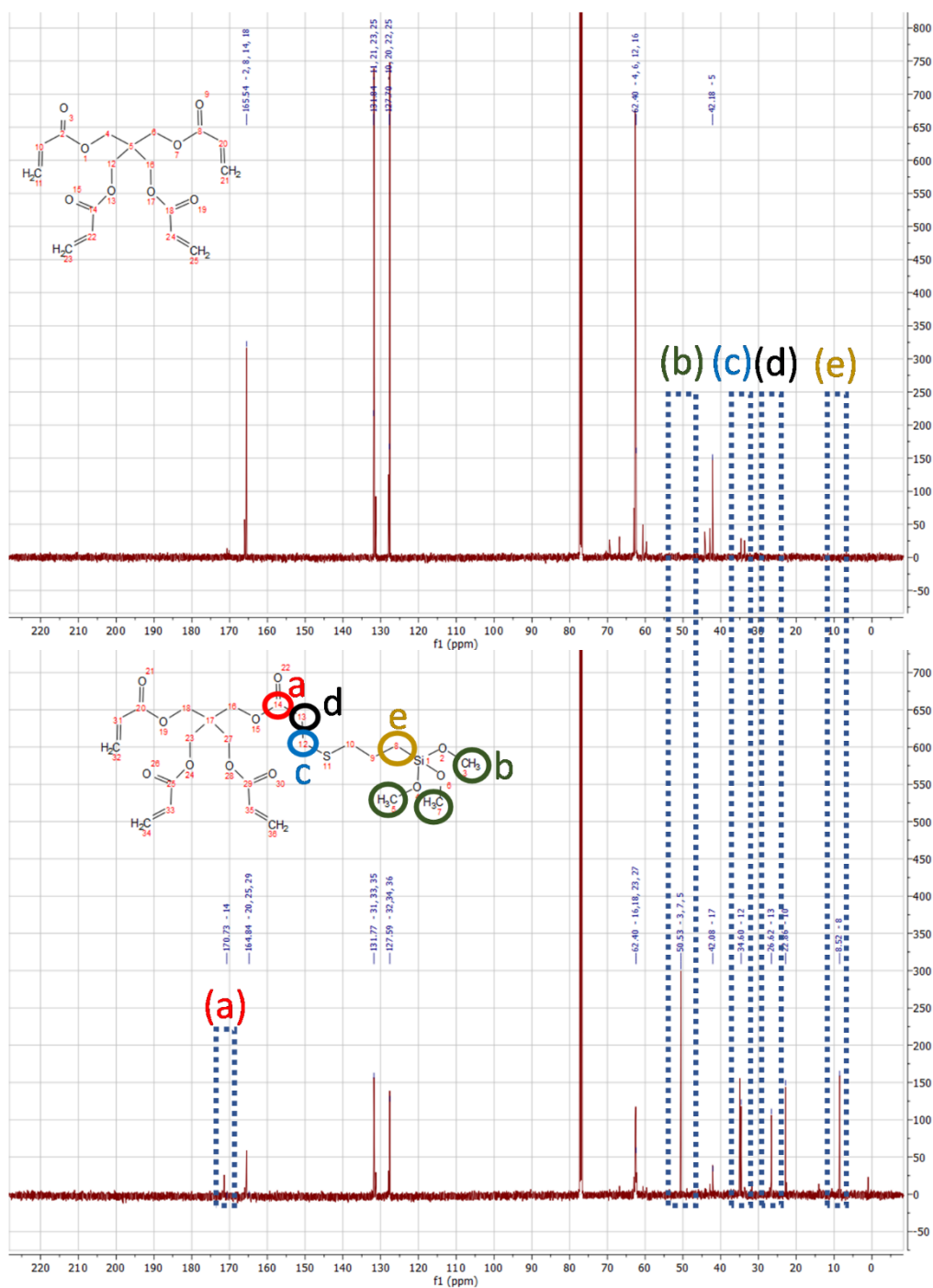
Fig. 31 ^{13}CNMR of PETTA And MP WITH MPTMS comparison before and after Michaele-thiol addition. The figure shows successful binding of MPTMS to PETTA.

The triplet signals assigned (2.75 and 2.60 ppm) in Fig. 32's ^{1}HNMR further demonstrate the effectiveness of the Michael-thiol reaction by highlighting the link between PETTA and MPTMS. The presence of the singlet signal shows the existence of methoxy groups connected to the MPTMS molecule (3.55 ppm). Another evidence that MPTMS molecules are present in the monomer is the triplet signal with the assigned number 8. To conclude the NMR analysis, it can be confirmed that the Michael-thiol reaction between the PETTA and MPTMS was successful. Therefore, after printing of this monomer, it is expected that to have free silanol group on the polymer after printing for further functionalisation.
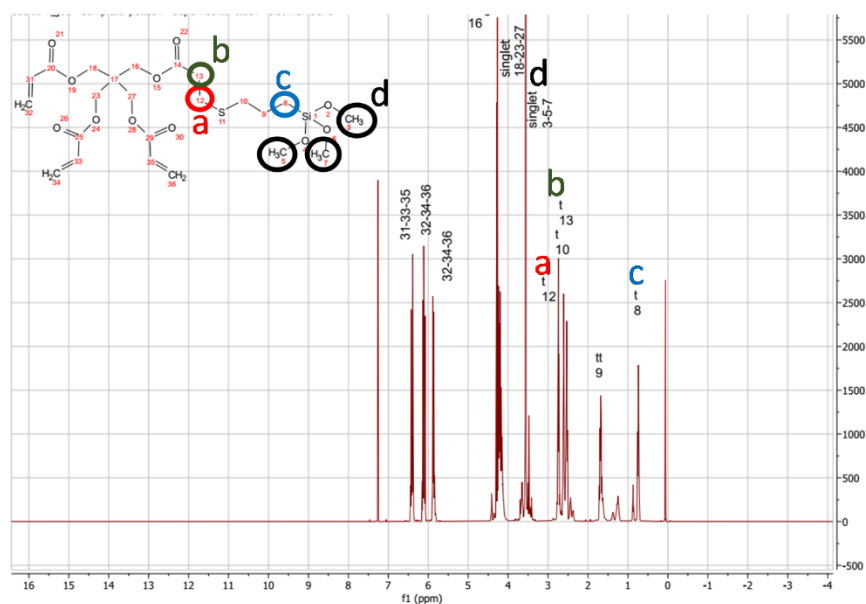
Fig. 32 ^{1}H NMR spectra of the MP. NMR results confirm binding of MPTMS to PETTA.

The monomer's viscosity is a significant variable that directly affects printing speed because, in the VP printing process, replacing a new resin layer takes longer

when the monomer's viscosity is higher. In order to accomplish reliable printing, the resin's viscosity should be less than 5 Pa s.[269] The MP monomer developed for this study has a viscosity of 0.94 Pa at a shear rate of 10 S^{-1}, demonstrating that the viscosity is adequate for printing (Fig. 33).
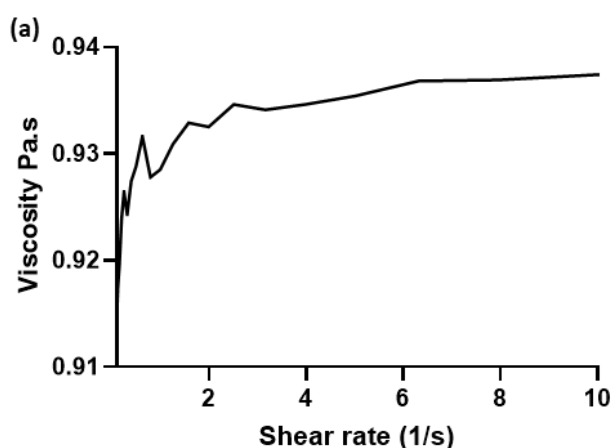
Fig. 33 The results of rheological investigation done on MP monomer using a rotating rheometer.

4.2.2. Optimising photoinitiator concentration

After successful preparation of the monomer, the photoinitiator was added to the monomer, to make it UV curable. Irgacure 819 was selected because of its biocompatibility, which opens up the possibility of using 3D printed microstructures for bioelectronic devices such as implantable biofuel cells (as detailed in more detail in section 2.6.3).[113,270,271] To find the optimal amount of photoinitiator, the degree of polymerisation (DP) analysis was performed as the efficiency of the reaction between monomers is anticipated to impact the printed polymer's mechanical and physical characteristics.[272]

As shown in Fig. 34A, during the polymerisation of MP, the C=C group of acrylate binds together to form a single C-C link. Therefore, through the FTIR analysis, the degree of polymerisation can be estimated by considering the reduction in alkene area and rise in alkane area (Fig. 34B). Equation 1 has been used to calculate the DP. The optimal concentration of Irgacure 819 to achieve the highest DP was determined to be 1 wt% using Fourier transform infrared (FTIR) spectroscopy at different concentrations ranging from 0.5 wt% to 1.75 wt%. The DP, calculated from the peak areas of unsaturated C=C bond at 1650 cm^{-1} and C=O bond at 1730 cm^{-1} of uncured resin and cured polymers (MP polymer), increased with the concentration of Irgacure 819 up to 1 wt% and then decreased at higher concentrations (Fig. 34C). This might be due to the rapid and high production of free radicals and the rapid reaction with monomers which competes with polymerisation.[273]
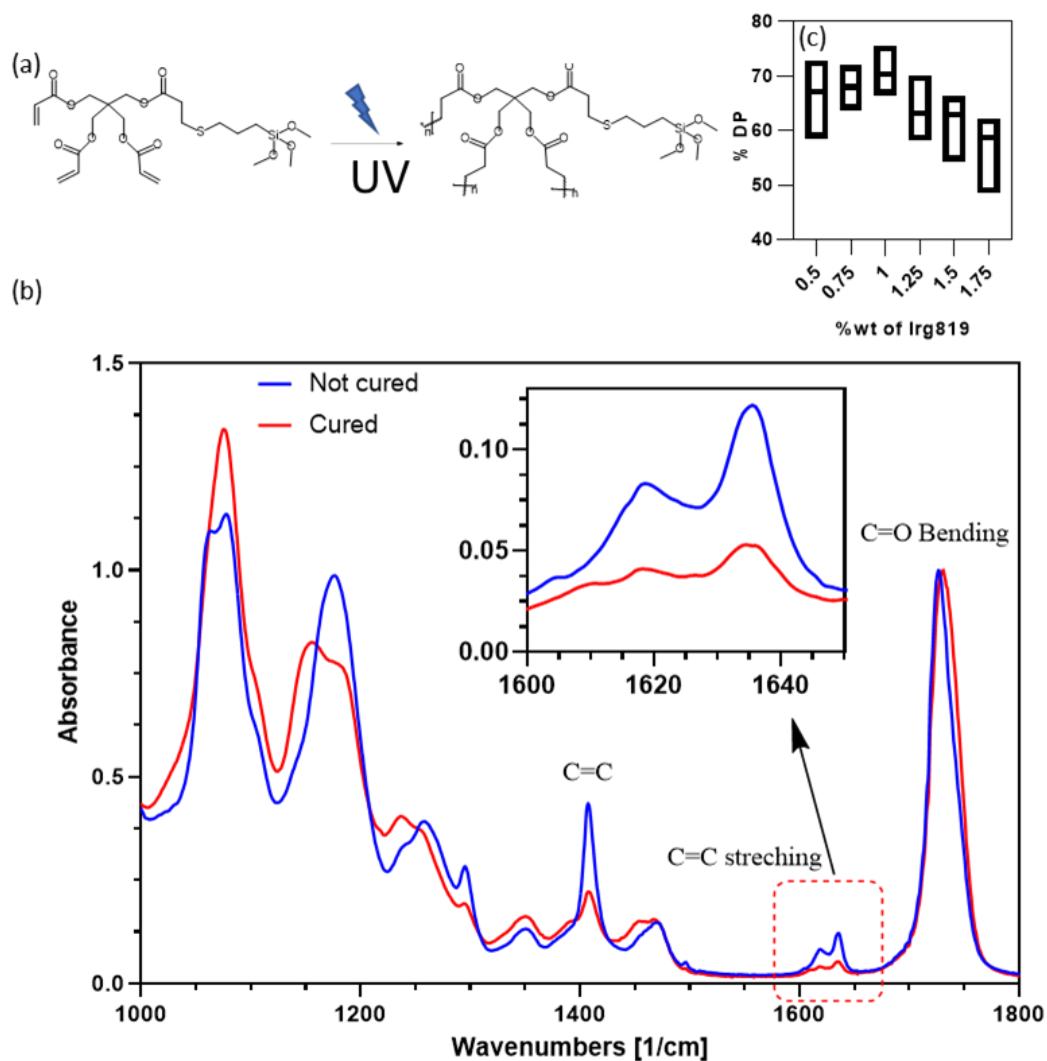
Fig. 34 Polymerisation of MP. The polymerisation reaction by exposing the UV light. FTIR spectra of MP before and after photopolymerisation (b). Degree of polymerisation in different concentrations of Irgacure 819 (c).

4.3.   3D printing of photocurable resin

After preparing the photocurable ink, the printing was tested with BMF microArch™ S130 micro-SLA. This printer uses DLP technology, which can make the parts with ultra-high resolution (down to two μm^2). The printer is built upon BMF's patented Projection Micro Stereolithography (PµSLA) technology, a technique that

allows for rapid photopolymerisation of an entire layer of liquid polymer using a flash of UV light at micro-scale resolution. A digital light projector screen, DMD, vat (resin tank), build plate, and build plate elevator are the fundamental elements of a DLP 3D printer (Fig. 35).

DLP: A DLP 3D printer's light source is a digital light projector.

DMD: The Digital Micromirror Device (DMD) is a part that is made from tens of thousands of micromirrors and is used to guide the light beam that the digital light projector projects.

VAT: The vat is a tank for the resin.

Membrane: To allow the resin to be cured by the light emitted by the digital light projector, the vat must have a clear top called a membrane.

Platform: The printed part attached to a stage during printing is called the build platform.

Stage-Z1 Lift: A self-explanatory component, the z-axis lowers the construction platform gradually when printing.
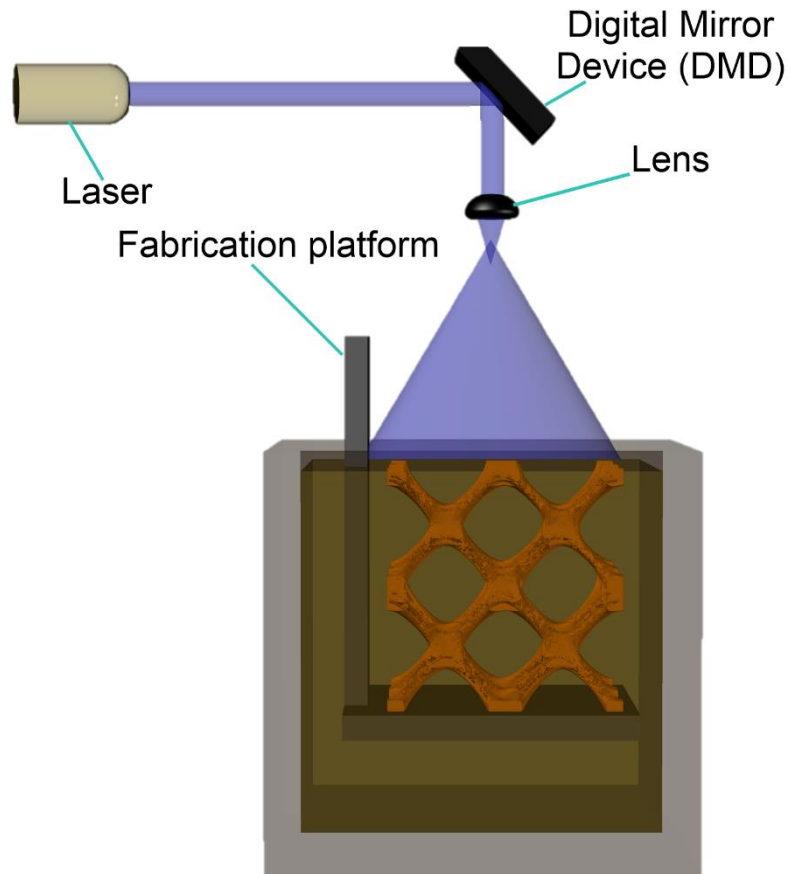
Fig. 35 Schematic structure of BMF PµSLA. As depicted in the figure, the resin vat holds the liquid photopolymer, the build platform supports the object being printed, the laser sources UV light for curing the resin, the lens focuses the laser, and the Digital Mirror Device (DMD) precisely controls light patterns for layer-by-layer resin curing.

The designed 3D model was first virtually sliced into 2D image layers by the BMF software slicer (Fig. 36A). The vat was then filled with resin. The construction platform was then lowered into the resin tank, and the resin was added next (Fig. 36B). When the build platform is almost level with the resin, there is little room between the build plate and the bottom of the vat. The space left between the build plate and the bottom of the vat determines a printed layer's height. The distance between the two was set

to 10 microns. The DMD uses projected light to create the layer's picture, which is subsequently directed to the clear vat top in the layer's pattern (Fig. 36A). The resin is cured into a solid, creating the first layer when the layer's image reaches the top of the vat. The construction platform descends several levels and then goes back up one layer below to make room in the vat for the next layer to be cured. Then, the digital light projector flashes a picture of the layer to the top of the vat once again, causing the next layer to solidify. Until the complete 3D component is done, that procedure is repeated.

Fig. 36C displays the printing settings used to print the sample. The quantity of photos scheduled for printing in each printing step is shown in the first column. The subsequent step in photocuring each layer is exposure time (Exp-t) light exposure. The Exp-t was set to be 2 seconds for all the layers except the first layer. The first layer exposure time was set 10 seconds to ensure the attachment of the first layer to the building platform. The moving distance (M-d) is the distance that stage moves down while wanting to replace the next printing resin. The M-d was set 1mm in this instance. This distance should be higher when the viscosity of the resin is higher. The delay time (De-t) refers to the time the stages stay down to replace the resin for the next layer. If the ink is more viscous, the De-t should be longer since viscous resin takes longer to flow and replace on the printing platform. The Moving upward (M-u) is the distance

the lift needs to come up for the next printing layer. For our instance, since the printing layer is 10 μm, the moving down 100 μm and then 90 μm upward.
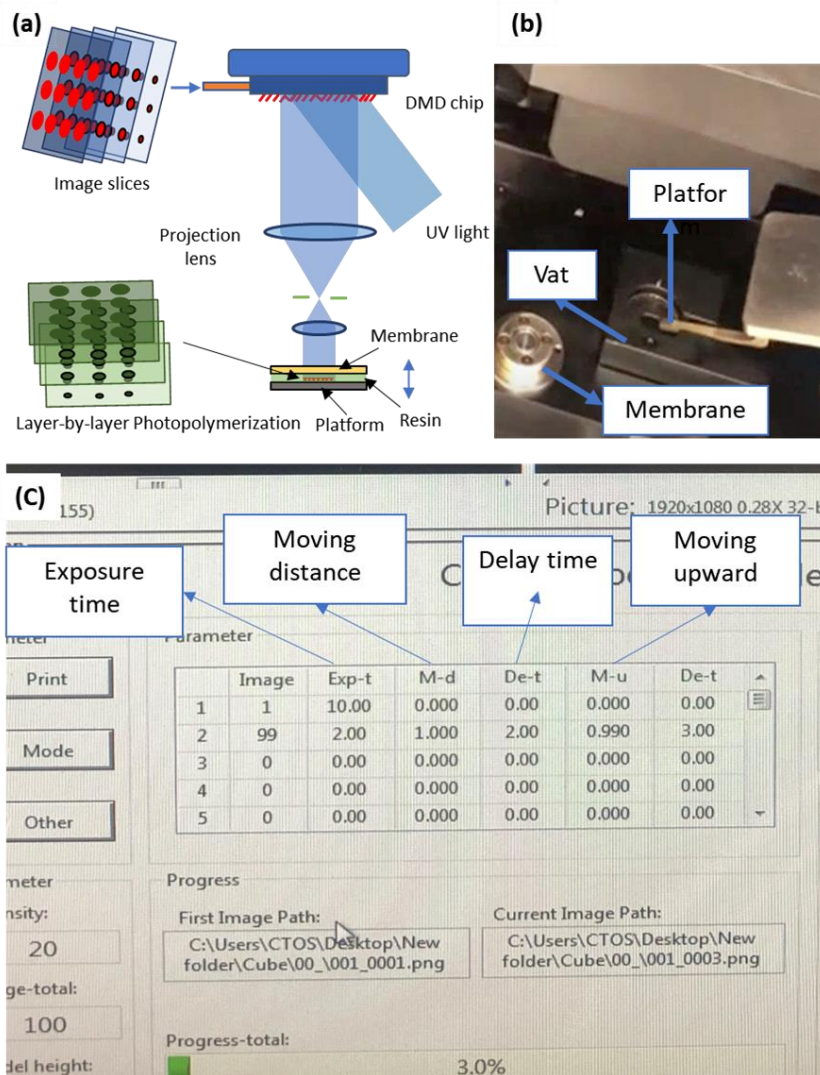
Fig. 36 3D printing of the resin using BMF S130. (a) Schematic presentation of the printing process. (b) Photo of setting up the vat, platform, and membrane. And (c) Software settings for printing parameters.

The Kolb et al.[235] method was used to evaluate the printing quality. Comparing the designed portion to the printed part is the foundation of this approach. In order

to create overhanging components with a high z-resolution, this approach examines the role of light absorbers in managing the curing depth of resin material. A unique model item called the "bridge-test part" was created with a high overhang to measure the dimensional correctness of the printed parts in the z-axis (Fig. 37 A). As shown in Fig. 37 B, the first attempts to print the MP resin in the form of a "bridge-test part" were unsuccessful. Each layer that was printed is much larger than the destined component. The printed portion, which is so large as seen in the inset, protrudes from the printing platform. This is due to two factors: First, light penetrates the resin more than desired depth,, and second, polymerisation continues even after light exposure and causing unwanted polymerisation. Adding a small amount of curcumin as a photo-absorber helped to address this over-polymerisation (OP). Curcumin prevents the OP by absorbing free radicals, halting the polymerisation immediately after light exposure, and controlling how much light can enter the transparent resin. As shown in Fig. 37 C, the printed component is similar to the planned part. Each layer was 10 µm thick, as specified in the printing settings (Fig. 37 D). The OP, determined using Equation 2, was as low as 7.60%, demonstrating excellent dimensional printing precision. The PµSLA can create high-quality prints with a nominal resolution of 2 µm in the XY direction and 5 µm in the Z direction. Using these capabilities, more complex geometries were tried to be printed. By comparing the interaxial angles of the designed and printed lattice structures, the angular precision of the printed sample was evaluated using a body-centre cubic (BCC) lattice structure (Fig. 37 E-H). The BCC lattice was selected as a model structure because it has all the required geometries,

including pores, tiny struts, and overhangs, to build complicated structures with a large surface area that may be used for biofuel cells and biosensors. The layer thickness of the printed lattice structure in Fig. 37E is 10 micrometres (Fig. 37F), and the angular accuracy of 82.5% shows the excellent resolution of the printed sample from all directions (Fig. 37F, 43G).
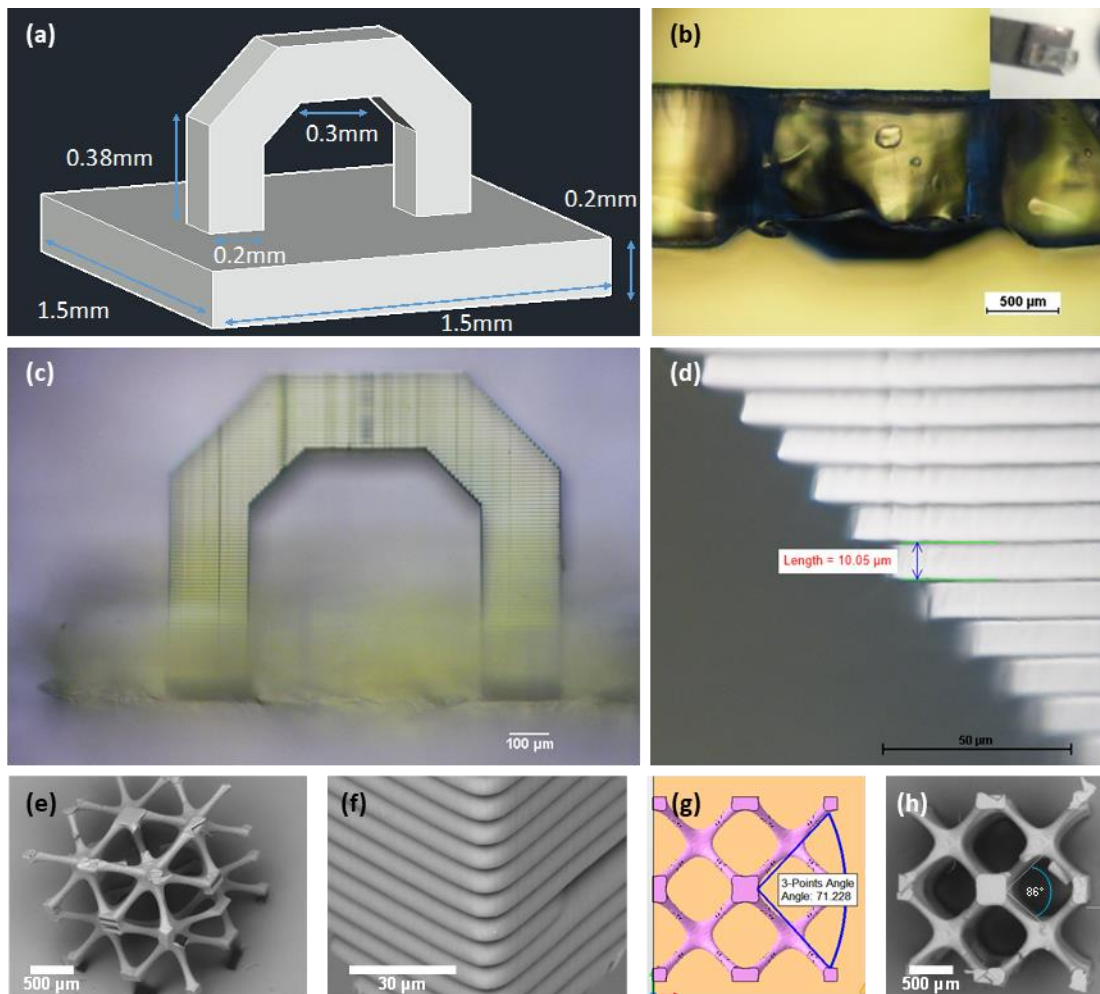
Fig. 37 Printing quality analysis. (A) Evaluating the Z-axis printing quality according to the Kolb et al. model. the high overhanging bridge test part was designed. (B) The printed resin without a photo-absorber. (C) The resin is printed with a photo-absorber. A magnified view of printed resin with a photo-absorber. (E) SEM image of 3D printed BCC lattice structure, (F) Magnified SEM image of 3D printed BCC

showing the thickness of a single printed layer, (G) Designed angle of the BCC model, and (H) Measured angle of the printed structure.

4.4.   Summary

The PμSLA is a promising approach to producing components in a quick, high-resolution, and broad printing scale window from two μm to 50 mm. If the monomer is created using Michael-thiol reactions, the surface of the printed component may contain functional groups. In this method, three of the PETTA's four arms are responsible for polymerisation, while one arm of the PETTA connects to the MPTMS' thiol group. The Michael thiol reaction was carried out in the PETTA and MPTMS to create the monomer, which was then validated by ^{13}CNMR and ^{1}HNMR studies. The photo initiator concentration was then researched to obtain the maximum degree of polymerisation. The highest degree of polymerisation is shown by the 1 weight per cent of the photo initiator. After selecting the appropriate printing settings, such as exposure duration, delay time, and printing thickness, the printing process was then set up. The use of the proper quantity of curcumin as a photoabsorber made high-quality printing feasible and revealed the low OP. More intricate shapes were produced successfully using this method. The angular precision study validated the high resolution of printing (87.5%) in the XY-axis. This improved printing method may open the door for using other DLP printers to produce large-scale parts with high amount of functional groups on the surface.

CHPTER 5

5. Surface functionalisation and electroless gold plating

5.1. Introduction

Coating a 3D printed part with metal using the electroless plating (EP) technique can be a possible solution as it can quickly deposit a wide variety of metals on 3D polymeric templates.[44,79,121,143] This method makes continuous and compact metal coating possible, which results in high conductivity.[146] The following procedures generally achieve the EP of a 3D-printed polymer: 1) surface preparation, 2) surface activation by seeding, 3) electroless plating and 4) sintering. Surface preparation and seeding are necessary for creating homogeneous and continuous metalisation.[116,119,121,274,275]

Different techniques have been developed to assure adhesion of the metal layer to the polymer surface. These include physical and chemical procedures such as etching, plasma, and UV treatment.[117–122] However, conventional surface preparation has two major difficulties that directly impact the quality of the deposited metal and its conductivity. First, if the adhesion of the physically adsorbed metallic coating is not strong enough, it will flake off once the plating procedure is complete.[121,147] Second, When utilizing UV and plasma for 3D surface treatment, coverage of very complex geometric structures is often limited by line-of-sight restrictions. As a result, the interior surfaces of three-dimensional objects remain untreated.[128,129]

In my PhD research, a thiol adhesion layer is introduced between deposited metal microstructures and 3D-printed polymer microstructures in order to improve adhesion.. The layer provides strong interaction between gold and polymer structure, resulting in improved adhesion and high conductivity. Our method of manufacturing 3D printed conductive microstructures includes the three main steps 1) 3D printing, 2) surface functionalisation, and 3) electroless gold plating of polymer microstructures. First, the photopolymerisation procedure using PµSLA was established by optimising the ink formulation and the printing process (as indicated in the previous chapter) (Fig. 38A). Second, the sol-gel reaction using 3-mercaptopropyltrimethoxysilane (MPTMS) was carried out to achieve multi-layers of thiol groups on the polymer surface (Fig. 38B). MPTMS was selected for the functionalisation reaction since it can be covalently bonded to the surface of the 3D-printed polymers via hydrolysis and condensation of silanol, and the thiol group on the other end of MPTMS can form a covalent bonding with gold atoms via gold-thiolate during electroless gold plating in the 3rd step. Finally, electroless gold plating (Fig. 38E) was carried out to deposit a thin coating of gold. Due to thiol functionality, this approach offers stronger metal adhesion to polymer structures than other methods.[122,276,277] Additionally, high conductivity is achieved without the need for sintering. This research can result in an improved electrode performance and aid in developing fuel cells and biosensors.
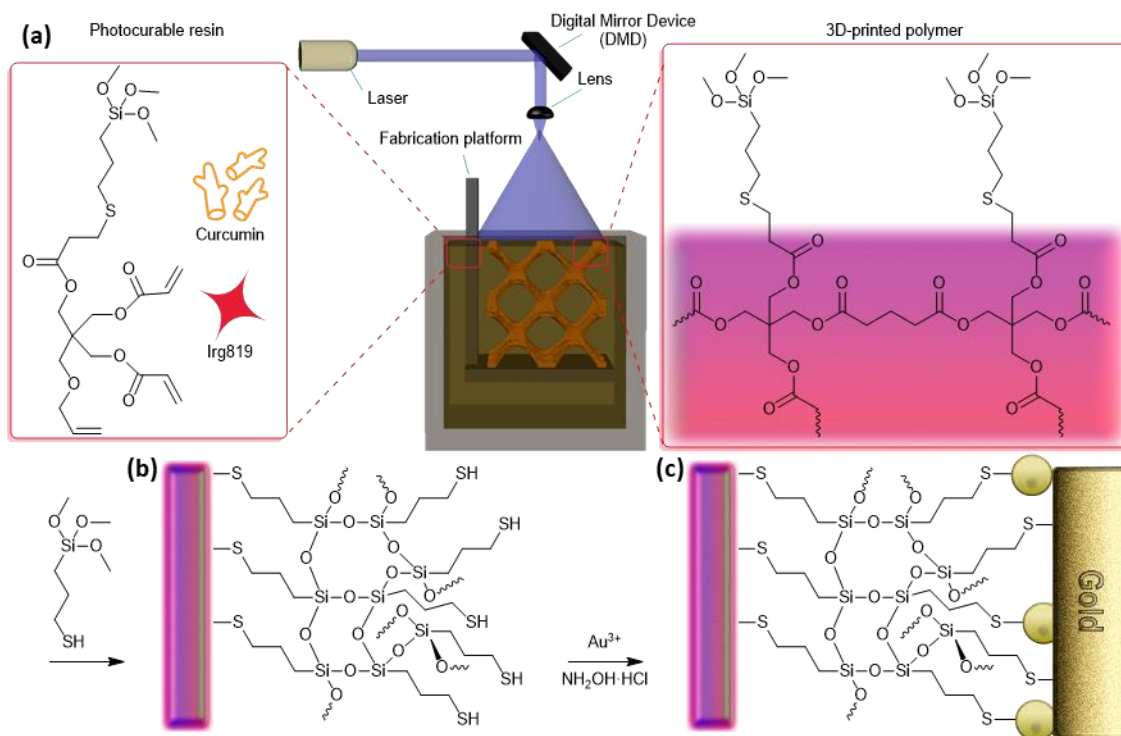
Fig. 38 Fabrication of robust 3D conductive microstructures: (A) 3D printing of functional photocurable resin using PμSLA, (B) Introduction of interfacial adhesion layer by surface functionalisation with MPTMS, (C) Electroless gold plating of a 3D printed polymer microstructure.

5.2.   Surface functionalisation using sol-gel reaction

Good adhesion between polymer structures and deposited metal is crucial for long-term and reliable device performance. To achieve this, thiol functionality was employed on the surface of the 3D-printed polymer via the sol-gel reaction using MPTMS (SG-MP), which leads to the formation of gold-thiolate bonding for better adhesion. Fig. 38B depicts the process in which hydrolysed silanol groups are assembled on the polymer surface and form a network following immersion in MPTMS sol-gel.[278] The use of sol-gel technology enables the creation of a 3D network appropriate for the various surface functionalisation. Sol-gel-derived inorganic

materials are especially desirable for biosensor manufacturing due to their ability to be created under ambient conditions and their adjustable porosity, excellent thermal stability, and chemical inertness. Additionally, unlike UV and plasma treatment, the sol-gel technique does not have grain size and pore diameter limitations for slurry infiltrations. Therefore, the 3D-printed complex structure's inner surface can be uniformly functionalised by the liquid sol-gel, as it can enter the printed pores.[279]

Using XPS and ToF-SIMS analysis on the materials before (MP) and after (SG-MP) the sol-gel process, the surface thiol functionality and concentration were investigated. For XPS and ToF-SIMS analysis, the surface sample has to be flat. Therefore, the sample needed to be printed as a cube. Since the sol-gel layer forms on a extreme surface, it is crucial to protect the functional group from any physical harm that may result from handling or mixing the sample and touching the vial wall. In order to protect the surface and make the top and bottom sides of the surface distinct, four pillars were added (Fig. 39A). These physical harms may be sufficiently powerful to destroy each coating. As shown in Fig. 39B, even after gold coating, the edge of the pillar's gold layer was damaged by contact with the vial wall during the reaction. However, the cube's core, which was used for surface characterisation analysis, was still intact. This demonstrates the effectiveness of the pillars in keeping the sample

surface   untouched   for   characterisation.
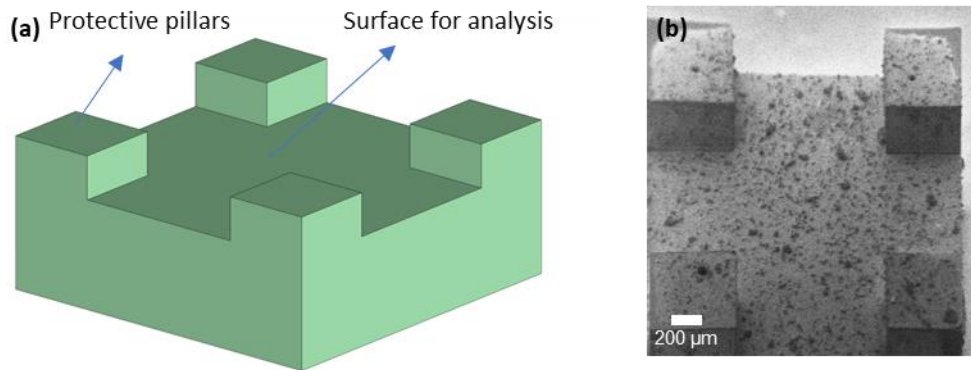
Fig. 39 The prepared sample for surface functionalisation analysis. (A) designed cube with four protective pillars. (B) The SEM image of 3D printed cube.

The X-ray photoelectron spectroscopy (XPS) was used to confirm surface functionalisation and find a link between sol-gel reaction time and gold coating quality. XPS analysis on the 3D printed polymer (MP polymer) revealed characteristic Si2p at 102 eV and O1s at 532 eV for alkoxysilane ($-Si-(OCH_3)_3$) groups and S2p at 163.8 eV for thioether (C-S) bond, confirming the successful implementation of alkoxysilane groups on the polymer surface (Fig. 40). These alkoxysilane groups take part in the sol-gel reaction with MPTMS in the next step to build the interfacial adhesion layer for gold deposition.
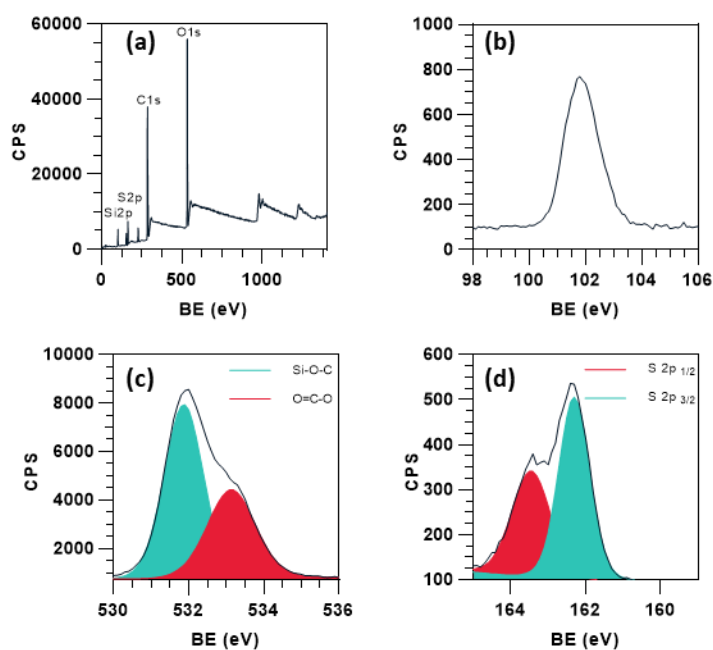
Fig. 40 XPS analysis on 3D printed MP polymer. (A) Survey scan spectrum. High-resolution spectra of (B) Si2p, (C) O1s, and (D) S2p.

An interfacial adhesion layer with thiol functionality was introduced by the sol-gel reaction of MPTMS with alkoxysilane groups on the surface of the 3D printed microstructure. The sol-gel reaction was carried out for differing reaction times (t_{func}) ranging from 1h to 3 days to find optimal functionalisation reaction time, and the amount of thiol groups was estimated using XPS analysis on the samples before and after the sol-gel reaction. The atomic percentages of S and Si relative to C of the surface functionalised polymer (SG-MP polymer) after the sol-gel reaction at t_{func} = 3d were increased by three times compared to those for the MP polymer (t_{func} = 0h), confirming the successful formation of the thiol adhesion layer consisting of MPTMS (Table 4).

Table 4 The XPS spectra of the 3D printed polymer before functionalisation showed the presence of the three main elements (C, O, S, and Si) in different atomic percentages (at%). After functionalisation, the spectra showed an increase in the at% of S, which corresponded to the increase in functionalisation reaction times.

Sample	Element (At%)			
	C 1s	O 1s	S 2p	Si 2p
MP	68.30	25.95	2.45	3.30
SG-MP functionalised for 1h	66.68	26.32	3.34	3.66
SG-MP functionalised for 2h	65.58	25.86	4.03	4.53
SG-MP functionalised for 3h	64.88	25.08	4.79	5.26
SG-MP functionalised for 4h	63.63	25.59	5.03	5.75
SG-MP functionalised for 1day	59.86	23.70	6.06	10.38
SG-MP functionalised for 2day	62.51	20.60	7.48	9.41
SG-MP functionalised for 3day	60.24	24.73	6.64	8.39

The high-resolution S2p core level spectrum for the SG-MP polymer shows the peak at 163.8 eV. assigned for free thiols, and no oxidised sulphur was found (Fig. 41A). The atomic percentage of S2p for free thiols increases with t_{func}, confirming the formation of thicker MPTMS adhesion layers at longer t_{func} (Fig. 41B). The high-resolution C1s spectrum of the SG-MP polymer also supports the formation of the thiol adhesion layer. The C1s peak in Fig. 41C was resolved by peak fitting into three chemical states: C-C at 285.0 eV, C-S/C-O at 287.0 eV and O-C=O at 289.0 eV. The peak at 289.0 eV is assigned to be O-C=O moieties of PETA from the MP polymer,[280] and reduction of this peak after sol-gel reaction indicates the introduction of thiol adhesion layer on the surface of the MP polymer (Fig. 41D).
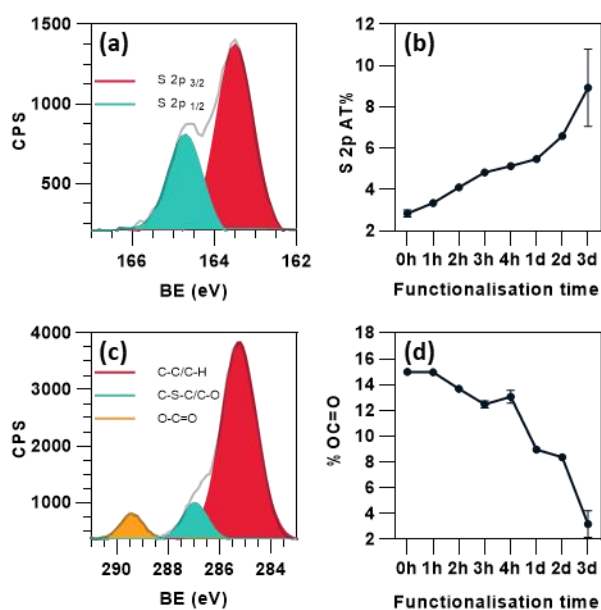
Fig. 41 XPS analysis on 3D printed polymer with thiol functionalisation (SG-MP polymer). (A) high resolution S2p core level of the SG-MP polymer prepared at t_{func} = 3h. (B) the atomic percentage of S2p of SG-MP polymer after thiol functionalisation at different t_{func}. (C) High resolution C1s core level of the SG-MP polymer prepared at t_{func} = 3h. (D) The proportion of O-C=O moity to other C1s chemical states of the SG-MP polymer at different t_{func}.

The successful introduction of the thiol adhesion layer was also supported by time-of-flight secondary ion mass spectrometry (ToF-SIMS) analysis. The SH- signal (at 32.98 u) for the SG-MP polymer was enhanced compared to the MP polymer shown in ToF-SIMS spectra data (Fig. 42A). The $C_3H_3O^-$ peak (at 55.02 u) corresponding to the methoxy group was significantly decreased after the sol-gel reaction, which might be attributed to the hydrolysis of the methoxy group during the reaction (Fig. 42A). Furthermore, the intensity of the SH$^-$ signal shown in ToF-SIMS mapping images

confirms that free thiols are distributed evenly throughout the surface (Fig. 42B and 48C).

Centre Mass (u)	Assignment
24.00	C2-
32.98	HS-
55.97	C_2S-
71.02	C_3H_3O_2-
59.97	SiO_2-
25.00	C_2H-
15.99	O-
31.97	S-
43.97	CS-
55.02	C_3H_3O
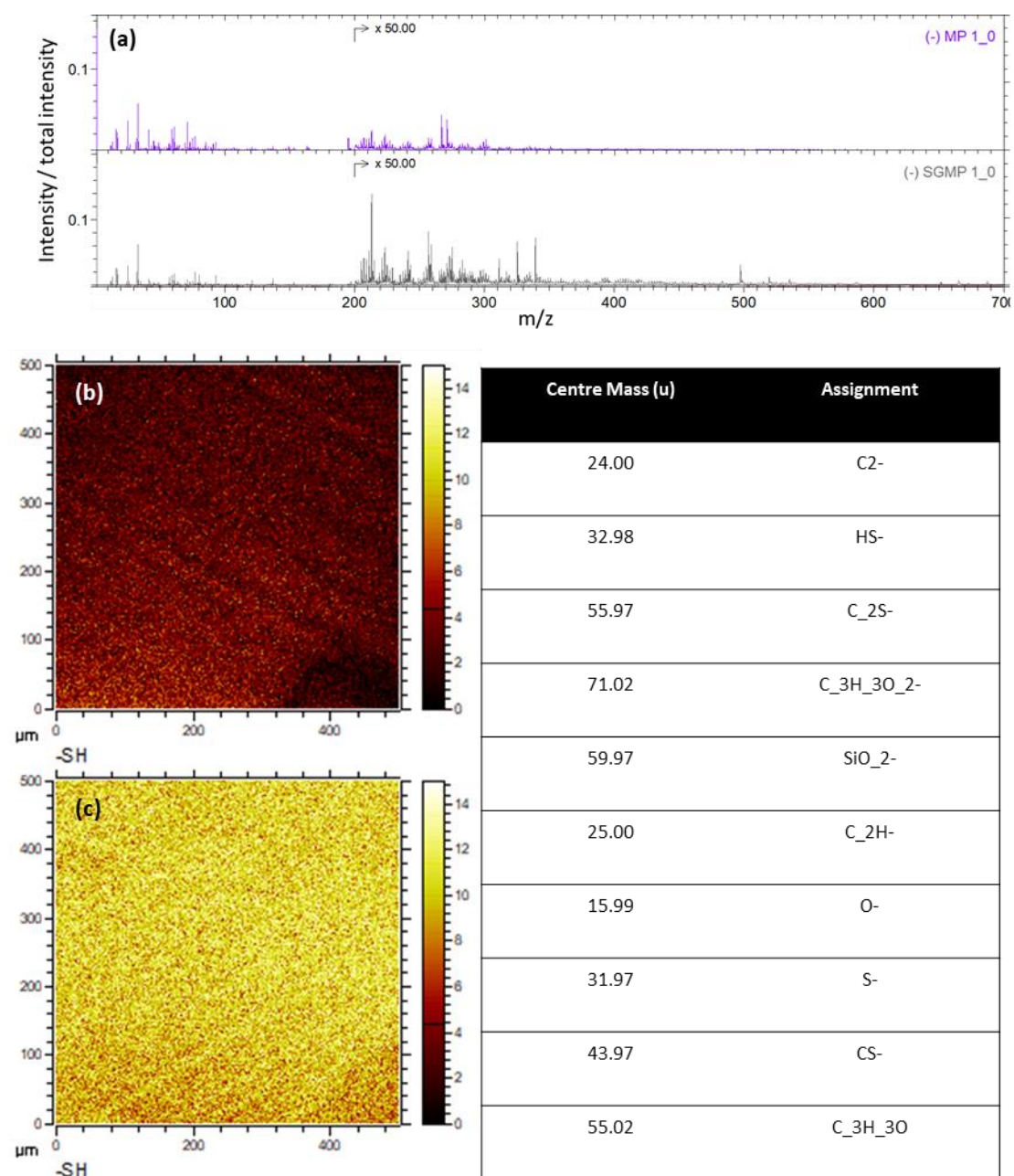
Fig. 42 Surface chemical composition analysis of 3D printed polymers before (MP polymer) and after surface functionalisation with MPTMS (SG-MP polymer). ToF-SIMS mapping data of (A) MP polymer and (B) SG-MP polymer. (C) ToF-SIMS spectra of MP polymer and SG-MP polymer. (D) Peak assignment in ToF-SIMS spectra.

5.3.   Electroless gold plating

The continuous gold layer was deposited on the 3D polymer microstructure (SG-MP polymer) by the following steps: i) seeding with gold nanoparticles (AuNPs) and ii) electroless gold plating by reduction of gold precursor to Au(0). The solution's colour gradually changed from yellow to colourless throughout this procedure. The polymer's colour changed simultaneously from clear to brown to gold (Fig. 43A-C). This is confirming the autocatalytic process (as described in Section 2.7.2) in which gold nanoparticles (seeds) catalyse the reduction of gold ions to gold metal, causing their growth. The AuNPs continue to grow until they unite to form a thin, conducting layer (Fig. 42D-G). AuNPs can be attached to the thiol-functionalised adhesion layer during the seeding step. The AuNPs-seeded polymer was then soaked in an electroless plating solution containing gold precursor ($HAuCl_4$) and a reducing agent (hydroxylamine) and sonicated for 7 min for continuous gold growth on the surface. These AuNPs on the surface act as a catalyst in the electroless plating reaction and help to reduce Au^{3+} to Au(0) by hydroxylamine preferentially on the AuNPs seeded sites. In addition, during the plating procedure, the thiol groups on the surface of the SG-MP polymer are deprotonated in the plating solution and interact strongly with Au^{3+}, resulting in a high concentration of Au^{3+} on the polymer surface for continuous gold growth and thus the formation of a uniform gold layer on the surface.[281–284]
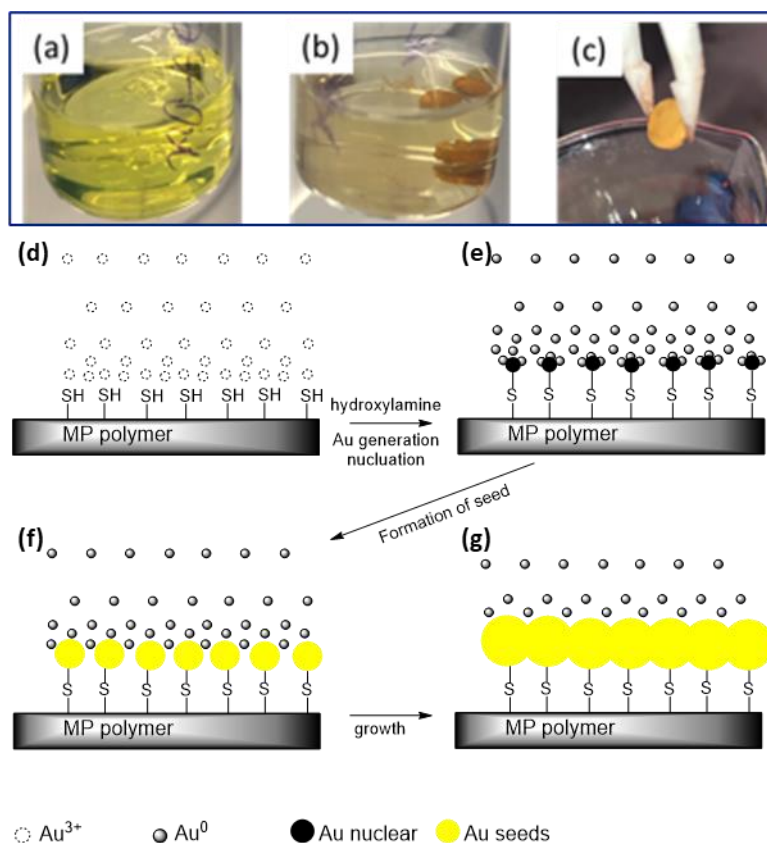
Fig. 43 Electroless plating process. (A) gold salt solution without sample. (B) Electroless plating solution after adding sample. (C) The gold coated sample after EP reaction. Schematic presentation of electroless plating process: (D) Functionalised sample in the EP solution, (E) seeding, (F) GNP growth, and (G) thin-film forming.

This surface functionalisation and EP procedure was used to coat complete lattice structures. As shown in the SEM image, the coating was damaged (Fig. 44A), particularly in the edge section. This was ascribed to the physical harm done when the sample was touched to the vial when it was being shaken through the EP plating. To safeguard the new lattices via sandwiching them between two flat platforms. As can be observed in Fig. 44B, the protective layer was effective in shielding the lattice while the coating held up well. It has been observed that the coating is not occurring completely uniformly and that the corners are not being coated, as shown in Fig. 44C.

Because it helps produce a more uniform gold coating (Fig. 44D) by reducing the creation of large gold agglomerations weakly bonded on the surface, sonication during electroless plating was used to solve this issue. Additionally, it aids in the removal of Cl_2 bubbles produced during the reaction that obstruct the electroless plating solution's ability to penetrate the lattice structure.
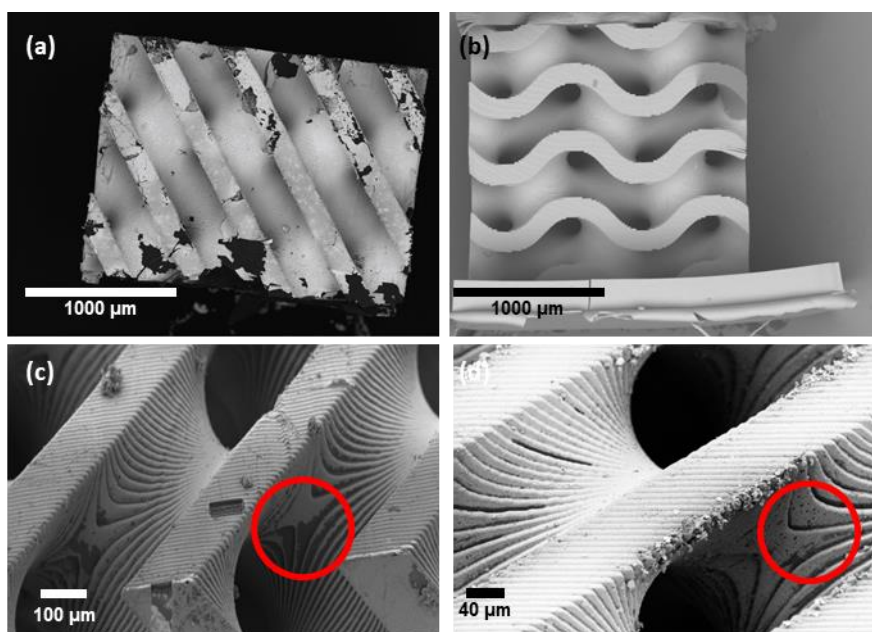
Fig. 44 SEM images showing the EP of diamond lattice structure. The electroless gold plated lattices with (A) and without (B) protective layer. The electroless gold plated lattice structure through the EP reaction with (C) and without (D) sonication.

It was noticed that this method only works well with the SG-MP polymer with a thiol interfacial adhesion layer. The MP polymer without thiol groups does not provide strong adhesion between created gold and the polymer surface. Hence, the weakly bound gold on the MP polymer was detached from the surface during sonication, leading to reduced gold left on the surface (Fig. 45). On the other hand, the thiol

interfacial adhesion layer on the SG-MP polymer provides strong binding sites for gold such that sonication only disturbs weakly bound gold and does not affect the deposited gold with strong adhesion.
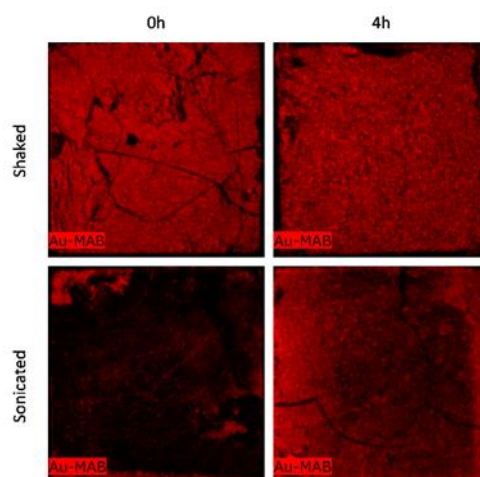
Fig. 45 Comparison of shaking and sonication of gold coated samples. On samples not functionalised with thiol, shaking through the electroless plating reaction, provided better gold coverage, whereas sonication failed to form gold attachment. As opposed to this, when a sample is functionalised with thiol, gold is also deposited when it is sonicated.

The 3D gold electrodes of three triply periodic minimal surface (TPMS) lattice structures were successfully fabricated: diamond, gyroid, and primitive (Fig. 46A-C). The electrodes with these lattice structures are particularly interesting for applications requiring large surface areas with ideal stiffness, such as biosensors and compact, lightweight fuel cells with high energy density.[41] The diamond (D) lattice structure, for instance, exhibits excellent mechanical properties and highest surface area among all the TPMS lattice structure.[41] The D-Lattice structure printed in this research with dimensions of 2x2x2 mm shown in figure Fig. 46A provides provides surface area of

64.6 mm^2 making it ideal geometry for EFCs and enzymatic biosensor applications. Gyroid (G) lattice structure (Fig. 46B) provides lower surface area (54.2 mm^2), but it is highly attractive for tissue engineering as it is found in various natural systems, including biological tissues and certain minerals.[285,286] Its biomimetic nature makes it an attractive choice for bio-inspired designs and applications, such as tissue engineering scaffolds or lightweight structural materials inspired by natural structures. Primitive lattice structure (Fig. 46C) in contrast provides least surface area (42.2 mm^2) but have the highest fluid permeability through the sub-volumes, which makes them suitable for applications as ultralight structural materials and tissue engineering scaffolds.[287]
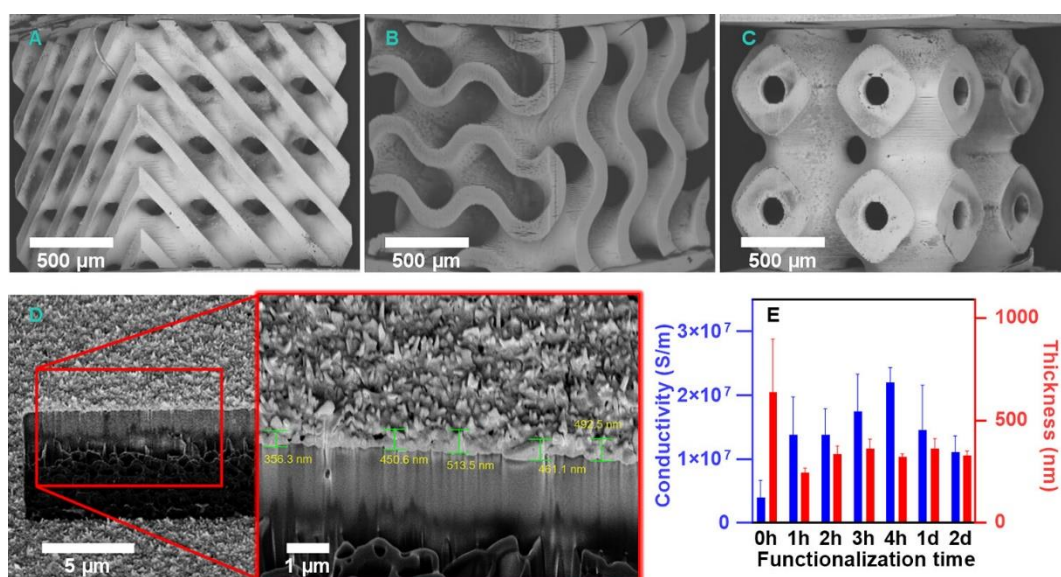
Fig. 46 SEM images of electroless gold plated 3D microstructures: (A) Diamond, (B) Gyroid, and (C) Primitive. (D) FIB-SEM analysis on the cross-section of the electroless plated sample prepared from the SG-MP polymer at t_{func} = 3h. Inset shows the magnified image showing the average thickness of 354±27 nm, (E) Effect of thiol functionalisation time on electrical conductivity of gold deposited samples.

* The reference sample (0h) was electroless plated using a gentler mixing method

since the gold did not adhere to the surface during sonication. The error bars show the standard error of the mean of at least three independent experiments.

The developed methodology ensures the uniform deposition of gold on both the lattice top surface and the inner surface of pores within the structure, as demonstrated by SEM and energy dispersive X-ray analysis (EDX) mapping data (Fig. 47A, 51B). The morphology and gold deposition were observed by Energy-Dispersive X-ray (EDX) spectroscopy. EDX map that collected on the scale of 3.5 mm × 2 mm of the coated polymer confirmed further details on the smooth, conformal Au coatings (Fig. 47C). The EDX spectrum in Fig. 47D exhibits an evident peak corresponding to the high amount of Au after electroless gold plating.
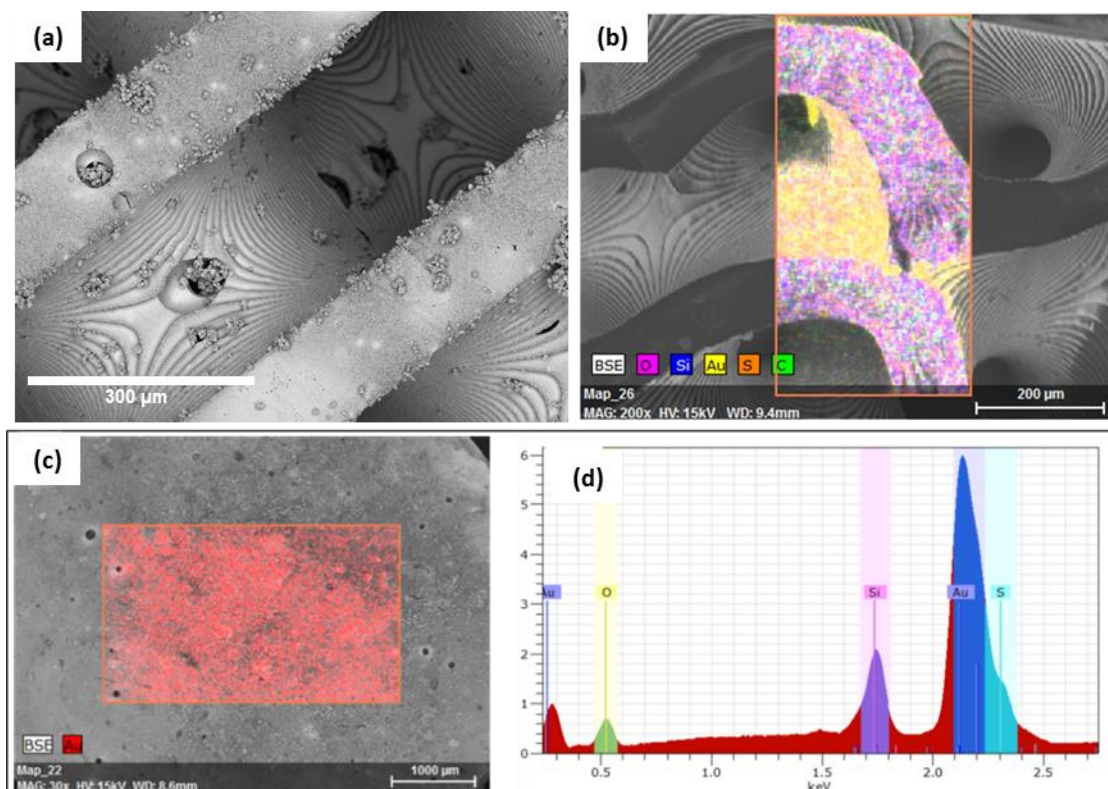
Fig. 47 Surface chemical composition of gold-coated SG-MP (t_{func}=3h) polymer using EDX. (A) SEM images of Diamond lattice structure showing the gold within the inner part of the 3D-structure. (B) EDX mapping data of the cross-section of gold-coated diamond lattice structure indicating the unform gold deposition inside the lattice structure. (C) SEM image showing EDX mapping signal of Au shown in red. (D) EDX spectrum proving the existence of Au, O, Si, and S.

5.4. Electrical conductivity

The sheet resistance (R_s) and electrical conductivity (σ) of the deposited gold on the 3D printed polymer structure (2 mm x 2 mm x 0.5 mm) were measured using Van der Pauw method and calculated from Equation 6 and Equation 7, respectively.[288] The average thickness of the deposited gold layer was evaluated to be 330 ± 60 nm using focused ion beam scanning electron microscopy (FIB-SEM) (Fig. 46D). I note that the conductivity of the electroless gold plated sample was improved by the introduction of thiol interfacial adhesion layer and increasing t_{func}. Since electroless plating on the

MP polymer in a sonication mode does not create gold on the surface, the reference sample (t_{func} = 0 h) electroless plated in a soft agitation mode for the conductivity measurement. The conductivity ($\sigma = 1.4\times10^7$ S/m) of the sample with thiol interfacial adhesion layer (t_{func} = 1 h) was one order magnitude higher than that ($\sigma = 4\times10^6$ S/m) of the sample without an adhesion layer (t_{func} = 0 h) (Fig. 46E). The highest conductivity ($\sigma = 2.2\times10^7$ S/m, 53% of bulk gold conductivity) of the deposited gold layer was achieved from the sample prepared at t_{func} = 4 h. The conductivities of the samples prepared at t_{func} = 1 d and t_{func} = 2d were slightly lower compared to the sample at t_{func} = 4 h. This might be due to non-uniform, thick layer of MPTMS polymer formed at longer t_{func} during surface functionalisation,[289] leading to the formation of rough gold layer with uneven thickness (Fig. 48).
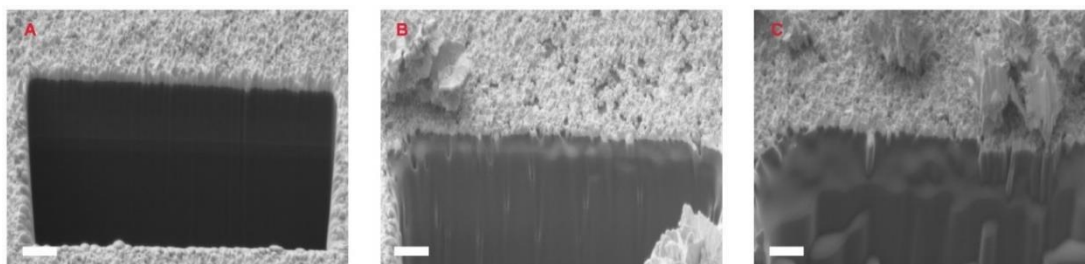
Fig. 48 Thickness measurement of the deposited gold on 3D printed microstructures using FIB-SEM. Cross-section images of the electroless gold plated samples prepared from the SG-MP polymers with (A) 4 hours, (B) 1 day and (C) 2 days functionalisation time. The scale bar is 1 μm.

5.5.   Interfacial adhesion

The mechanical adhesion between the deposited gold and the polymer scaffold was measured by applying a high-performance clear 3M scotch tape on the electroless gold plated sample and then peeling it off from the sample at an angle of 90 degrees.

The sample before and after adhesion test was analysed using SEM coupled with EDX. The adhesion of the deposited gold was quantified by estimating the area of gold from EDX mapping images before and after the adhesion test (Equation 4). Each sample was tested at least five times to ensure reproducibility and consistency. Without the introduction of the interfacial thiol adhesion layer, only 15 ± 2% of deposited gold remained on the polymer surface after the tape test, indicating poor adhesion (Fig. 49A). However, interfacial adhesion of the deposited gold layer was significantly increased by introducing the thiol adhesion layer shown in Fig. 49B. The maximum interfacial adhesion (97% of gold survived from adhesion test) was achieved from electroless gold plating of SG-MP polymer at t_{func} = 4h. I attribute the enhanced adhesion to the strong bonding between thiols and gold at the interface between the deposited gold and the polymer surface. The decrease in the amount of deposited gold and adhesion for the sample at t_{func} = 1d and 2d was observed. This might be due to the delamination of physically adsorbed MPTMS from the surface of SG-MP polymer during electroless plating in a sonication mode and adhesion test. A similar phenomenon was observed from the adhesion failure of electroless nickel-phosphorous film on the surface of silicon wafer where weakly bound multilayer grafting of alkoxysilane was formed on the silicon wafer.[289]

3 D - p r i n t i n g   o f   e n z y m a t i c
b i o f u e l   c e l l s
143 | P a g e
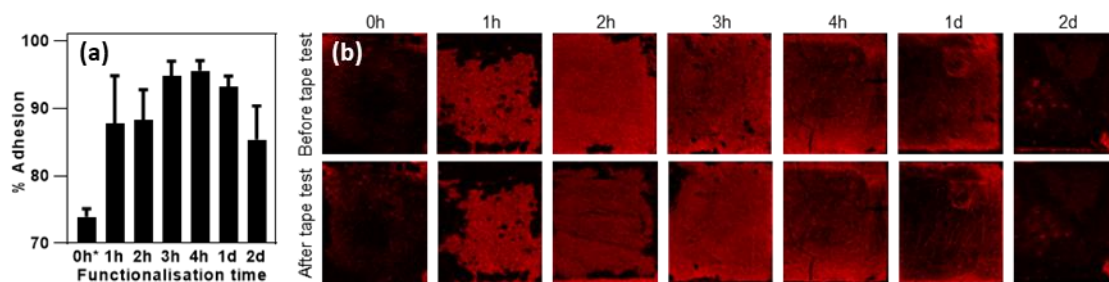
Fig. 49 Effect of thiol functionalisation on interfacial adhesion between the deposited gold and the polymer surface: (A) The percentage of gold remained on the polymer surface after adhesion tape test. (B) EDX Au mapping data before and after adhesion tape test.

5.6. Interfacial analysis

To investigate the interfacial bonding between the gold and the polymer surface, the surface and interfacial composition of a gold coated 3D microstructure were examined. XPS and EDX analyses were performed on the SG-MP polymers (t_{func} = 4h) before and after electroless gold plating. For the SG-MP polymer without gold coating, the S2p$_{3/2}$ peak appears at 163.8 eV, indicating the existence of the free thiols on the polymer surface (Fig. 50A). To confirm the gold-thiolate bonding using XPS, the sample was prepared with a thin gold layer by reducing the electroless plating time from 7 min for thick gold coating (330 ± 60 nm) to 3 min. The S2p core level of the SG-MP polymer coated with a thin gold layer exhibits the shift of the S2p$_{3/2}$ peak to 163.2 eV, indicating the gold-thiolate bonding (Fig. 50B).[290] The Au4f$_{7/2}$ peak of the thin gold-coated sample appeared at 83.6 eV for Au(0), with a shoulder at 84.2 eV. The shoulder peak at 84.2 eV might be attributed to the discontinuous gold islands formation on the polymer surface and charged when the photo-hole is not promptly neutralised

(Fig. 50C).[291] This peak disappears for the thick gold coated sample shown in Fig. 50D, indicating the successful formation of the dense and continuous gold film.
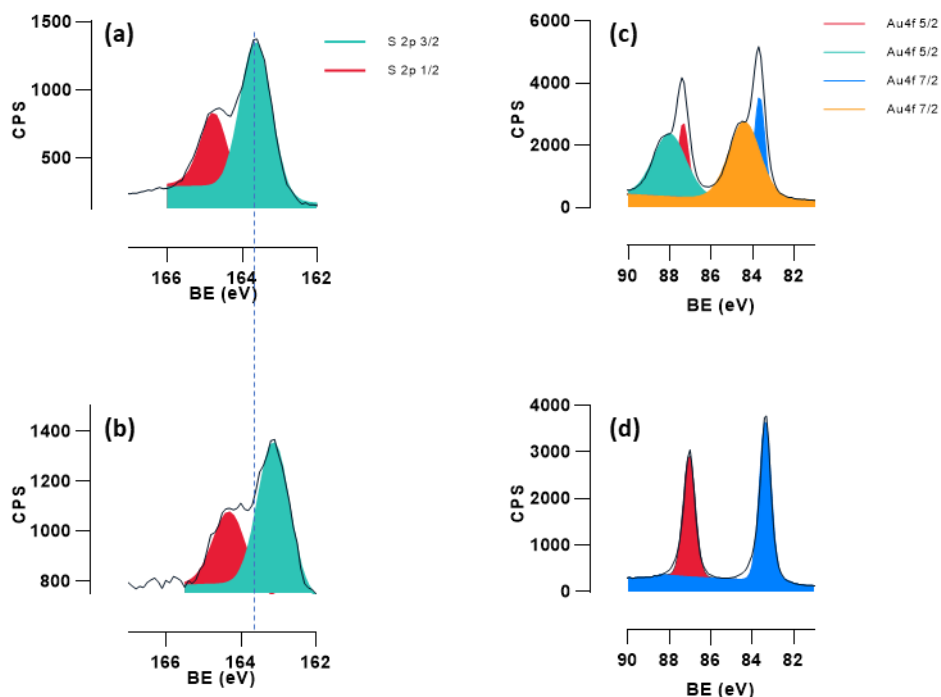
Fig. 50 XPS analysis on electroless gold plated polymers with different gold layer thicknesses. (A) and (B) demonstrate the S2p core level of the SG-MP polymer before and after depositing a thin layer of gold, respectively. The shift in S2P core level confirms covalent S-Au attachment. C and D show the Au4F core level spectra of the SG-MP polymer with a thin and thick gold layer, respectively. This shows that the gold layer on the surface after complete electroless plating is uniform.

ToF-SIMS depth profiling in combination with FIB-SEM was used to investigate the interfacial chemical composition and estimate the thickness and homogeneity of the interfacial adhesion layer of the gold-coated sample. The normalised ToF-SIMS depth profiles of the gold coated sample (t_{func} = 4h) in Fig. 51 show the interfacial adhesion layer consisting of gold-thiolate bonding characterised by Au_3S^- and $AuCS^-$

and MPTMS evidenced by the signals of SiO^{2-} and CSC^{-} with an estimated thickness of 50 nm between the deposited gold layer (Au^{-} rich area) and the polymer surface ($C_3H_3O_2^{-}$ abundant region). XZ cross-section mapping images reconstructed from the depth profile data in Fig. 51B-5F reveals the formation of a homogeneous interfacial adhesion layer across the sample.

The successful introduction of the interfacial adhesion layer and strong gold-thiolate interfacial bonding formation during electroless plating ensure the uniform and compact deposition of the gold layer on the polymer surface, leading to high electrical conductivity and strong adhesion. This methodology will allow simple fabrication of 3D conductive microarchitectures with various design form factors and surface area and provide the device reliability and performance because of strong adhesion, offering potential for novel electronics, including sensors and energy devices.
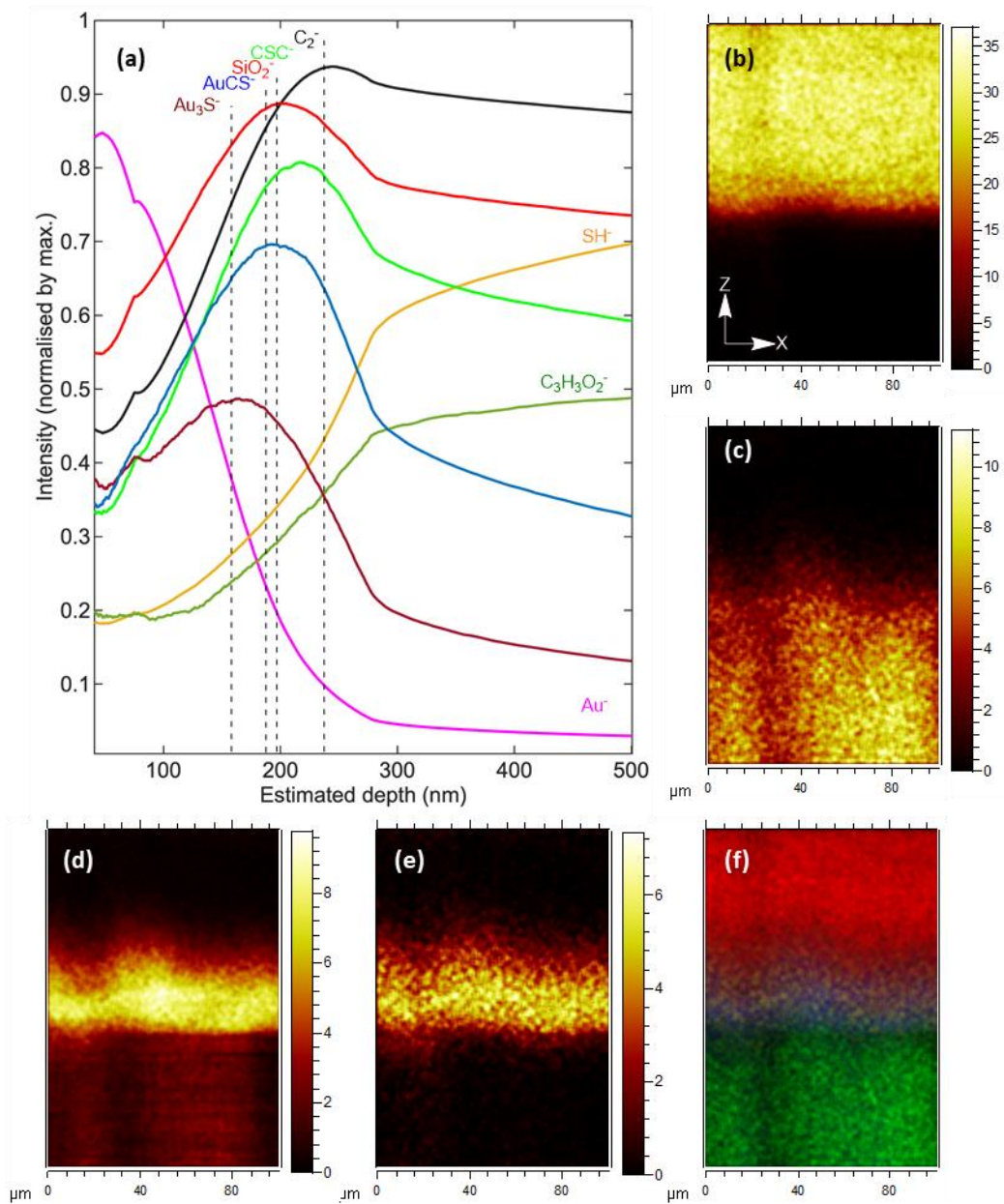
Fig. 51 Interfacial chemical composition analysis on gold deposited sample (t_{func} = 4h) using ToF-SIMS analysis. (A) ToF-SIMS depth profiles of the sample. Cross-section maps along XZ direction of (B) Au^{3-}, (C) CHO, (D) SiO_2, (E) AuS, and (F) overlay of the signals for (B), (c), (D), and (E). (Red: Au^{3-}, Yellow: AuS, Blue: SiO_2, Green: CHO).

5.7. Summary

This work demonstrated a method to fabricate robust 3D conductive microstructures using PµSLA coupled with electroless plating. The poor adhesion between a metal and a polymer, one of the main issues with electroless plating, was solved by introducing a thiol interfacial adhesion layer on the 3D printed polymer surface. The thiol groups on the polymer surface provide strong bonding with gold during electroless plating, confirmed by surface and interfacial analysis by XPS, EDX and ToF-SIMS, leading to uniform gold layer formation and thus high electrical conductivity. An adhesion test conducted on the 3D conductive gold samples demonstrated that nearly all deposited gold remained intact after the adhesion test. In addition, the samples were highly conductive (2.7×10^7 S/m), demonstrating significantly improved interfacial adhesion. This method enables interface engineering between the polymer and the deposited gold layer to achieve good adhesion. It provides a solution to overcome the limitation of the existing production method for the fabrication of complex and sophisticated microelectrodes with strong interfacial adhesion for biosensors and bioelectronics applications.

CHAPTER 6

6. Enzyme immobilisation

6.1. Introduction

The need for biocatalysts for industrial usage is growing daily in the twenty-first century since enzymes provide gentle, effective, and affordable reactions. However, several distinctive characteristics of the enzymatic proteins, such as their non-reusability, high susceptibility to various denaturing agents, and their loss of stability, is a barrier to the efficient usage of enzymes. Fortunately, immobilised enzyme can remedy these flaws by increasing the product's durability, reliability, reusability, and specificity. It has been demonstrated that immobilizing the enzyme on rigid structures, inducing rigidity in the enzyme, and improving its stability. The stability of enzyme is one of the main factors must be improved for practical application of EFC in the biomedical applications. This stability is required as it directly impacts on the EFC lifetime and efficiency. The stability in the EFC is dependent to two main factors of enzyme initial stability, and enzyme immobilisation method. The aim of this research in this section is to investigate these two factors in order to achieve the highest enzyme stability on the gold electrode printed in 3D.

6.2. Characteristics of glucose oxidase (GOx)

The most common enzyme in enzymatic biofuel cells and sensors is GOx from Aspergillus niger because of its high selectivity for glucose, stability across a wide range of temperatures, and stability in pH, including physiological pH.[292] The GOx, a dimeric, glycosylated flavoprotein, catalyses the conversion of glucose to

gluconolactone and, as a byproduct, produces hydrogen peroxide.[234] Each monomer has a flavin adenine dinucleotide cofactor (FAD/FADH$_2$) in the core of its highly covered active site. The free GOx uses molecular oxygen as an electron acceptor while also producing hydrogen peroxide to catalyse the oxidation of D-glucose to gluconic acid.[293] In the case of the EFCs, the electron that was cleaved off the substrate is sent to the electrode to produce current (Fig. 3 and Fig. 52). The effectiveness of such devices is strongly influenced by the inherent enzyme immobilisation, which has a direct impact on the rate at which electrons are transferred from the FAD/FADH$_2$ redox centre to the electrode surface, and a lifetime of the EFCs.
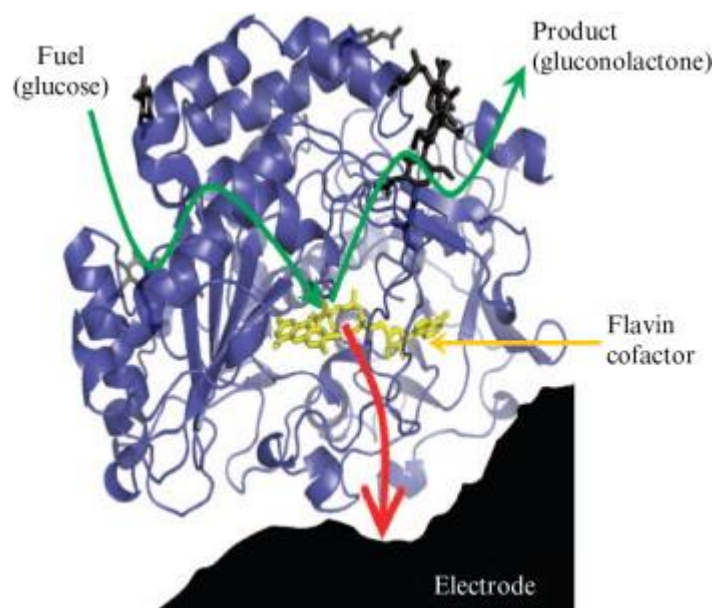
Fig. 52 Schematic representation Glucose oxidase that catalyses the oxidation of glucose, and releases electrons.[294] The electron then transfer from enzyme cofactor to the electrode.

To immobilise enzymes in an optimal manner, it is essential to investigate their surface charges, functional groups, and geometrical properties before employing

them in EFCs. The factors that may affect enzyme stability can be broken down as follows:

- **<u>Temperature:</u>** Most enzymes can be used, handled and stored under low-temperature conditions (0°C-4°C). However, some enzymes are unstable at room temperature and should be stored frozen in liquid nitrogen or -80°C.

- **<u>Enzyme concentration:</u>** Although the stability of the enzyme varies depending on the nature and purity, in general, the enzyme protein is stable at a high concentration, and at a low concentration, it is easy to dissociate and adsorb and even prone to surface degeneration.

- **<u>pH and buffer:</u>** Most enzymes are only stable over a specific pH range, and stability is reduced beyond this range. The type of buffer sometimes affects the stability of the enzyme.

To study as-mentioned factors in GOx, the free enzyme was first evaluated to find its stability in different environments. First, the enzyme was tested in PBS at room temperature. As shown in Fig. 53A, the free enzyme in a 3μg/ml concentration is inactivating at room temperature. The enzyme remained stable within the first two hours, and no decrease was observed. The enzyme was quite stable, and it only lost about 30% of its initial activity even after three days. Therefore, it was justified that the enzyme would preserve its initial activity during the immobilisation, which usually takes less than one hour. The enzyme stability was then tested to see if there was any connection between the enzyme concentration and stability. Since the enzyme is

stable, inactivating it and determining its stability takes a long time. The enzyme was inactivated at a higher temperature (50 °C) to acquire the data quickly. Fig. 53B shows no significant difference in the enzyme stability formed even after increasing the enzyme concentration 15 times. The GOx was tested in different buffers to see if it impacts its stability. After 150 minutes, the GOx in the different buffers reached half-life, and no significant difference was observed (Fig. 53C). It is evident that GOx from *A. niger* has a broader pH range, as the pH and buffer type do not impact significantly in the stability. Therefore, GOx immobilisation conditions could be tested in various pH and buffers.
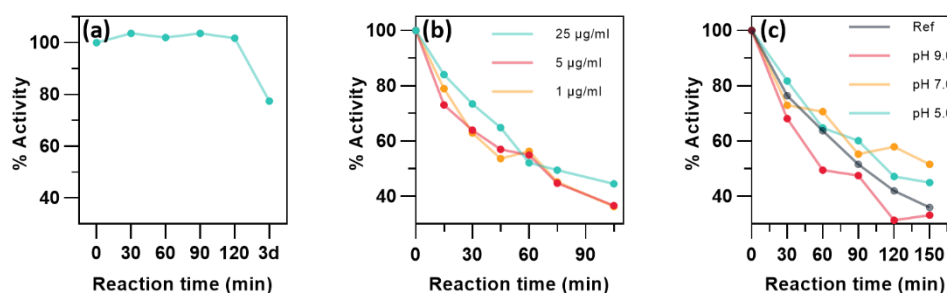
Fig. 53 Free enzyme stability test. (A) Free enzyme stability at room temperature. (B) Free enzyme (dissolved in the water) stability in different concentrations at 50°C. (C) Stability of free enzyme in three different buffers of carbonate, phosphate, and acetate at 50°C.

6.3.   GOx immobilisation

The demand for biocatalysts for biomedical use is increasing daily, as enzymes provide mild, efficient, and low-cost reactions. Nonetheless, the effective use of enzymes should be hampered by some peculiar properties of the enzymatic proteins,

3 D - p r i n t i n g   o f   e n z y m a t i c
b i o f u e l   c e l l s
152 | P a g e

such as their high sensitivity to several denaturising agents and their loss of stability during time. These defects can be removed by using the enzymes in their immobilised form. It improves firmness, safety, reusability, and target action, which are advantageous for EFCs. As indicated in section 2.8.3, enzyme immobilisation with covalent bonding is the most reliable technique to attach the enzyme for the EFC application. Immobilising an enzyme via multipoint covalent attachment, in a specified form, on pre-existing supports is one of the promising ways to make it stiffer. This technique for stabilizing enzymes is based on the need that the relative positions of all groups involved in immobilisation remain constant under all experimental circumstances, with the only movement allowed being that determined by the spacer arm's length (Fig. 54).[207]

Multipoint covalent immobilization: the relative positions of all groups involved in the immobilization must remain uncharged under any conformational change
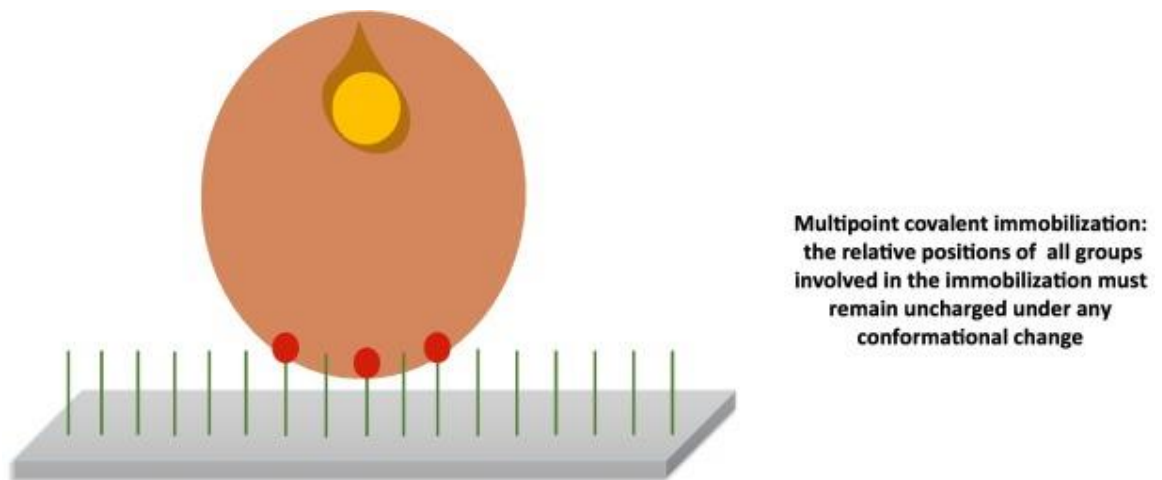
Fig. 54 The schematic presentation of enzyme immobilisation by multipoint covalent binding.[207]

Numerous GOx immobilisation protocols have been identified. However, it is unknown which is the most effective for immobilizing the enzyme on a gold electrode.

This is because each support has distinct physical and chemical surface features that may either increase or decrease the immobilised enzyme's stability. As a solution, testing the immobilisation of enzymes in inert support, where the only existing physical or chemical groups are those introduced by the researcher, was proposed.[295] An optimum immobilisation strategy can then be extrapolated to other supports after analysing the effects of immobilisation on the inert support. One particularly effective support in this respect is agarose beads, which are suitable for this use.[207] Therefore, to determine which approach can immobilise the enzyme with the highest degree of stability, I functionalised the agarose beads with several functional groups and tested the enzyme immobilisation. GOx was then immobilised on the 3D-printed gold electrode using the optimal immobilisation technique.

To find out which immobilised enzyme is more stable throughout the inactivation process, I evaluated the following hypotheses for GOx immobilisation:

- **GOx can immobilise on an aldehyde-activated surface:** Various enzymes have been stabilised by multipoint covalent attachment using aldehyde-activated surfaces such as glyoxal agarose.[296–299]

- **Crosslinking with glutaraldehyde enhances the stability:** Enzymes adsorbed on aminated supports may be crosslinked with the support,[300,301] or pre-activated using glutaraldehyde chemistry.[302,303]

- **Immobilisation pH can impact enzyme stability:** The immobilisation reaction pH can affect the enzyme orientation and stability, as indicated in section 0.

- **Cysteine and/or Cysteamine activated surface can be used for GOx immobilisation:** Cysteine and cysteamine are attractive compounds for functionalising the gold surface with amine for GOx attachment.[176,304–306]

6.3.1. GOx immobilisation on Glyoxyl functionalised surface

To test this hypothesis, glyoxal agarose was prepared according to the Guisán method.[299] The support was prepared by etherifying the primary hydroxyl groups of the support with Epichlorohydrin to introduce diols, which are later oxidised with sodium periodate to get the glyoxal group (Fig. 55A and B).[295] Theoretically, the surface of the GOx contains Lysine molecules, providing a free amine group on the surface that can attach to the short aldehyde group on the glyoxal -agarose and for the very strong multipoint covalent bond.
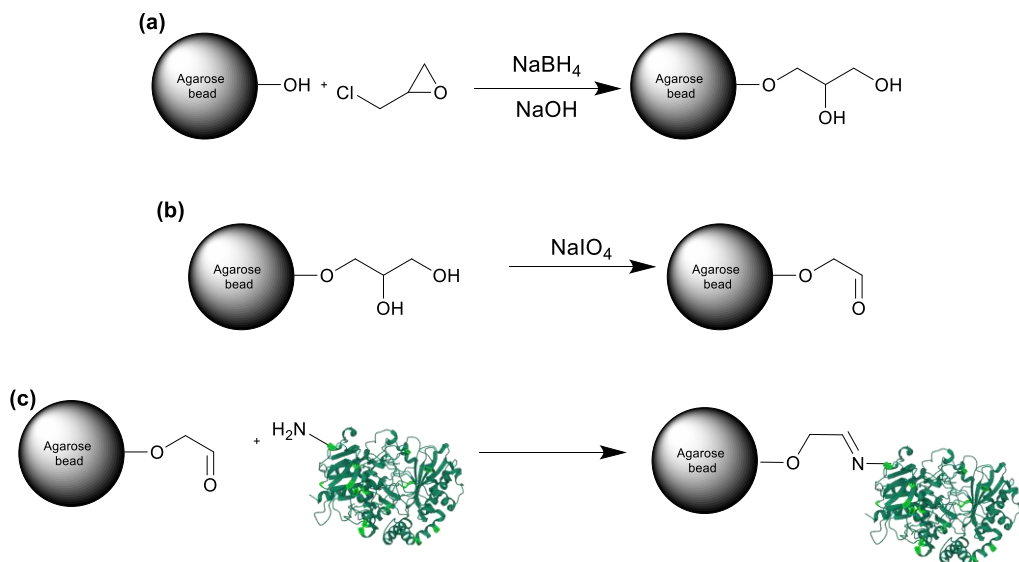
Fig. 55 The preparation and use of glyoxal agarose and enzyme immobilisation. (A) The etherification and reduction of Epichlorohydrin generate a diol group on the

agarose surface. (B) The diol's oxidation process produces glyoxal-agarose. (C) The aldehyde group on glyoxal agarose may connect to the amine group on the Lysine enzyme.

The enzyme should be immobilised on glyoxal-agarose under alkaline conditions, as described by Mateo et al.[307]. Consequently, this enzyme immobilisation procedure was conducted at room temperature, pH 10 (5 mM), and with roller shaking. As seen in Fig. 56A, although the activity of the reference GOx remained constant, the activity of both the suspension and supernatant diminished progressively. The activity of the supernatant decreases faster than that of the suspension, suggesting that certain enzymes are immobilised on the support. However, the rate of immobilisation on glyoxal-agarose was relatively slow, and the immobilised enzyme is not very stable since its activity decreased by more than 20% over the course of four hours. Only 24% of the enzyme was immobilised during four

hours on the glyoxal-agarose, showing that the immobilisation rate was not effective (Fig. 56B).

Fig. 56 Immobilisation of the GOx enzyme on glyoxal-agarose. (A) enzyme activity of suspension and supernatant during GOx immobilisation reactions. (B) Average GOx immobilisation rate.

This poor GOx immobilisation on glyoxal may be attributed to three main factors. First, it may be related to the low ion exchange between the enzyme and the support. As a result of ion exchange interactions, the enzyme adsorbs on the base surface, facilitating the formation of a dense and stable crosslink network between the enzyme and the support material.[308] Second, the final enzyme stabilisation obtained by the short spacer arm may also potentially be the source of reducing the enzyme activity as the reduction of the enzyme mobility will be more severe. And finally, the shorter spacer arm results in a lower number of covalent bonds (Fig. 57). A shorter spacer arm restricts the distance between the enzyme and the support surface. This limited accessibility can reduce the number of available binding sites on the support for the attachment of the enzyme. Consequently, fewer covalent bonds

can be formed between the enzyme and the support, resulting in a lower number of bonds overall.[207]

Very short spacer arm
Low number of enzyme - support bonds
High enzyme rigidification by each enzyme-support bond

Long spacer arm
Higher number of enzyme - support bonds
Lower enzyme rigidification by each enzyme-support bond
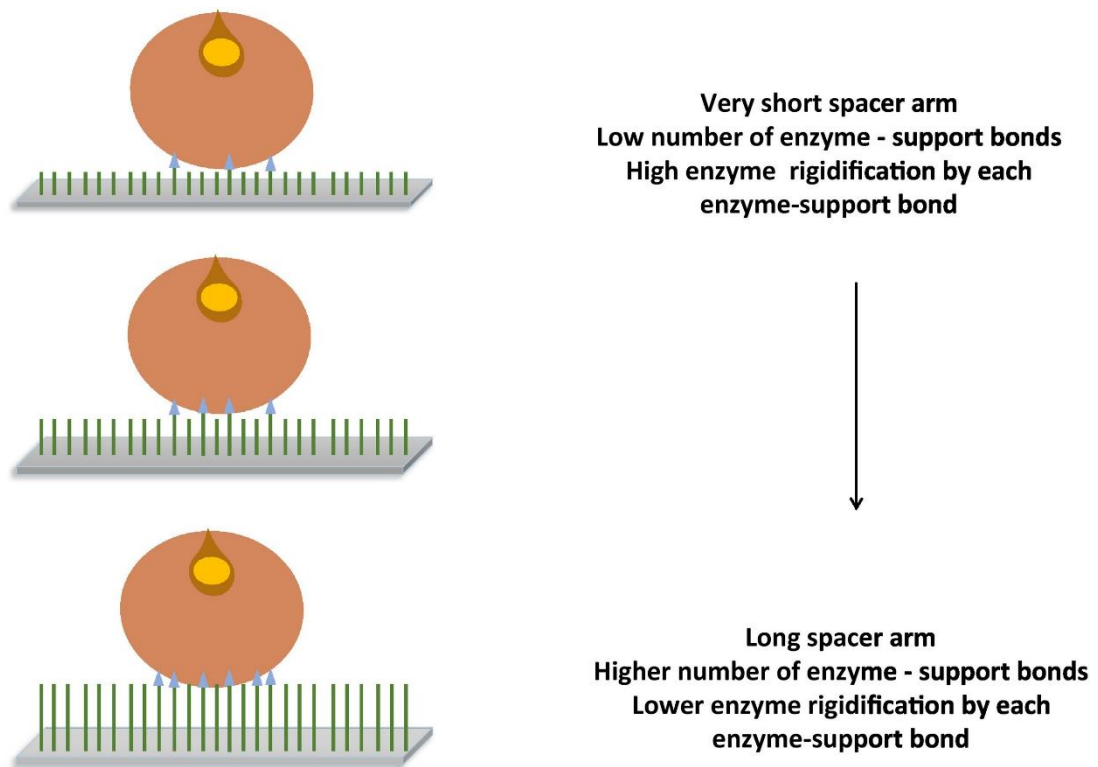
Fig. 57 Effect of spacer arm length on multipoint covalent attachment's ability to stabilise enzymes.[207] When the spacer arm is longer, more binding occurs between the enzme and the support.

6.3.2. GOx immobilisation on amine functionalised support

Immobilizing enzymes on glutaraldehyde-activated supports has been primarily used on supports previously activated with amine groups. Therefore, the supports are positively charged; hence, the immobilisation is usually promoted through a two-step mechanism: in the first step, the enzyme is adsorbed on the support *via* an anionic exchange mechanism, and then the covalent immobilisation occurs. In this work, the

surface of agarose beads were functionalised with amine, and two different crosslinking approaches were tested:

- Amine functionalised agarose first pre-activated with glutaraldehyde, then involved with the GOx immobilisation reaction

- Amine functionalised agarose first involved with GOx immobilisation, then crosslinked with the glutaraldehyde

6.3.3. GOx immobilisation on glutaraldehyde pre-activated support

As mentioned in the previous section, it has been pointed out that the length of the spacer arm can significantly alter the immobilisation results.[309] therefore, the GOx immobilisation was tested on monoaminoethyl-N-ethyl-agarose (MANAE-agarose). The MANAE-agarose was prepared according to Fernandez-Lafuente et al.,[237] and pre-activated with glutaraldehyde according to Vieira et al.[238] to have a longer spacer arm for GOx attachment (Fig. 58).
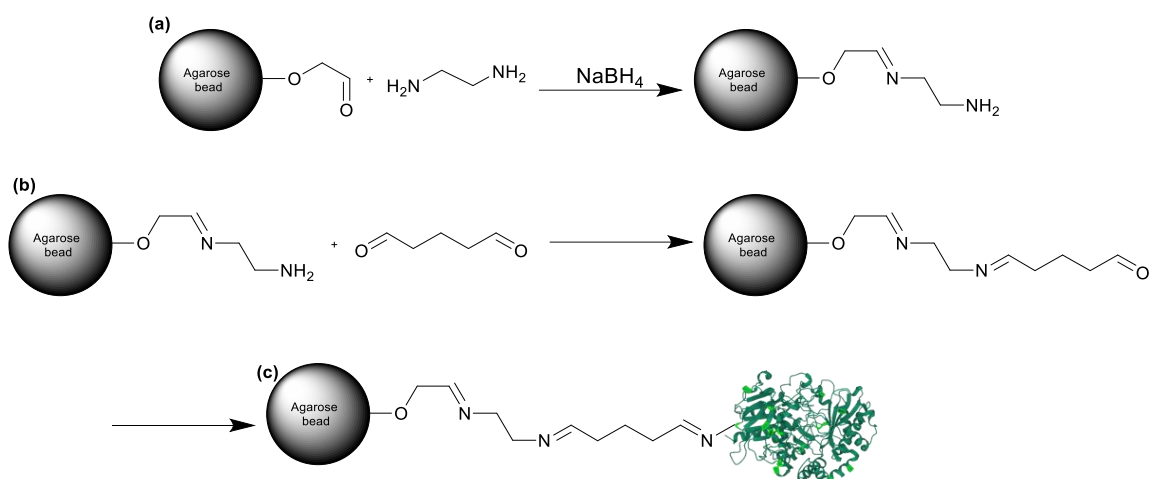
Fig. 58 Schematic presentation of MANAE preparation and GOx immobilisation. (A) preparation of MANAE. (B) pre-activating of MANAE with glutaraldehyde. (C) GOx immobilisation on glutaraldehyde activated MANAE.

As the Gox immobilisation on the pre-activated MANAE may occur across a wide pH range, the immobilisation was evaluated in three different buffers of Acetate pH 5.0, PBS pH 7.0, and Phosphate pH 9.0 to see whether the pH difference can alter the stability of the GOx, as described in section 2.8.3.

Fig. 59A shows that the immobilisation was fast, and all the enzymes were fully immobilised since no activity was observed after 15 minutes in the supernatant solution. This efficient enzyme immobilisation might be attributed to the longer spacer arm, as shown in Fig. 58C. The presence of primary amino groups with low pK_a values between the glutaraldehyde molecule and the support surface is another factor contributing to this quick immobilisation. This indicates that, even though the most reactive amino group—the one with the lowest pK_a—is theoretically what promotes immobilisation of glutaraldehyde, in practice, this is accomplished through a two-step

process: first, the protein binds to the support with the ionic exchange, and then, second, a covalent reaction takes place. To see the immobilised GOx stability, the thermal inactivation process was inducted. The immobilised enzyme was very stable and did not reach its half-life within one day at 50 °C. Therefore, the thermal inactivation temperature was increased to 55 °C to accelerate the inactivation. As seen in Fig. 59B, the free enzyme reached its half-life within 15 minutes. However, the adsorbed enzyme was slightly more stable and reached its half-life in 30 minutes. This poor adsorbed enzyme's stability on the MANAE may be attributed to the GOx adsorbed on the support with weak physical adhesion. Therefore, it easily desorbs through the inactivation process and lose activity. However, the stability has dramatically increased when the enzyme is immobilised via covalent bonding with glutaraldehyde.[306] Fig. 59B shows that the immobilised GOx on the preactivated glutaraldehyde is very stable since it reaches its half-life after 240 minutes. This enzyme stability may be attributed to the GOx immobilising with multiple covalent attachments on the longer spacer arms, which firmly keeps the enzyme on the support.[207] The immobilisation pH, however, had no significant effect on the GOx stability. This might be a very rapid enzyme immobilisation process that does not let the enzyme alter the orientation, or the enzyme has no significant charge distribution on the surface.
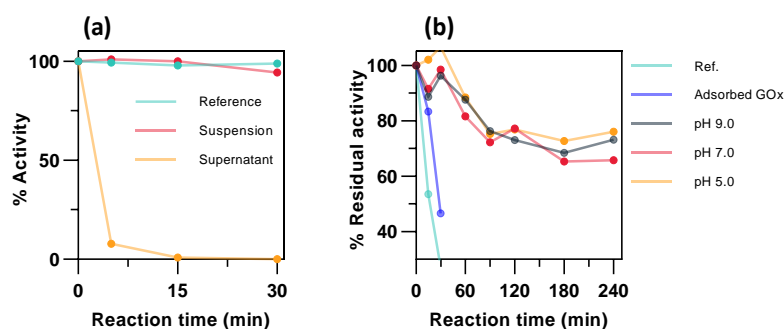
Fig. 59 GOx immobilisation results on pre-activated MANAE. (A) GOx immobilisation rate. (B) Thermal inactivation at 55 °C, pH 7.0.

As shown in Table 5, the GOx lost a small amount of its initial activity after immobilisation, mainly because of rigidification and the loss of enzyme freedom due to the immobilisation. Following immobilisation, the sample was washed and incubated for three days in a more alkaline PBS solution (pH 8.0) to get a multipoint covalent attachment.[207] Further rigidification and immobilisation of the enzyme resulted from this process, which led to more activity loss.

Table 5 Activity loss after GOx immobilisation and incubating in pH 8.0. After incubation at pH 8.0, enzyme immobilised in carbonate buffer loses less of its initial activity compaired to the enzyme immobilised in higher pH buffer (PBS and Acetate).

	Carbonate	PBS	Acetate
Activity loss after the immobilisation	86.91%	86.23%	83.29%
Activity loss after incubating in pH 8.0	87.56%	77.50%	63.58%

6.3.4. GOx immobilisation with glutaraldehyde crosslinking

Although this technique is very efficient in GOx immobilisation, immobilising the enzyme for the EFC may not be beneficial. This is because the longer spacer arm decreases the ET between the electrode and enzyme, as indicated in section 2.8.1. The ET reduces exponentially for the spacer arms longer than eight carbons ~ 15 Å. To solve this problem, the enzyme was first physically immobilised on MANAE-agarose before crosslinking with glutaraldehyde (Fig. 60).
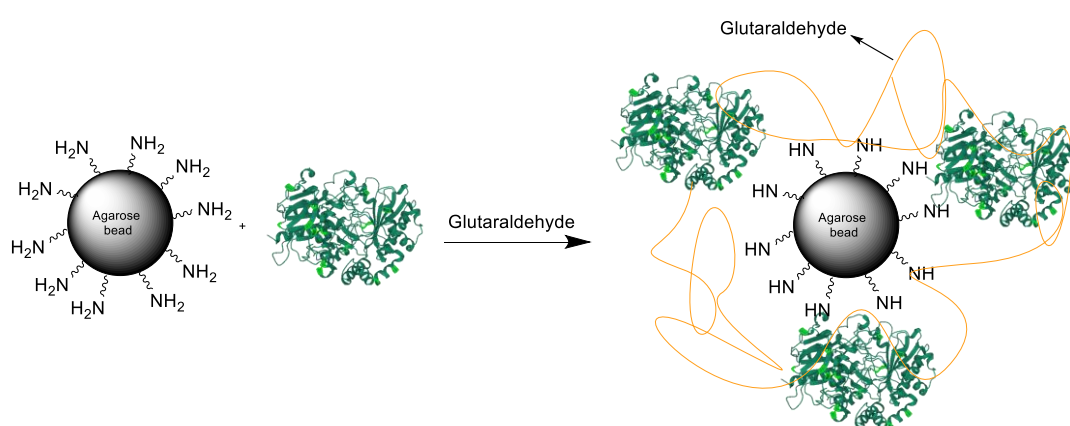
Fig. 60 Schematic presentation of GOx on the MANAE and crosslinking with glutaraldehyde.

The rate of enzyme immobilisation (with physical adsorption) on MANAE-agarose was comparable to that of pre-activated MANAE. The enzyme adsorbed MANAE-agarose was then washed and incubated for one hour with 1% glutaraldehyde to crosslink the enzyme to the support. As demonstrated in Fig. 61A, the enzyme's activity has reduced after adding glutaraldehyde. As previously indicated, this activity reduction may be attributable to the enzyme rigidification and losing its freedom because of effective covalent crosslinking. Similar to the pre-activated MANAE, the

crosslinked GOx was inactivated in PBS with a pH of 7.0 and a temperature of 55 °C (Fig. 61B). After 240 minutes, the activity of the crosslinked GOx on the MANAE had decreased by only ~20%. This demonstrates that enzyme stabilisation is very effective and efficient. In order to obtain the enzyme's half-life, the immobilised enzyme was inactivated at a higher temperature (Fig. 61C). After four hours, the immobilised enzyme achieved its half-life, and no significant difference was observed between the immobilised enzyme at the three different pH levels.
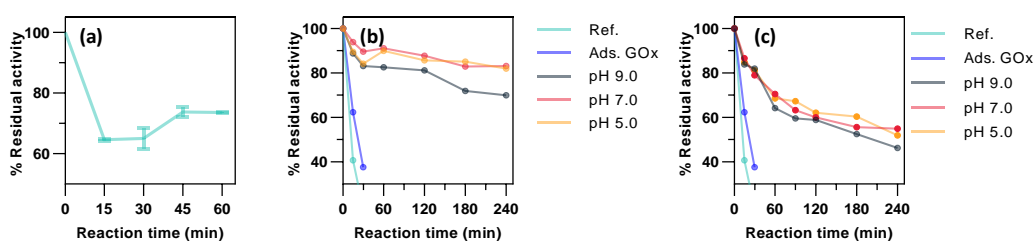
Fig. 61 GOx immobilisation using the crosslinking technique. (A) Residual activity of GOx after adding glutaraldehyde through crosslinking. Crosslinked enzyme inactivation at 55 °C (B) and 60 °C (C).

6.4.   GOx immobilisation via cysteine and/or cysteamine

A chemical with a thiol group on one side can be used to functionalise the gold surface with an amine. Cysteine and cysteamine are attractive compounds for amine functionalizing gold because the thiol group on one side of these molecules can tightly bind to gold, and the amine group on the other may be utilised to immobilise certain enzymes. To evaluate the efficiency of enzyme immobilisation on the amine group that provides a similar surface to ethylenediamine-functionalised agarose (MANAE),

the epoxy-agarose was functionalised with cysteamine (Fig. 62A-B). The resultant immobilisation of GOx was equally effective as MANAE. Fig. 62E shows glucose oxidase undergoes rapid ion exchange with Cysteine (Cys) on the anion exchanger; however, it was only immobilised by a very small percentage using the mixed anion exchanger. That means that the enzyme glucose oxidase was able to establish multiple ion interactions using amino support, while no so much using an amino/carboxylic support, in opposition to other enzymes, like penicillin G acylase that readily immobilised in mixed ion exchangers but not in cation or anion exchangers.[310] That way, the Cys activated support was discarded. After the glutaraldehyde treatment, the activity of the immobilised enzyme was around 85% of the initial one.

Interestingly, the enzyme stability significantly increased after this treatment, as previously reported using MANAE-agarose.[234] The free GOx and physically adsorbed GOx on the cysteamine (Cys this sounds to cysteine, change-GOx) lost their activity within one hour of inactivation at 55 °C. On the other hand, over 80% activity of the GOx was observed even after four hours under these conditions. This should be caused by promoting an intense enzyme-support multipoint attachment that promotes enzyme rigidification, although some inter or intramolecular protein crosslinking cannot be discarded.[191,207] This immobilisation protocol, the amine functionalisation with cysteamine and then glutaraldehyde treatment, was used to immobilise the GOx on the gold electrode. All enzymes were quickly adsorbed to the support, with no enzyme activity measured in the supernatant 15 minutes after immobilisation. This high enzyme adsorption rate may be attributed to the presence

of a primary amino group with a low pK_a, which deprotonates rapidly and aids GOx adsorption through an ionic exchange.

The adsorption phase may be helpful since it reduces the overall immobilisation time. Nonetheless, the adsorption step also influences the enzyme's orientation on the surface of the support, which in some circumstances might lead to a less active and/or stable immobilised derivative due to a less suitable position for subsequent covalent bond formation or limited substrate access to the active site.[306] Therefore, it is necessary to immobilise the enzyme using glutaraldehyde which does not absorb enzymes fast.

To find the way to decrease adsorption rate, in this study, epoxide groups were activated with cysteine, which includes a secondary amine with a higher pK_a, and enzyme immobilisation was examined on it (Fig. 62C). Enzyme immobilisation did not occur. All enzymes remained in the supernatant, as shown in Fig. 62F. This may be due to the development of one secondary amino group and one carboxylic group on the surface due to the cysteine. This is because the total charge of this support area is zero, preventing the adsorption generated by contact between oppositely charged portions of the support and the enzyme. Therefore, this method may not be suitable for immobilizing GOx on our 3D-printed gold electrode. As a compromise, cysteine and cysteamine were combined in a molar ratio of 0.8:0.2 on epoxy-agarose (Fig. 62D). According to Fig. 68G, the GOx was completely immobilised slowly and effectively after 90 minutes. Since the rate of enzyme immobilisation was slowed, it was anticipated that GOx would have sufficient time to immobilise with a more favourable

3 D - p r i n t i n g   o f   e n z y m a t i c
b i o f u e l   c e l l s
166 | P a g e

orientation to attain better stability. However, since the adhesion between the enzyme and support was so poor, all immobilised enzymes were desorbed after washing.

For this reason, the washing step prior to glutaraldehyde crosslinking was removed. Although there was some activity in GOx-immobilised agarose, the overall activity was much lower than in cysteamine-immobilised agarose because very little enzyme was immobilised due to the decrease enzyme adhesion. Due to the decreased effectiveness of enzyme immobilisation, this approach may not be suited for GOx immobilisation for EFCs and will result in the EFCs' low power density.
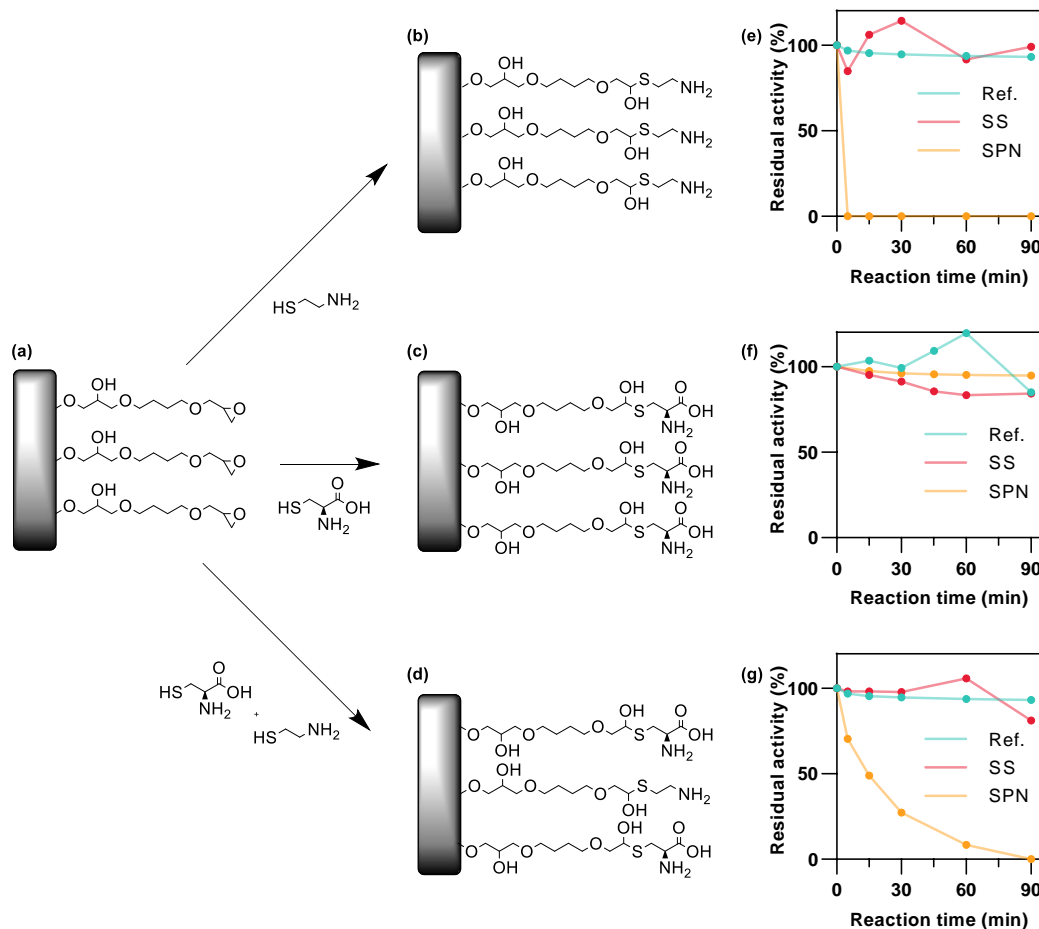
Fig. 62 Enzyme immobilisation on cysteine and cysteamine functionalised surfaces. (A) Epoxide agarose. Surface functionalisation reaction with cysteamine (B), (C) cysteine, and a combination of cysteine and cysteine with the molar ratio of 8:2 (D). Enzyme immobilisation (adsorption) rate on the agarose functionalised with cysteamine (E), cysteine (F), and a combination of cysteamine and cysteine. While enzymes are immobilised, the enzyme activity in the suspension (SS) drops slightly due to immobilisation. But the activity of the enzyme in the supernatant (SPN) drops significantly as the concentration of the enzyme decreases.

6.5. Electrocatalytic characterisation of EFC

The GOx can specifically interact with glucose and use enzymatic electrochemical processes to transform it into gluconolactone. The electron may be transported from the enzyme to the electrode under the right circumstances. This

ideal circumstance is a function of the facile electron transport and the good conductivity of the current collector. The porous gold structure is a good candidate for EFCs due to its intriguing characteristics. These includes its 3D bicontinuous open pore network structure, high surface-to-volume ratio compared to bulk metals, distinctive electronic properties, nontoxic nature, high recyclability, and relatively simple recovery.[311] It is safe for implanting purposes because of its excellent biocompatibility and high conductivity, which enables the flow of electrons between enzyme and electrode. Thin nanoporous gold films have often been selected to be employed as an electrode because of these characteristics.[21,312–314]

The development of the highly conductive 3D current collector and identification of the ideal GOx immobilisation reaction has been discussed in earlier chapters. This chapter explains how to immobilise the enzyme on a 3D current collector to produce power from glucose by combining the previously stated methods. The following procedures were used to set up the EFC:

- The wire was first connected to the 3D gold electrode (Fig. 63A)

- Optimum enzyme immobilisation, obtained from testing on agarose, was conducted to attach the GOx to the gold through the following process:

    o The gold microelectrode amine was functionalised by soaking it in 1M of cysteamine (Fig. 63B).

    o The sample was washed and immersed in 10mL GOx solution with 5μg/mL concentration in PBS 5mM (Fig. 63C).

o The enzyme immobilised electrode was then washed and soaked in 1% glutaraldehyde solution for one hour to crosslink the GOx to the electrode (Fig. 63D).
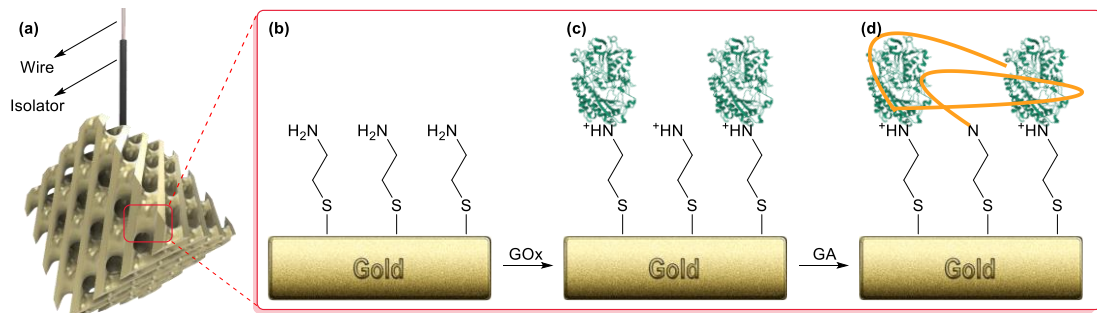
Fig. 63 Schematic presentation of 3D EFC bioanode preparation for electrochemical characterisation. (A) Connecting wire to the 3D gold microelectrode. (B) Amine functionalisation of the gold surface with cysteamine. (C) The GOx adhesion on the electrode. (D) Crosslinking enzyme with glutaraldehyde.

The high conductivity of the gold electrode, along with the large catalytic surface area produced by the electrode's 3D structure created in this work, enhances the current output of the EFCs.

6.6. Bioanode preparation

An enzyme must be immobilised to produce an electrochemical current in enzymatic biofuel cells. . As the first approach, the copper wire was connected to the gold electrode using silver paste. The wire was then isolated using dielectric polymer paste (Fig. 64A). The glucose oxidase was utilised to be immobilised on the gold electrode. This is a dimeric enzyme containing one FAD molecule per enzyme subunit and catalyses the oxidation of β-D-glucose to D-glucono-δ-lactone producing

hydrogen peroxide (H_2O_2) as a by-product, with molecular oxygen acting as an electron acceptor.[315–317] The glucose oxidase was utilised as a model enzyme since it is often used in producing enzymatic biofuel cells.[318,319]

To functionalise the gold electrode, cysteamine was utilised. This provided a monolayer of primary amino-groups, converting the surface support in an anion exchanger using cysteamine.[320–322] Nevertheless, mere ion exchange wasn't sufficient to produce a stable biocatalyst. For this reason, stabilising the enzyme via multipoint covalent attachment was used,[207] using the glutaraldehyde chemistry in this first approach. This is a very versatile immobilisation strategy,[231,301,323], which has been successfully previously applied to immobilise-stabilise this enzyme in MANAE-agarose, obtaining the highest stability after treating the enzyme previously adsorbed on the aminated support surface with glutaraldehyde.[234] Fig. 64B shows that 20% of the offered enzyme activity was immobilised on the electrode surface within the first 30 minutes of the immobilisation reaction. That means 10 μg of enzyme was immobilised on each gold lattice electrode. No enzyme immobilised after 30 minutes, suggesting the electrode surface is saturated with the enzyme.
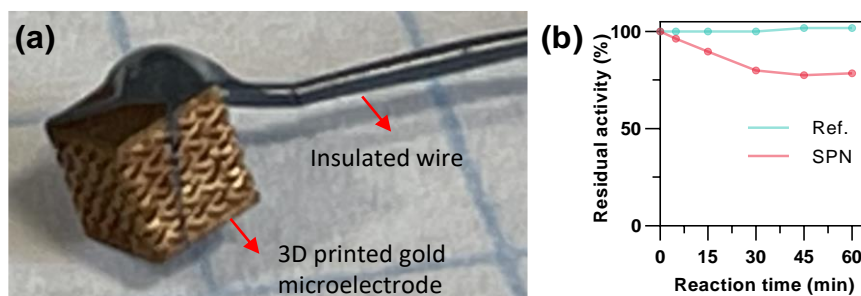
Fig. 64 The preparation of enzymatic 3D gold electrode. Wire was first connected to the electrode (a). The electrode was then involved with optimum enzyme immobilisation reaction, in which 20% total amount of the enzyme immobilised on the gold electrode (b).

6.7.   Cyclic voltammetry analysis of bioanode

The electrocatalytic activity of GOx in the presence of glucose was compared across the electrode surface of 3D-printed lattice and cube bioanodes using cyclic voltammetry (CV). As shown in Fig. 65A, the CV analysis cell consisted of three electrodes:

- **The working electrode (WE):** The GOx immobilised 3D gold electrode.

- **The counter electrode (CE):** Made of platinum wire.

- **The reference electrode (RE):** Reference electrodes have an electrochemical potential that is constant, well-known, and well-defined.

The WE are where the chemistry of interest occurs, and the CE is the other half of the cell. The applied potential (EA) is measured between the working electrode and the counter electrode, and the resultant current is measured in the working or counter electrode lead. The purpose of the reference electrode is to serve as a reference while

monitoring and adjusting the working electrode's potential, without transmitting any current. Based on the applied voltage change, the electron current—the product of enzymatic activity in the WE—is measured. This analysis was carried out in PBS (100 mM, pH 7) saturated with nitrogen gas at a concentration of 50 mM glucose solution and 0.5 mM ferrocenemethanol as a redox mediator. The 50 mM concentration of glucose was chosen since it has been recognised as an optimum concentration for bioanode performance.[324,325] The 3D-printed cube bioanode did not show a significant electrocatalytic oxidation effect in the presence of 50mM glucose, as shown in Fig. 65B. The 3D-printed diamond lattice bioanode, on the other hand, demonstrated a clear mediated electrocatalytic glucose oxidation current observed by the increase of the ferrocenemethanol oxidation wave while its reduction wave disappeared (Fig. 65C). The catalytic current of 2.5 µA at 0.35 V was measured per the 2 mm^3 of the diamond lattice microelectrode, which is almost ten times higher than 0.27 µA current of the cube microelectrode with the same dimension. The obtained results demonstrate that the combined advantages of high conductivity and large catalytic surface area of the 3D printed gold microelectrode significantly increased the enzymatic anode efficiency for glucose oxidation and consequently enhanced the current output of the EFC.
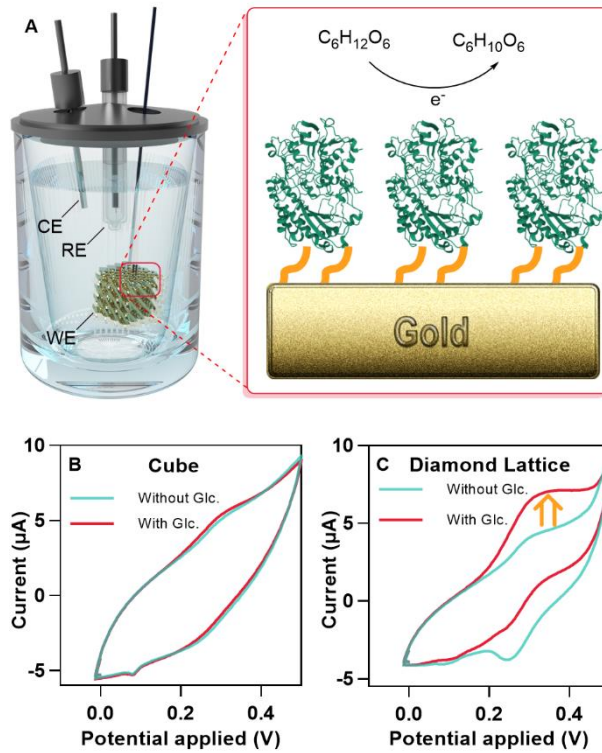
Fig. 65 Application of 3D printed microelectrodes as an enzymatic anode: (A) Schematic representation of the enzymatic glucose oxidation process inside an electrochemical cell. Cyclic voltammetry curves of glucose oxidation with cube (B) microelectrodes and diamond lattice form (C).

6.8.   Summary

This chapter thoroughly analysed the stability of the free and immobilised enzyme. Various surface functionalisation and enzyme techniques were tested on agarose to find the optimal protocol for GOx immobilisation. Several hypotheses were answered using these techniques summarised in Fig. 66. On the aldehydes with short spacer arms, the immobilisation of the enzyme is very poor. GOx immobilisation is effective on amine-functionalised surfaces with long spacer arms. GOx immobilisation by glutaraldehyde crosslinking and pre-activating, resulting in high stability of the enzyme. The crosslinking method offers a smaller space between the enzyme and support, making it more advantageous for EFC applications. The crosslinked enzyme has the same level of stability as the pre-activated support. GOx immobilisation on cysteine or a mixture of cysteine and cysteamine functionalised surfaces was not achievable. So, the optimal method for immobilizing GOx is for our EFC is to functionalise the surface of the 3D-printed gold electrode with cysteamine, immobilise the enzyme by adsorption, and then add glutaraldehyde to create a covalent crosslinking between the enzyme and the support.
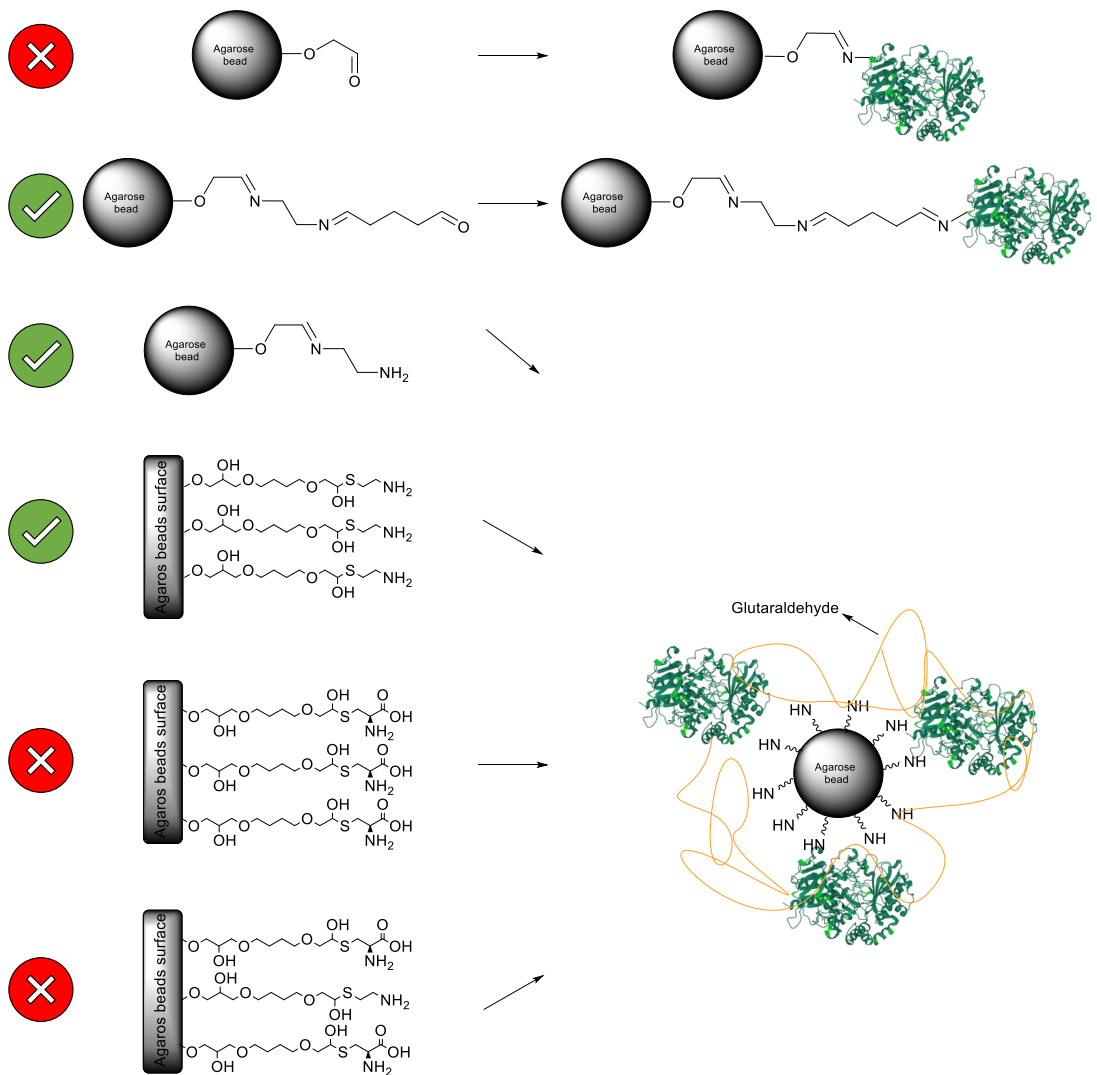
Fig. 66 An overview of the potential feasibility of immobilizing GOx using several enzyme immobilisation techniques.

DISCUSSION

7. Discussion

This work was conducted to create a reliable and effective 3D microelectrode for use in EFCs. PμSLA makes it possible to create 3D microstructures with more catalytic surface area, high resolution in the micro-regime, and fast printing speeds.[10] For the purpose of miniaturising EFCs, this printing resolution is essential because it can creates large surface area to volume ratio (46.5 mm^2 per square centimetre for diamond lattice). The stereolithography technique can only print a polymer that is typically not conductive or just marginally conductive, which presents difficulties for manufacturing microelectrodes. This issue was solved by adding a thiol-containing adhesion layer on the surface of a printed polymer, which provides strong adhesion between a polymer and metal coating via electroless plating and high electrical conductivity. The surface of the printed item was then post-functionalised with thiol groups to promote a strong chemical bond between the polymer and the gold that was being deposited using the electroless plating method. Glucose oxidase was immobilized on the gold electrodes via covalent attachment and tested as an enzymatic bioanode to demonstrate the 3D printed microstructures for enzymatic biofuel cells.

The findings in this research demonstrate that functionalising the multiacrylate monomer, PETTA in this instance, using MPTMS yields functionalised photocurable monomer. While prior research has focused on the 3D printing of monomers using the

2PP technique,[92] our findings reveal that the monomer can also be printed using the PµSLA approach by adding appropriate amount of curcumin as a photo-absorber, and Irgacure 819 photoinitiator. All the ingredients of this ink was carefully selected to be biocompatible, so that it can be used as an implanting purpose and tissue engineering. Printing this functional monomer with PµSLA enabled the fabrication of complicated components on a bigger scale and more quickly than with 2PP. With the addition of an optimal quantity of photoinitiator, the maximum DP of 70 per cent functional monomer can be attained, which is higher in comparison to earlier comparable DP investigations on acrylate monomer.[326–329] A likely reason for this higher DP is that the Irgacure 819 is more efficient with UV light of DLP-based printers than the IR light of 2PP, resulting in more efficient polymerisation. What can be clearly seen in Fig. 34C is that the DP does not dramatically enhance while using a lower amount of photoinitiator. Therefore, 0.5 weight per cent of Irgacure may be applied if the photoinitiator is potentially toxic for implanting purposes, and a longer exposure time may compensate for a little drop in polymerisation. Using curcumin as a photoabsorber and optimising the printing parameters, the monomer could be precisely printed to fabricate complicated shapes using PµSLA. However, the results are not examined using other VP strategies to ensure their applicability. The printability of the material may thus need to be investigated further using DLP and SLA methods to fabricate a functional component at larger sizes.

The NMR results of the MP monomer prepared in this study back up the method presented by Yee et al.[92], who developed a method of PETTA functionalisation with

MPTMS, which allowed for post-functionalising the 3D-printed microstructure with different functional groups thanks to the presence of the silanol group on the surface. However, the author did not attempt to ascertain whether it could silanise the printed microstructure. This study shows the possibility of silanising the 3D-printed microstructure with various functional groups for various applications. Although extensive research has been conducted on functionalising the 3D printed polymer to coat the 3D printed polymer with metal effectively, no study exists to quantify the association between silanisation reaction conditions and coating and find a threshold for the amount of the thiol for the coating. For this reason, the experiment in this study offers a particular understanding of the relationship between the functionalisation reaction time and the conductivity and adhesion of the gold that has been deposited, as well as a threshold for the quantity of thiol needed for the optimal gold coating. Thiol increases adhesion and conductivity by increasing the amount of thiol on the surface up to four-hour sol-gel process. However, the adhesion and decreased with longer functionalisation reaction time. This could be justified according to the theory presented by Hsu et al, once the surface is saturated with the sol-gel reaction, excess silane groups precipitate and attach to the surface with weak physical attachments. The gold that attaches to the thiols also attaches to the polymer surface with weak physical bonds.[289] After three to four hours of functionalization, the polymer's surface appears saturated with silane groups, and further functionalization does not seem to increase adhesion substantially. Therefore, the maximum level of gold attachment may be attained after just three hours of a sol-gel reaction. This

process allows gold plating a 3D-printed object to provide two additional benefits. First, electroless gold may be created in any wet-chemical laboratory. Furthermore, unlike the sputter method procedure, electroless gold coatings may be applied to substrates with complex geometries.[330] One intriguing finding is that this study's optimal silanisation process yielded exceptional gold conductivity deposited on the 3D-printed structure. This is an improvement of four orders of magnitude above the gold coating of the 3D-printed microstructure found in earlier study.[121] The reason for this high conductivity may be attributed to the thiol groups on the substrate surface, which draw gold ions and nanoparticles and form a thin, compact, and homogeneous coating on the surface.[331,332] For the same reason, in contrast to previous reports, the deposited gold stayed intact even after a rigorous adhesion test. The evaluation of various metal depositions on the functionalised components may also provide exciting findings in creating a variety of metal foams, pointing to interesting avenues for future research. The as-prepared 3D gold part has a large surface area and conductivity, making it an ideal microelectrode for the EFCs. To immobilize the electrode optimally, optimising the enzyme immobilisation reaction was explored.. While several efforts have been made to immobilise enzymes by covalent bonding, a comparison of different immobilisation proteolytic strategies was not discovered in a literature study. In order to establish the suitable technique to immobilise the enzyme on the electrode, the current investigation was made to ascertain the impact of the functional group and spacer arm on the enzyme immobilisation. Surprisingly, the enzyme did not immobilise on the agarose that had been chemically functionalised

with an aldehyde group. The results disagree with those of Vieira et al.[238], who reported a GOx immobilisation yield of 71% on glyoxyl agarose support. This discrepancy in findings may be due to the fact that enzyme suppliers use varying methods of manufacture, resulting in somewhat varied enzyme surfaces. The poor GOx immobilisation on the glyoxyl-agarose may be explained by Rodrigues et al.[207] hypothesis, according to which the immobilisation of an enzyme relies not only on the functional group on the surface but also on the enzyme's adsorption with ionic exchange and spacer arm length. In accordance with idea, the GOx has connected to the MANAE-agarose efficiently and rapidly. This enzyme immobilisation with the ionic exchange, however, did not massively improve the stability of the enzyme since it lost its activity immediately through inactivation process.

In contrast, the enzyme became very stable after covalent bonding. This finding suggests that the enzyme is adsorbed onto the support surface with the assistance of the amine groups, which are subsequently crosslinked by glutaraldehyde. Although prior studies have emphasised the significance of amine functionalisation on the immobilisation of the enzyme, no work has been done to study the difference between the amine groups. Due to this, the effectiveness of the two amine groups most often utilised for enzyme immobilisation was examined. The MANAE-agarose test predicted that the GOx immobilisation would be very effective when the surface was functionalised with cysteamine. Contrary to expectations, the immobilisation of GOx in this investigation did not result in an effective immobilisation on the cysteine functionalised agarose. Two key factors relating to the cysteine may be responsible

for this poor enzyme adhesion. One reason is that cysteine is more difficult to deprotonate and ion exchange with enzymes because of its secondary amine group, which has a higher pK_a. Second, the carboxylic group oxygens are negatively charged, which likely repulses the enzyme's negative charge.[306] This result contrasts with other research that functionalised the support surface for the GOx attachment using cysteamine.[176,304,333]

In prior investigations, the glutaraldehyde pre-functionalisation of the cysteine-activated surface may account for the discrepancy in findings. As a result, the immobilisation of the cysteine was more successful because of the longer spacer arm. This study did not attempt pre-activating the surface with glutaraldehyde since the goal is to reduce the distance between the electrode and the enzyme to promote ET. Because of this, it was determined that the cysteamine was the best functional group to use in functionalising the gold surface for the GOx attachment to form the bioanode. Despite these encouraging findings, there is still more that can be done to understand better how surface charge affects the attachment of the enzyme.

Cyclic voltammetry was then used to evaluate bioanode effectiveness. The results of this study support the idea that AM can improve current density through the increase of microelectrode surface areas.. Although the current density attained in this study is less than that of a bioanode that had previously been made using nanomaterials, this research finding paves the path for AM of EFCs. Because VP offers design freedom, microelectrodes with larger surface areas may be produced. Additionally, this technology demonstrates the potential of producing gold electrodes

with a large surface area in substitution of carbon nanomaterials, which have limitations in biocompatibility and mass transfer. Although the findings are encouraging, there are still questions on how geometry affects the EFCs' efficacy. The optimisation of the cell shape via further computational fluid dynamics (CFD) study might thus provide some very intriguing findings.

8. Conclusion and recommendation for future work

8.1. Conclusion

The study's findings suggest that integrating VP with surface functionalisation and electroless plating increase the effectiveness of the EFCs. The Michael-thiol reaction with multiacrylate monomers was used to create the functional printable ink, which was then mixed with the biocompatible photoinitiator and photoabsorbers. This functional ink was successfully printed with PμSLA, functionalised with thiol using the optimal sol-gel process. Thiol groups on the surface of the polymer made the gold coating on the 3D-printed material exceedingly successful; the gold was firmly bond to the polymer and had high conductivity (53% of bulk gold). These characteristics enable the electrode to function as a reliable current collector for the EFC.

Testing GOx immobilisation on agarose revealed that the enzyme is highly stable on gold is by crosslinking the GOx on a surface functionalised with cysteamine. The 3D microelectrode's electrochemical performance as an enzyme anode for usage in enzymatic biofuel cells was evaluated. Due to the increased catalytic surface area compared to a simple cubic electrode, the high performance of EFC based on the 3D printed lattice-structured gold microelectrode was demonstrated. The study enables the suggested technology to be used not only for enhancing EFCs but also for applications in implanted energy supply devices and self-powered biosensors.

8.2. Recommendation for future work

This work has opened up new avenues for future research on using of SLA printing technique to enhance the efficiency of the implantable EFCs and biosensors. It is highly advised to carry out further research and testing on the microelectrode's

potential applications. The following suggestions may be used to expand the knowledge beyond what was done in this work:

- The sol-gel reaction described in this work is a highly flexible technique for attaching various functional groups. A variety of silane functional groups, including amine, aldehyde, and epoxy groups, may be employed to attach to different biomolecules, cells, and bacteria immobilised on the 3D-printed object using the surface functionalisation technique described in this work.[334–337]

- It has been shown that the immobilising of GOx on the gold nanoparticles[162,212,338] and CNTs[339] can enhance DET. This immobilised enzyme on the nanomaterials may then immobilise the created 3D-printed gold electrode to promote DET and further increase the electrode's surface area.[340]

- The methodology developed in this work offers design freedom to create EFCs. The design of the EFC may be optimised using Computational Fluid Dynamics (CFD) analysis to obtain optimum mass transfer efficiency without sacrificing surface area. The relationship between the lattice geometry and EFC efficiency may be understood by experimenting with various lattice structures with varying porosity.

- Different plating techniques may be employed in place of the electroless gold plating reported in this work since the thiol functionalised 3D part can help with the adhesion of other kinds of metals. This could make it possible to

fabricate various metal structures to provide the optimum catalytic supports.[341]

- The 3D-printed gold structure can catalyse various reactions that may be used in many industries, such as hydrogen production in water electrolysers,[342,343] reduce CO_2 to produce other useful organic materials,[344] and nitrogen reduction to ammonia.[345,346] The gold electrodes may be produced on a larger scale using SLA or DLP, making them ideal for the uses mentioned earlier.

- A porous transport layer (PTL) for electrolysers can be made using this technology for 3D printing conductive structures. This may provide a chance to improve the PTL shape and facilitate the removal of bubbles from the medium, which will increase the electrolyser's efficiency.[347,348]

- Electrode for flow cells with the best shape and lowest cost may be made using this technology. Flow cells have been used in various fields, such as producing renewable energy and purifying water.[349,350]

- Biocompatible materials were used to create the 3D-printed gold electrode. Consequently, it is appropriate electrode for neuron cell testing.[351]

- Other enzymes, such as nitrogenase, may be immobilised on a 3D-printed gold electrode to produce power simultaneously during ammonia production.[352,353] The high surface area of the AM-made electrode may boost efficiency in the synthesis of ammonia, which is particularly beneficial to the agricultural industries.

- This work's technology for manufacturing 3D-structured EFC may aid in enhancing the sensitivity of enzyme biosensors. For instance, further research may result in the development of glucose sensors.

Overall, 3D printing gold microelectrodes hold immense potential for revolutionising future applications. The outcome of this research can be used as a toolkit to fabricate various 3D metal microstructures that will have a significant impact on the fields of sensors, catalysts, and enzymatic biofuel cells, offering enhanced capabilities, design versatility, and increased accessibility. It holds the promise of driving innovation and opening up new possibilities for a range of applications in the future.

REFERENCES

(1)   Carrión-Camacho, M. R.; Marín-León, I.; Molina-Doñoro, J. M.; González-López, J. R. Safety of Permanent Pacemaker Implantation: A Prospective Study. *J. Clin. Med.* **2019**, *8* (1), 35. https://doi.org/10.3390/jcm8010035.

(2)   du Toit, H.; Di Lorenzo, M. Continuous Power Generation from Glucose with Two Different Miniature Flow-through Enzymatic Biofuel Cells. *Biosens. Bioelectron.* **2015**, *69*, 199–205. https://doi.org/10.1016/j.bios.2015.02.036.

(3)   Rasmussen, M.; Abdellaoui, S.; Minteer, S. D. Enzymatic Biofuel Cells: 30 Years of Critical Advancements. *Biosens. Bioelectron.* **2016**, *76*, 91–102. https://doi.org/10.1016/j.bios.2015.06.029.

(4)   Kim, B. C.; Lee, I.; Kwon, S. J.; Wee, Y.; Kwon, K. Y.; Jeon, C.; An, H. J.; Jung, H. T.; Ha, S.; Dordick, J. S.; Kim, J. Fabrication of Enzyme-Based Coatings on Intact Multi-Walled Carbon Nanotubes as Highly Effective Electrodes in Biofuel Cells. *Sci. Rep.* **2017**, *7* (December 2016), 1–10. https://doi.org/10.1038/srep40202.

(5)   Wen, D.; Eychmüller, A. Enzymatic Biofuel Cells on Porous Nanostructures. *Small* **2016**, *12* (34), 4649–4661. https://doi.org/10.1002/smll.201600906.

(6)   Murata, K.; Kajiya, K.; Nakamura, N.; Ohno, H. Direct Electrochemistry of Bilirubin Oxidase on Three-Dimensional Gold Nanoparticle Electrodes and Its Application in a Biofuel Cell. *Energy Environ. Sci.* **2009**, *2* (12), 1280–1285. https://doi.org/10.1039/b912915d.

(7)   Inamuddin; Shin, K. M.; Kim, S. I.; So, I.; Kim, S. J. A Conducting Polymer/Ferritin

Anode for Biofuel Cell Applications. *Electrochim. Acta* **2009**, *54* (16), 3979–3983. https://doi.org/10.1016/j.electacta.2009.02.020.

(8)   Wong, T. S.; Schwaneberg, U. Protein Engineering in Bioelectrocatalysis. *Curr. Opin. Biotechnol.* **2003**, *14* (6), 590–596. https://doi.org/10.1016/j.copbio.2003.09.008.

(9)   Song, Y.; Penmatsa, V.; Wang, C. Modeling and Simulation of Enzymatic Biofuel Cells with Three-Dimensional Microelectrodes. *Energies* **2014**, *7* (7), 4694–4709. https://doi.org/10.3390/en7074694.

(10)   Al Rashid, A.; Ahmed, W.; Khalid, M. Y.; Koc, M. Vat Photopolymerization of Polymers and Polymer Composites: Processes and Applications. *Addit. Manuf.* **2021**, *47*, 102279.

(11)   Pagac, M.; Hajnys, J.; Ma, Q.-P.; Jancar, L.; Jansa, J.; Stefek, P.; Mesicek, J. A Review of Vat Photopolymerization Technology: Materials, Applications, Challenges, and Future Trends of 3d Printing. *Polymers (Basel).* **2021**, *13* (4), 598.

(12)   Nakashima, N. *Nanocarbons for Energy Conversion: Supramolecular Approaches*; Springer, 2019.

(13)   Choudhary, T. V; Goodman, D. W. CO-Free Fuel Processing for Fuel Cell Applications Choudhary, T. V. and Goodman, D. W. Catalysis Today, 2002, 77, (1–2), 65–78. *Fuel Energy Abstr.* **2003**, *44* (4), 224. https://doi.org/10.1016/S0140-6701(03)82895-3.

(14)   De Poulpiquet, A.; Ciaccafava, A.; Benomar, S.; Giudici-Orticoni, M.-T.; Lojou, E. Carbon Nanotube-Enzyme Biohybrids in a Green Hydrogen Economy. *Synth. Appl. Carbon Nanotub. Their Compos.* **2013**, 433.

(15)   Barton, S. C.; Gallaway, J.; Atanassov, P. Enzymatic Biofuel Cells for Implantable and Microscale Devices. **2004**. https://doi.org/10.1021/cr020719k.

(16)   Cohen, B. The Bacterial Culture as an Electrical Half-Cell. *J. Bacteriol* **1931**, *21* (1), 18–19.

(17)   Song, Y.; Wang, C. High-Power Biofuel Cells Based on Three-Dimensional Reduced Graphene Oxide/Carbon Nanotube Micro-Arrays. *Microsystems Nanoeng.* **2019**, *5* (1). https://doi.org/10.1038/s41378-019-0081-2.

(18)   Yahiro, A. T.; Lee, S. M.; Kimble, D. O. Bioelectrochemistry: I. Enzyme Utilizing Bio-Fuel Cell Studies. *Biochim. Biophys. Acta (BBA)-Specialized Sect. Biophys. Subj.* **1964**, *88* (2), 375–383.

(19)   Berezin, I. V; Bogdanovskaia, V. A.; Varfolomeev, S. D.; Tarasevich, M. R.; Iaropolov, A. I. Bioelectrocatalysis-Equilibrium Oxygen Potential in Presence of Laccase. *Dokl. Akad. Nauk SSSR* **1978**, *240* (3), 615–618.

(20)   Falk, M.; Blum, Z.; Shleev, S. Direct Electron Transfer Based Enzymatic Fuel Cells. *Electrochim. Acta* **2012**, *82*, 191–202. https://doi.org/10.1016/j.electacta.2011.12.133.

(21)   Andoralov, V.; Falk, M.; Suyatin, D. B.; Granmo, M.; Sotres, J.; Ludwig, R.; Popov,

V. O.; Schouenborg, J.; Blum, Z.; Shleev, S. Biofuel Cell Based on Microscale Nanostructured Electrodes with Inductive Coupling to Rat Brain Neurons. *Sci. Rep.* **2013**, *3*, 1–11. https://doi.org/10.1038/srep03270.

(22) Song, Y.; Chen, C.; Wang, C. Graphene/Enzyme-Encrusted Three-Dimensional Carbon Micropillar Arrays for Mediatorless Micro-Biofuel Cells. *Nanoscale* **2015**, *7* (16), 7084–7090. https://doi.org/10.1039/c4nr06856d.

(23) Mano, N.; Mao, F.; Heller, A. Characteristics of a Miniature Compartment-Less Glucose-O2 Biofuel Cell and Its Operation in a Living Plant. *J. Am. Chem. Soc.* **2003**, *125* (21), 6588–6594. https://doi.org/10.1021/ja0346328.

(24) Cinquin, P.; Gondran, C.; Giroud, F.; Mazabrard, S.; Pellissier, A.; Boucher, F.; Alcaraz, J. P.; Gorgy, K.; Lenouvel, F.; Mathé, S.; Porcu, P.; Cosnier, S. A Glucose BioFuel Cell Implanted in Rats. *PLoS One* **2010**, *5* (5), 1–7. https://doi.org/10.1371/journal.pone.0010476.

(25) Halámková, L.; Halámek, J.; Bocharova, V.; Szczupak, A.; Alfonta, L.; Katz, E. Implanted Biofuel Cell Operating in a Living Snail. *J. Am. Chem. Soc.* **2012**, *134* (11), 5040–5043. https://doi.org/10.1021/ja211714w.

(26) Szczupak, A.; Halámek, J.; Halámková, L.; Bocharova, V.; Alfonta, L.; Katz, E. Living Battery - Biofuel Cells Operating in Vivo in Clams. *Energy Environ. Sci.* **2012**, *5* (10), 8891–8895. https://doi.org/10.1039/c2ee21626d.

(27) Sales, F. C. P. F.; Iost, R. M.; Martins, M. V. A.; Almeida, M. C.; Crespilho, F. N. An Intravenous Implantable Glucose/Dioxygen Biofuel Cell with Modified

Flexible Carbon Fiber Electrodes. *Lab Chip* **2013**, *13* (3), 468–474. https://doi.org/10.1039/c2lc41007a.

(28)   Zebda, A.; Cosnier, S.; Alcaraz, J. P.; Holzinger, M.; Le Goff, A.; Gondran, C.; Boucher, F.; Giroud, F.; Gorgy, K.; Lamraoui, H.; Cinquin, P. Single Glucose Biofuel Cells Implanted in Rats Power Electronic Devices. *Sci. Rep.* **2013**, *3*, 1–5. https://doi.org/10.1038/srep01516.

(29)   Zebda, A.; Alcaraz, J. P.; Vadgama, P.; Shleev, S.; Minteer, S. D.; Boucher, F.; Cinquin, P.; Martin, D. K. Challenges for Successful Implantation of Biofuel Cells. *Bioelectrochemistry* **2018**, *124*, 57–72. https://doi.org/10.1016/j.bioelechem.2018.05.011.

(30)   Xiao, X.; Xia, H.; Wu, R.; Bai, L.; Yan, L.; Magner, E.; Cosnier, S.; Lojou, E.; Zhu, Z.; Liu, A. Tackling the Challenges of Enzymatic (Bio) Fuel Cells. *Chem. Rev.* **2019**, *119* (16), 9509–9558.

(31)   MacVittie, K.; Halámek, J.; Halámková, L.; Southcott, M.; Jemison, W. D.; Lobel, R.; Katz, E. From "Cyborg" Lobsters to a Pacemaker Powered by Implantable Biofuel Cells. *Energy Environ. Sci.* **2013**, *6* (1), 81–86. https://doi.org/10.1039/c2ee23209j.

(32)   Akiyama, Y.; Ohno, H.; Morishima, K.; Nakamura, N.; Shoji, K.; Suzuki, M. Biofuel Cell Backpacked Insect and Its Application to Wireless Sensing. *Biosens. Bioelectron.* **2015**, *78*, 390–395. https://doi.org/10.1016/j.bios.2015.11.077.

(33)   El Ichi-Ribault, S.; Alcaraz, J. P.; Boucher, F.; Boutaud, B.; Dalmolin, R.;

Boutonnat, J.; Cinquin, P.; Zebda, A.; Martin, D. K. Remote Wireless Control of an Enzymatic Biofuel Cell Implanted in a Rabbit for 2 Months. *Electrochim. Acta* **2018**, *269*, 360–366. https://doi.org/10.1016/j.electacta.2018.02.156.

(34) Wang, Y.; Vaddiraju, S.; Gu, B.; Papadimitrakopoulos, F.; Burgess, D. J. Foreign Body Reaction to Implantable Biosensors: Effects of Tissue Trauma and Implant Size. *J. Diabetes Sci. Technol.* **2015**, *9* (5), 966–977. https://doi.org/10.1177/1932296815601869.

(35) Zebda, A.; Alcaraz, J. P.; Vadgama, P.; Shleev, S.; Minteer, S. D.; Boucher, F.; Cinquin, P.; Martin, D. K. Challenges for Successful Implantation of Biofuel Cells. *Bioelectrochemistry* **2018**, *124*, 57–72. https://doi.org/10.1016/j.bioelechem.2018.05.011.

(36) Liu, C.; Chen, Z.; Li, C. Z. Surface Engineering of Graphene-Enzyme Nanocomposites for Miniaturized Biofuel Cell. *IEEE Trans. Nanotechnol.* **2011**, *10* (1), 59–62. https://doi.org/10.1109/TNANO.2010.2050147.

(37) Kai, H.; Suda, W.; Yoshida, S.; Nishizawa, M. Organic Electrochromic Timer for Enzymatic Skin Patches. *Biosens. Bioelectron.* **2019**, *123* (July 2018), 108–113. https://doi.org/10.1016/j.bios.2018.07.013.

(38) Liu, L.; Kai, H.; Nagamine, K.; Ogawa, Y.; Nishizawa, M. Porous Polymer Microneedles with Interconnecting Microchannels for Rapid Fluid Transport. *RSC Adv.* **2016**, *6* (54), 48630–48635. https://doi.org/10.1039/c6ra07882f.

(39) Chiao, M. A Microfabricated PDMS Microbial Fuel Cell. *J.*

Microelectromechanical Syst. **2008**, *17* (6), 1329–1341.

(40) Chiao, M.; Lam, K. B.; Lin, L. Micromachined Microbial and Photosynthetic Fuel Cells. *J. Micromechanics Microengineering* **2006**, *16* (12), 2547.

(41) Han, S. C.; Choi, J. M.; Liu, G.; Kang, K. A Microscopic Shell Structure with Schwarz's D-Surface. *Sci. Rep.* **2017**, *7* (1), 1–8. https://doi.org/10.1038/s41598-017-13618-3.

(42) Panesar, A.; Abdi, M.; Hickman, D.; Ashcroft, I. Strategies for Functionally Graded Lattice Structures Derived Using Topology Optimisation for Additive Manufacturing. *Addit. Manuf.* **2018**, *19*, 81–94. https://doi.org/10.1016/j.addma.2017.11.008.

(43) Wadley, H. N. G.; Fleck, N. A.; Evans, A. G. Fabrication and Structural Performance of Periodic Cellular Metal Sandwich Structures. *Compos. Sci. Technol.* **2003**, *63* (16), 2331–2343.

(44) Lay, C. L.; Koh, C. S. L.; Lee, Y. H.; Phan-Quang, G. C.; Sim, H. Y. F.; Leong, S. X.; Han, X.; Phang, I. Y.; Ling, X. Y. Two-Photon-Assisted Polymerization and Reduction: Emerging Formulations and Applications. *ACS Appl. Mater. Interfaces* **2020**, *12* (9), 10061–10079. https://doi.org/10.1021/acsami.9b20911.

(45) Huang, Q.; Zhu, Y. Printing Conductive Nanomaterials for Flexible and Stretchable Electronics: A Review of Materials, Processes, and Applications. *Adv. Mater. Technol.* **2019**, *4* (5), 1800546.

(46)   Tan, H. W.; Choong, Y. Y. C.; Kuo, C. N.; Low, H. Y.; Chua, C. K. 3D Printed Electronics: Processes, Materials and Future Trends. *Prog. Mater. Sci.* **2022**, 100945.

(47)   Carranza, G. T.; Robles, U.; Valle, C. L.; Gutierrez, J. J.; Rumpf, R. C. Design and Hybrid Additive Manufacturing of 3-D/Volumetric Electrical Circuits. *IEEE Trans. Components, Packag. Manuf. Technol.* **2019**, *9* (6), 1176–1183.

(48)   Wu, S.-Y.; Yang, C.; Hsu, W.; Lin, L. 3D-Printed Microelectronics for Integrated Circuitry and Passive Wireless Sensors. *Microsystems Nanoeng.* **2015**, *1* (1), 1–9.

(49)   Zhang, W.; Liu, H.; Zhang, X.; Li, X.; Zhang, G.; Cao, P. 3D Printed Micro-electrochemical Energy Storage Devices: From Design to Integration. *Adv. Funct. Mater.* **2021**, *31* (40), 2104909.

(50)   Xu, Y.; Wu, X.; Guo, X.; Kong, B.; Zhang, M.; Qian, X.; Mi, S.; Sun, W. The Boom in 3D-Printed Sensor Technology. *Sensors* **2017**, *17* (5), 1166.

(51)   Choi, K. H.; Ahn, D. B.; Lee, S. Y. Current Status and Challenges in Printed Batteries: Toward Form Factor-Free, Monolithic Integrated Power Sources. *ACS Energy Lett.* **2018**, *3* (1), 220–236. https://doi.org/10.1021/acsenergylett.7b01086.

(52)   Van Osch, T. H. J.; Perelaer, J.; De Laat, A. W. M.; Schubert, U. S. Inkjet Printing of Narrow Conductive Tracks on Untreated Polymeric Substrates. *Adv. Mater.* **2008**, *20* (2), 343–345. https://doi.org/10.1002/adma.200701876.

(53) Liu, I. P.; Hung, W. N.; Teng, H.; Venkatesan, S.; Lin, J. C.; Lee, Y. L. High-Performance Printable Electrolytes for Dye-Sensitized Solar Cells. *J. Mater. Chem. A* **2017**, *5* (19), 9190–9197. https://doi.org/10.1039/c7ta01341h.

(54) Pei, Z.; Zhang, Q.; Li, Q.; Ji, C.; Liu, Y.; Yang, K.; Zhuo, K.; Zhang, W.; Sang, S. A Fully 3D Printed Electronic Skin with Bionic High Resolution and Air Permeable Porous Structure. *J. Colloid Interface Sci.* **2021**, *602*, 452–458.

(55) Mikolajek, M.; Reinheimer, T.; Bohn, N.; Kohler, C.; Hoffmann, M. J.; Binder, J. R. Fabrication and Characterization of Fully Inkjet Printed Capacitors Based on Ceramic/Polymer Composite Dielectrics on Flexible Substrates. *Sci. Rep.* **2019**, *9* (1), 1–13.

(56) Yang, Y.; Yuan, W.; Zhang, X.; Yuan, Y.; Wang, C.; Ye, Y.; Huang, Y.; Qiu, Z.; Tang, Y. Overview on the Applications of Three-Dimensional Printing for Rechargeable Lithium-Ion Batteries. *Appl. Energy* **2020**, *257*, 114002.

(57) Ramoni, M.; Shanmugam, R.; Thangapandian, N.; Vishnuvarthanan, M. Challenges in Additive Manufacturing for Metals and Alloys. In *Innovations in Additive Manufacturing*; Springer, 2022; pp 57–72.

(58) Zhou, L.; Ning, W.; Wu, C.; Zhang, D.; Wei, W.; Ma, J.; Li, C.; Chen, L. 3D-printed Microelectrodes with a Developed Conductive Network and Hierarchical Pores toward High Areal Capacity for Microbatteries. *Adv. Mater. Technol.* **2019**, *4* (2), 1800402.

(59) del-Mazo-Barbara, L.; Ginebra, M.-P. Rheological Characterisation of Ceramic

Inks for 3D Direct Ink Writing: A Review. *J. Eur. Ceram. Soc.* **2021**, *41* (16), 18–33.

(60)   Weems, A. C.; Pérez-Madrigal, M. M.; Arno, M. C.; Dove, A. P. 3D Printing for the Clinic: Examining Contemporary Polymeric Biomaterials and Their Clinical Utility. *Biomacromolecules* **2020**, *21* (3), 1037–1059.

(61)   Saleh, M. S.; Li, J.; Park, J.; Panat, R. 3D Printed Hierarchically-Porous Microlattice Electrode Materials for Exceptionally High Specific Capacity and Areal Capacity Lithium Ion Batteries. *Addit. Manuf.* **2018**, *23*, 70–78.

(62)   Chen, C.; Jiang, J.; He, W.; Lei, W.; Hao, Q.; Zhang, X. 3D Printed High-loading Lithium-sulfur Battery toward Wearable Energy Storage. *Adv. Funct. Mater.* **2020**, *30* (10), 1909469.

(63)   Secor, E. B.; Hersam, M. C. Emerging Carbon and Post-Carbon Nanomaterial Inks for Printed Electronics. *J. Phys. Chem. Lett.* **2015**, *6* (4), 620–626.

(64)   Chandrasekaran, S.; Yao, B.; Liu, T.; Xiao, W.; Song, Y.; Qian, F.; Zhu, C.; Duoss, E. B.; Spadaccini, C. M.; Li, Y. Direct Ink Writing of Organic and Carbon Aerogels. *Mater. Horizons* **2018**, *5* (6), 1166–1175.

(65)   Moyano, J. J.; Gómez-Gómez, A.; Pérez-Coll, D.; Belmonte, M.; Miranzo, P.; Osendi, M. I. Filament Printing of Graphene-Based Inks into Self-Supported 3D Architectures. *Carbon N. Y.* **2019**, *151*, 94–102.

(66)   Tsang, A. C. H.; Zhang, J.; Hui, K. N.; Hui, K. S.; Huang, H. Recent Development

and Applications of Advanced Materials via Direct Ink Writing. *Adv. Mater. Technol.* **2022**, 2101358.

(67)   Scordo, G.; Bertana, V.; Scaltrito, L.; Ferrero, S.; Cocuzza, M.; Marasso, S. L.; Romano, S.; Sesana, R.; Catania, F.; Pirri, C. F. A Novel Highly Electrically Conductive Composite Resin for Stereolithography. *Mater. Today Commun.* **2019**, *19* (November 2018), 12–17. https://doi.org/10.1016/j.mtcomm.2018.12.017.

(68)   Xu, C.; Quinn, B.; Lebel, L. L.; Therriault, D.; L'Espérance, G. Multi-Material Direct Ink Writing (DIW) for Complex 3D Metallic Structures with Removable Supports. *ACS Appl. Mater. Interfaces* **2019**, *11* (8), 8499–8506.

(69)   Wang, R.; Zhu, P.; Yang, W.; Gao, S.; Li, B.; Li, Q. Direct-Writing of 3D Periodic TiO2 Bio-Ceramic Scaffolds with a Sol-Gel Ink for in Vitro Cell Growth. *Mater. Des.* **2018**, *144*, 304–309.

(70)   Yap, C. Y.; Chua, C. K.; Dong, Z. L.; Liu, Z. H.; Zhang, D. Q.; Loh, L. E.; Sing, S. L. Review of Selective Laser Melting: Materials and Applications. *Appl. Phys. Rev.* **2015**, *2* (4), 41101.

(71)   Haeri, S. Optimisation of Blade Type Spreaders for Powder Bed Preparation in Additive Manufacturing Using DEM Simulations. *Powder Technol.* **2017**, *321*, 94–104.

(72)   Ventura, A. P.; Marvel, C. J.; Pawlikowski, G.; Bayes, M.; Watanabe, M.; Vinci, R. P.; Misiolek, W. Z. The Effect of Aging on the Microstructure of Selective Laser

Melted Cu-Ni-Si. *Metall. Mater. Trans. A* **2017**, *48* (12), 6070–6082.

(73)   Qu, S.; Ding, J.; Fu, J.; Fu, M.; Zhang, B.; Song, X. High-Precision Laser Powder Bed Fusion Processing of Pure Copper. *Addit. Manuf.* **2021**, *48*, 102417.

(74)   Silbernagel, C.; Gargalis, L.; Ashcroft, I.; Hague, R.; Galea, M.; Dickens, P. Electrical Resistivity of Pure Copper Processed by Medium-Powered Laser Powder Bed Fusion Additive Manufacturing for Use in Electromagnetic Applications. *Addit. Manuf.* **2019**, *29*, 100831.

(75)   Chin, S. Y.; Dikshit, V.; Meera Priyadarshini, B.; Zhang, Y. Powder-Based 3D Printing for the Fabrication of Device with Micro and Mesoscale Features. *Micromachines* **2020**, *11* (7), 658.

(76)   Zhang, H.; Choi, J. P.; Moon, S. K.; Ngo, T. H. A Hybrid Multi-Objective Optimization of Aerosol Jet Printing Process via Response Surface Methodology. *Addit. Manuf.* **2020**, *33*, 101096.

(77)   Rahman, M. T.; Panat, R. Aerosol Jet 3D Printing and High Temperature Characterization of Nickel Nanoparticle Films. *Manuf. Lett.* **2021**, *29*, 5–10.

(78)   Ligon, S. C.; Liska, R.; Stampfl, J.; Gurr, M.; Mülhaupt, R. Polymers for 3D Printing and Customized Additive Manufacturing. *Chem. Rev.* **2017**, *117* (15), 10212–10290. https://doi.org/10.1021/acs.chemrev.7b00074.

(79)   Ma, Z.-C.; Zhang, Y.-L.; Han, B.; Chen, Q.-D.; Sun, H.-B. Femtosecond-Laser Direct Writing of Metallic Micro/Nanostructures: From Fabrication Strategies to

Future Applications. *Small Methods* **2018**, *2* (7), 1700413. https://doi.org/10.1002/smtd.201700413.

(80) Naik, D. L.; Kiran, R. On Anisotropy, Strain Rate and Size Effects in Vat Photopolymerization Based Specimens. *Addit. Manuf.* **2018**, *23*, 181–196.

(81) Tétreault, N.; von Freymann, G.; Deubel, M.; Hermatschweiler, M.; Pérez-Willard, F.; John, S.; Wegener, M.; Ozin, G. A. New Route to Three-dimensional Photonic Bandgap Materials: Silicon Double Inversion of Polymer Templates. *Adv. Mater.* **2006**, *18* (4), 457–460.

(82) Lee, K.-S.; Kim, R. H.; Yang, D.-Y.; Park, S. H. Advances in 3D Nano/Microfabrication Using Two-Photon Initiated Polymerization. *Prog. Polym. Sci.* **2008**, *33* (6), 631–681.

(83) Hu, Q.; Sun, X. Z.; Parmenter, C. D. J.; Fay, M. W.; Smith, E. F.; Rance, G. A.; He, Y.; Zhang, F.; Liu, Y.; Irvine, D.; Tuck, C.; Hague, R.; Wildman, R. Additive Manufacture of Complex 3D Au-Containing Nanocomposites by Simultaneous Two-Photon Polymerisation and Photoreduction. *Sci. Rep.* **2017**, *7* (1), 1–9. https://doi.org/10.1038/s41598-017-17391-1.

(84) Cao, Y. Y.; Takeyasu, N.; Tanaka, T.; Duan, X. M.; Kawata, S. 3D Metallic Nanostructure Fabrication by Surfactant-Assisted Multiphoton-Induced Reduction. *Small* **2009**, *5* (10), 1144–1148. https://doi.org/10.1002/smll.200801179.

(85) Carlotti, M.; Mattoli, V. Functional Materials for Two-Photon Polymerization in

Microfabrication. *Small* **2019**, *15* (40), 1–22. https://doi.org/10.1002/smll.201902687.

(86) Zhang, J.; Xiao, P. 3D Printing of Photopolymers. *Polym. Chem.* **2018**, *9* (13), 1530–1540.

(87) Ligon-Auer, S. C.; Schwentenwein, M.; Gorsche, C.; Stampfl, J.; Liska, R. Toughening of Photo-Curable Polymer Networks: A Review. *Polym. Chem.* **2016**, *7* (2), 257–286.

(88) Chen, C.; Garber, L.; Smoak, M.; Fargason, C.; Scherr, T.; Blackburn, C.; Bacchus, S.; Lopez, M. J.; Pojman, J. A.; Del Piero, F. In Vitro and in Vivo Characterization of Pentaerythritol Triacrylate-Co-Trimethylolpropane Nanocomposite Scaffolds as Potential Bone Augments and Grafts. *Tissue Eng. Part A* **2015**, *21* (1–2), 320–331.

(89) Jayne, R. K.; Karakan, M. Ç.; Zhang, K.; Pierce, N.; Michas, C.; Bishop, D. J.; Chen, C. S.; Ekinci, K. L.; White, A. E. Direct Laser Writing for Cardiac Tissue Engineering: A Microfluidic Heart on a Chip with Integrated Transducers. *Lab Chip* **2021**, *21* (9), 1724–1737.

(90) Taormina, G.; Sciancalepore, C.; Messori, M.; Bondioli, F. 3D Printing Processes for Photocurable Polymeric Materials: Technologies, Materials, and Future Trends. *J. Appl. Biomater. Funct. Mater.* **2018**, *16* (3), 151–160.

(91) Voet, V. S. D.; Strating, T.; Schnelting, G. H. M.; Dijkstra, P.; Tietema, M.; Xu, J.; Woortman, A. J. J.; Loos, K.; Jager, J.; Folkersma, R. Biobased Acrylate

Photocurable Resin Formulation for Stereolithography 3D Printing. *ACS omega* **2018**, *3* (2), 1403–1408.

(92) Yee, D. W.; Schulz, M. D.; Grubbs, R. H.; Greer, J. R. Functionalized 3D Architected Materials via Thiol-Michael Addition and Two-Photon Lithography. *Adv. Mater.* **2017**, *29* (16). https://doi.org/10.1002/adma.201605293.

(93) Xiao, X.; Hao, C. Preparation of Waterborne Epoxy Acrylate/Silica Sol Hybrid Materials and Study of Their UV Curing Behavior. *Colloids Surfaces A Physicochem. Eng. Asp.* **2010**, *359* (1–3), 82–87.

(94) Parker, G. Encyclopedia of Materials: Science and Technology. **2001**.

(95) Deflorian, F.; Fedel, M. UV-Curable Organic Polymer Coatings for Corrosion Protection of Steel. In *Handbook of Smart Coatings for Materials Protection*; Elsevier, 2014; pp 530–559.

(96) Ikemura, K.; Endo, T. A Review of the Development of Radical Photopolymerization Initiators Used for Designing Light-Curing Dental Adhesives and Resin Composites. *Dent. Mater. J.* **2010**, 1009140075.

(97) Kiefer, P.; Hahn, V.; Nardi, M.; Yang, L.; Blasco, E.; Barner-Kowollik, C.; Wegener, M. Sensitive Photoresists for Rapid Multiphoton 3D Laser Micro-and Nanoprinting. *Adv. Opt. Mater.* **2020**, *8* (19), 2000895.

(98) Urrios, A.; Parra-Cabrera, C.; Bhattacharjee, N.; Gonzalez-Suarez, A. M.; Rigat-Brugarolas, L. G.; Nallapatti, U.; Samitier, J.; DeForest, C. A.; Posas, F.; Garcia-

Cordero, J. L. 3D-Printing of Transparent Bio-Microfluidic Devices in PEG-DA. *Lab Chip* **2016**, *16* (12), 2287–2294.

(99)   Kamoun, E. A.; Winkel, A.; Eisenburger, M.; Menzel, H. Carboxylated Camphorquinone as Visible-Light Photoinitiator for Biomedical Application: Synthesis, Characterization, and Application. *Arab. J. Chem.* **2016**, *9* (5), 745–754.

(100) Vaidyanathan, T. K.; Vaidyanathan, J.; Lizymol, P. P.; Ariya, S.; Krishnan, K. V. Study of Visible Light Activated Polymerization in BisGMA-TEGDMA Monomers with Type 1 and Type 2 Photoinitiators Using Raman Spectroscopy. *Dent. Mater.* **2017**, *33* (1), 1–11.

(101) Kuo, A. P.; Bhattacharjee, N.; Lee, Y.; Castro, K.; Kim, Y. T.; Folch, A. High-Precision Stereolithography of Biomicrofluidic Devices. *Adv. Mater. Technol.* **2019**, *4* (6), 1800395.

(102) Morizane, M.; Kawasaki, Y.; Miura, T.; Yagi, K.; Esumi, S.; Kitamura, Y.; Sendo, T. Photoinitiator-Initiated Estrogenic Activity in Human Breast Cancer Cell Line MCF-7. *J. Toxicol. Environ. Heal. Part A* **2015**, *78* (23–24), 1450–1460.

(103) Billiet, T.; Vandenhaute, M.; Schelfhout, J.; Van Vlierberghe, S.; Dubruel, P. A Review of Trends and Limitations in Hydrogel-Rapid Prototyping for Tissue Engineering. *Biomaterials* **2012**, *33* (26), 6020–6041.

(104) Reitsma, M.; Bovee, T. F. H.; Peijnenburg, A. A. C. M.; Hendriksen, P. J. M.; Hoogenboom, R. L. A. P.; Rijk, J. C. W. Endocrine-Disrupting Effects of

Thioxanthone Photoinitiators. *Toxicol. Sci.* **2013**, *132* (1), 64–74.

(105)   Chi, T.; Somers, P.; Wilcox, D. A.; Schuman, A. J.; Iyer, V.; Le, R.; Gengler, J.; Ferdinandus, M.; Liebig, C.; Pan, L. Tailored Thioxanthone-based Photoinitiators for Two-photon-controllable Polymerization and Nanolithographic Printing. *J. Polym. Sci. Part B Polym. Phys.* **2019**, *57* (21), 1462–1475.

(106)   Kowalska, A.; Sokolowski, J.; Bociong, K. The Photoinitiators Used in Resin Based Dental Composite—a Review and Future Perspectives. *Polymers (Basel).* **2021**, *13* (3), 470.

(107)   Salgado, V. E.; Borba, M. M.; Cavalcante, L. M.; de Moraes, R. R.; Schneider, L. F. Effect of Photoinitiator Combinations on Hardness, Depth of Cure, and Color of Model Resin Composites. *J. Esthet. Restor. Dent.* **2015**, *27*, S41–S48.

(108)   dos Reis Lima, C.; da Silva, D. B.; Vitti, R. P.; Miranda, M. E.; Brandt, W. C. Mechanical Properties of Experimental Resin Cements Containing Different Photoinitiators and Co-Initiators. *Clin. Cosmet. Investig. Dent.* **2019**, *11*, 285.

(109)   Zeng, B.; Cai, Z.; Lalevée, J.; Yang, Q.; Lai, H.; Xiao, P.; Liu, J.; Xing, F. Cytotoxic and Cytocompatible Comparison among Seven Photoinitiators-Triggered Polymers in Different Tissue Cells. *Toxicol. Vitr.* **2021**, *72*, 105103.

(110)   Dworak, C.; Koch, T.; Varga, F.; Liska, R. Photopolymerization of Biocompatible Phosphorus-containing Vinyl Esters and Vinyl Carbamates. *J. Polym. Sci. Part A Polym. Chem.* **2010**, *48* (13), 2916–2924.

(111) Schuster, M.; Turecek, C.; Varga, F.; Lichtenegger, H.; Stampfl, J.; Liska, R. 3D-Shaping of Biodegradable Photopolymers for Hard Tissue Replacement. *Appl. Surf. Sci.* **2007**, *254* (4), 1131–1134.

(112) Schuster, M.; Turecek, C.; Weigel, G.; Saf, R.; Stampfl, J.; Varga, F.; Liska, R. Gelatin-based Photopolymers for Bone Replacement Materials. *J. Polym. Sci. Part A Polym. Chem.* **2009**, *47* (24), 7078–7089.

(113) Warr, C.; Valdoz, J. C.; Bickham, B. P.; Knight, C. J.; Franks, N. A.; Chartrand, N.; Van Ry, P. M.; Christensen, K. A.; Nordin, G. P.; Cook, A. D. Biocompatible PEGDA Resin for 3D Printing. *ACS Appl. Bio Mater.* **2020**, *3* (4), 2239–2244. https://doi.org/10.1021/acsabm.0c00055.

(114) Grigoryan, B.; Paulsen, S. J.; Corbett, D. C.; Sazer, D. W.; Fortin, C. L.; Zaita, A. J.; Greenfield, P. T.; Calafat, N. J.; Gounley, J. P.; Ta, A. H.; Johansson, F.; Randles, A.; Rosenkrantz, J. E.; Louis-Rosenberg, J. D.; Galie, P. A.; Stevens, K. R.; Miller, J. S. Multivascular Networks and Functional Intravascular Topologies within Biocompatible Hydrogels. *Science (80-.).* **2019**, *364* (6439), 458–464. https://doi.org/10.1126/science.aav9750.

(115) Fonovich, T. M. Sudan Dyes: Are They Dangerous for Human Health? *Drug Chem. Toxicol.* **2013**, *36* (3), 343–352.

(116) Su, X.; Li, X.; Ong, C. Y. A.; Herng, T. S.; Wang, Y.; Peng, E.; Ding, J. Metallization of 3D Printed Polymers and Their Application as a Fully Functional Water-Splitting System. *Adv. Sci.* **2019**, *6* (6).

https://doi.org/10.1002/advs.201801670.

(117) Formanek, F.; Takeyasu, N.; Tanaka, T.; Chiyoda, K.; Ishikawa, A.; Kawata, S. Three-Dimensional Fabrication of Metallic Nanostructures over Large Areas by Two-Photon Polymerization. *Opt. Express* **2006**, *14* (2), 800. https://doi.org/10.1364/opex.14.000800.

(118) Formanek, F.; Takeyasu, N.; Tanaka, T.; Chiyoda, K.; Ishikawa, A.; Kawata, S. Selective Electroless Plating to Fabricate Complex Three-Dimensional Metallic Micro/Nanostructures. *Appl. Phys. Lett.* **2006**, *88* (8), 1–4. https://doi.org/10.1063/1.2178261.

(119) Huang, K. M.; Tsai, S. C.; Lee, Y. K.; Yuan, C. K.; Chang, Y. C.; Chiu, H. L.; Chung, T. T.; Liao, Y. C. Selective Metallic Coating of 3D-Printed Microstructures on Flexible Substrates. *RSC Adv.* **2017**, *7* (81), 51663–51669. https://doi.org/10.1039/c7ra11171a.

(120) Hossain, M. M.; Gu, M. Fabrication Methods of 3D Periodic Metallic Nano/Microstructures for Photonics Applications. *Laser Photonics Rev.* **2014**, *8* (2), 233–249. https://doi.org/10.1002/lpor.201300052.

(121) Kim, S. H.; Jackson, J. A.; Oakdale, J. S.; Forien, J. B.; Lenhardt, J. M.; Yoo, J. H.; Shin, S. J.; Lepró, X.; Moran, B. D.; Aracne-Ruddle, C. M.; Baumann, T. F.; Jones, O. S.; Biener, J. A Simple, Highly Efficient Route to Electroless Gold Plating on Complex 3D Printed Polyacrylate Plastics. *Chem. Commun.* **2018**, *54* (74), 10463–10466. https://doi.org/10.1039/C8CC05368E.

(122) Chen, Y. S.; Tal, A.; Torrance, D. B.; Kuebler, S. M. Fabrication and Characterization of Three-Dimensional Silver-Coated Polymeric Microstructures. *Adv. Funct. Mater.* **2006**, *16* (13), 1739–1744. https://doi.org/10.1002/adfm.200600394.

(123) Domenech, S. C.; Lima Jr, E.; Drago, V.; De Lima, J. C.; Borges Jr, N. G.; Avila, A. O. V; Soldi, V. Electroless Plating of Nickel–Phosphorous on Surface-Modified Poly (Ethylene Terephthalate) Films. *Appl. Surf. Sci.* **2003**, *220* (1–4), 238–250.

(124) Luan, B.; Yeung, M.; Wells, W.; Liu, X. Chemical Surface Preparation for Metallization of Stereolithography Polymers. *Appl. Surf. Sci.* **2000**, *156* (1–4), 26–38.

(125) Moraczewski, K.; Rytlewski, P.; Malinowski, R.; Tracz, A.; Żenkiewicz, M. Influence of DC Plasma Modification on the Selected Properties and the Geometrical Surface Structure of Polylactide Prior to Autocatalytic Metallization. *Mater. Chem. Phys.* **2015**, *153*, 135–144.

(126) Reznickova, A.; Kolska, Z.; Siegel, J.; Svorcik, V. Grafting of Gold Nanoparticles and Nanorods on Plasma-Treated Polymers by Thiols. *J. Mater. Sci.* **2012**, *47* (17), 6297–6304. https://doi.org/10.1007/s10853-012-6550-8.

(127) Yan, Y.; Rashad, M. I.; Teo, E. J.; Tanoto, H.; Teng, J.; Bettiol, A. A. Selective Electroless Silver Plating of Three Dimensional SU-8 Microstructures on Silicon for Metamaterials Applications. *Opt. Mater. Express* **2011**, *1* (8), 1548. https://doi.org/10.1364/ome.1.001548.

(128) Conrad, J. R.; Dodd, R. A.; Worzala, F. J.; Qiu, X. Plasma Source Ion Implantation: A New, Cost-Effective, Non-Line-of-Sight Technique for Ion Implantation of Materials. *Surf. Coatings Technol.* **1988**, *36* (3–4), 927–937. https://doi.org/10.1016/0257-8972(88)90033-3.

(129) Pyka, G.; Burakowski, A.; Kerckhofs, G.; Moesen, M.; Van Bael, S.; Schrooten, J.; Wevers, M. Surface Modification of Ti6Al4V Open Porous Structures Produced by Additive Manufacturing. *Adv. Eng. Mater.* **2012**, *14* (6), 363–370.

(130) Barry, J. J. A.; Silva, M. M. C. G.; Shakesheff, K. M.; Howdle, S. M.; Alexander, M. R. Using Plasma Deposits to Promote Cell Population of the Porous Interior of Three-dimensional Poly (D, L-lactic Acid) Tissue-engineering Scaffolds. *Adv. Funct. Mater.* **2005**, *15* (7), 1134–1140.

(131) Mandal, P.; Singha, N. K. Selective Atom Transfer Radical Polymerization of 1, 2, 3, 6-Tetrahydrobenzyl Methacrylate (THBMA) and Demonstration of Thiol–Ene Addition Reaction in the Pendant Cycloalkenyl Functional Group. *Eur. Polym. J.* **2015**, *67*, 21–30.

(132) Shahzadi, L.; Maya, F.; Breadmore, M. C.; Thickett, S. C. Functional Materials for DLP-SLA 3D Printing Using Thiol–Acrylate Chemistry: Resin Design and Postprint Applications. *ACS Appl. Polym. Mater.* **2022**, *4* (5), 3896–3907.

(133) Simon, D. M.; Charkhkar, H.; St. John, C.; Rajendran, S.; Kang, T.; Reit, R.; Arreaga-Salas, D.; McHail, D. G.; Knaack, G. L.; Sloan, A. Design and Demonstration of an Intracortical Probe Technology with Tunable Modulus. *J.*

Biomed. Mater. Res. Part A **2017**, *105* (1), 159–168.

(134) Ecker, M.; Danda, V.; Shoffstall, A. J.; Mahmood, S. F.; Joshi-Imre, A.; Frewin, C. L.; Ware, T. H.; Capadona, J. R.; Pancrazio, J. J.; Voit, W. E. Sterilization of Thiol-ene/Acrylate Based Shape Memory Polymers for Biomedical Applications. *Macromol. Mater. Eng.* **2017**, *302* (2), 1600331.

(135) Ware, T.; Simon, D.; Hearon, K.; Kang, T. H.; Maitland, D. J.; Voit, W. Thiol-C Lick Chemistries for Responsive Neural Interfaces. *Macromol. Biosci.* **2013**, *13* (12), 1640–1647.

(136) González-Vidal, N.; Martinez De Ilarduya, A.; Muñoz-Guerra, S. Poly (Ethylene-co-1, 4-cyclohexylenedimethylene Terephthalate) Copolyesters Obtained by Ring Opening Polymerization. *J. Polym. Sci. Part A Polym. Chem.* **2009**, *47* (22), 5954–5966.

(137) Quick, A. S.; Fischer, J.; Richter, B.; Pauloehrl, T.; Trouillet, V.; Wegener, M.; Barner-Kowollik, C. Preparation of Reactive Three-Dimensional Microstructures via Direct Laser Writing and Thiol-Ene Chemistry. *Macromol. Rapid Commun.* **2013**, *34* (4), 335–340. https://doi.org/10.1002/marc.201200796.

(138) Cramer, N. B.; Couch, C. L.; Schreck, K. M.; Carioscia, J. A.; Boulden, J. E.; Stansbury, J. W.; Bowman, C. N. Investigation of Thiol-Ene and Thiol-Ene–Methacrylate Based Resins as Dental Restorative Materials. *Dent. Mater.* **2010**, *26* (1), 21–28.

(139) Singamaneni, S.; Kharlampieva, E.; Jang, J. H.; McConney, M. E.; Jiang, H.;

Bunning, T. J.; Thomas, E. L.; Tsukruk, V. V. Metalized Porous Interference Lithographic Microstructures via Biofunctionalization. *Adv. Mater.* **2010**, *22* (12), 1369–1373. https://doi.org/10.1002/adma.200902893.

(140) Jackman, R. J.; Brittain, S. T.; Adams, A.; Wu, H.; Prentiss, M. G.; Whitesides, S.; Whitesides, G. M. Three-Dimensional Metallic Microstructures Fabricated by Soft Lithography and Microelectrodeposition. *Langmuir* **1999**, *15* (3), 826–834. https://doi.org/10.1021/la980857y.

(141) Gobet, J.; Cardot, F.; Bergqvist, J.; Rudolf, F. Electrodeposition of 3D Microstructures on Silicon. *J. Micromechanics Microengineering* **1993**, *3* (3), 123–130. https://doi.org/10.1088/0960-1317/3/3/007.

(142) Liu, Y.; Xu, Y.; Avila, R.; Liu, C.; Xie, Z.; Wang, L.; Yu, X. 3D Printed Microstructures for Flexible Electronic Devices. *Nanotechnology* **2019**, *30* (41). https://doi.org/10.1088/1361-6528/ab2d5d.

(143) Shacham-Diamand, Y.; Osaka, T.; Okinaka, Y.; Sugiyama, A.; Dubin, V. 30 Years of Electroless Plating for Semiconductor and Polymer Micro-Systems. *Microelectron. Eng.* **2015**, *132*, 35–45. https://doi.org/10.1016/j.mee.2014.09.003.

(144) Wang, W.-K.; Sun, Z.-B.; Zheng, M.-L.; Dong, X.-Z.; Zhao, Z.-S.; Duan, X.-M. Magnetic Nickel–Phosphorus/Polymer Composite and Remotely Driven Three-Dimensional Micromachine Fabricated by Nanoplating and Two-Photon Polymerization. *J. Phys. Chem. C* **2011**, *115* (22), 11275–11281.

(145) Ma, Z.-C.; Zhang, Y.-L.; Han, B.; Chen, Q.-D.; Sun, H.-B. Femtosecond-Laser Direct Writing of Metallic Micro/Nanostructures: From Fabrication Strategies to Future Applications. *Small Methods* **2018**, *2* (7), 1700413. https://doi.org/10.1002/smtd.201700413.

(146) Fu, Y.; Liu, L.; Zhang, L.; Wang, W. Highly Conductive One-Dimensional Nanofibers: Silvered Electrospun Silica Nanofibers via Poly(Dopamine) Functionalization. *ACS Appl. Mater. Interfaces* **2014**, *6* (7), 5105–5112. https://doi.org/10.1021/am5002663.

(147) Ee, Y. C.; Chen, Z.; Chan, L.; See, A. K. H.; Law, S. B.; Tee, K. C.; Zeng, K. Y.; Shen, L. Effect of Processing Parameters on Electroless Cu Seed Layer Properties. *Thin Solid Films* **2004**, *462–463* (SPEC. ISS.), 197–201. https://doi.org/10.1016/j.tsf.2004.05.018.

(148) Javidjam, A.; Hekmatshoar, M. H.; Hedayatifar, L.; Abad, S. N. K. Effect of Surface Roughness on Electrical Conductivity and Hardness of Silver Plated Copper. *Mater. Res. Express* **2019**, *6* (3). https://doi.org/10.1088/2053-1591/aaf4c5.

(149) Tanaka, T.; Ishikawa, A.; Kawata, S. Two-Photon-Induced Reduction of Metal Ions for Fabricating Three-Dimensional Electrically Conductive Metallic Microstructure. *Appl. Phys. Lett.* **2006**, *88* (8), 1–4. https://doi.org/10.1063/1.2177636.

(150) Do, J. S.; Shieh, R. Y. Electrochemical Nitrogen Dioxide Gas Sensor Based on Solid Polymeric Electrolyte. *Sensors Actuators, B Chem.* **1996**, *37* (1–2), 19–26.

https://doi.org/10.1016/S0925-4005(97)80068-8.

(151) Tang, J.; Ou, Q.; Zhou, H.; Qi, L.; Man, S. Seed-Mediated Electroless Deposition of Gold Nanoparticles for Highly Uniform and Efficient SERS Enhancement. *Nanomaterials* **2019**, *9* (2). https://doi.org/10.3390/nano9020185.

(152) Sau, T. K.; Pal, A.; Jana, N. R.; Wang, Z. L.; Pal, T. Size Controlled Synthesis of Gold Nanoparticles Using Photochemically Prepared Seed Particles. *J. Nanoparticle Res.* **2001**, *3* (4), 257–261. https://doi.org/10.1023/A:1017567225071.

(153) Monsalve, K.; Mazurenko, I.; Lalaoui, N.; Le Goff, A.; Holzinger, M.; Infossi, P.; Nitsche, S.; Lojou, J.-Y.; Giudici-Orticoni, M.-T.; Cosnier, S. A H2/O2 Enzymatic Fuel Cell as a Sustainable Power for a Wireless Device. *Electrochem. commun.* **2015**, *60*, 216–220.

(154) Ó Conghaile, P.; Falk, M.; MacAodha, D.; Yakovleva, M. E.; Gonaus, C.; Peterbauer, C. K.; Gorton, L.; Shleev, S.; Leech, D. Fully Enzymatic Membraneless Glucose| Oxygen Fuel Cell That Provides 0.275 MA Cm−2 in 5 MM Glucose, Operates in Human Physiological Solutions, and Powers Transmission of Sensing Data. *Anal. Chem.* **2016**, *88* (4), 2156–2163.

(155) Mazurenko, eI; De Poulpiquet, A.; Lojou, E. Recent Developments in High Surface Area Bioelectrodes for Enzymatic Fuel Cells. *Curr. Opin. Electrochem.* **2017**, *5* (1), 74–84.

(156) Miyake, T.; Haneda, K.; Nagai, N.; Yatagawa, Y.; Onami, H.; Yoshino, S.; Abe, T.;

Nishizawa, M. Enzymatic Biofuel Cells Designed for Direct Power Generation from Biofluids in Living Organisms. *Energy Environ. Sci.* **2011**, *4* (12), 5008–5012.

(157) Du, J.; Wang, S.; You, H.; Zhao, X. Understanding the Toxicity of Carbon Nanotubes in the Environment Is Crucial to the Control of Nanomaterials in Producing and Processing and the Assessment of Health Risk for Human: A Review. *Environ. Toxicol. Pharmacol.* **2013**, *36* (2), 451–462.

(158) Orecchioni, M.; Ménard-Moyon, C.; Delogu, L. G.; Bianco, A. Graphene and the Immune System: Challenges and Potentiality. *Adv. Drug Deliv. Rev.* **2016**, *105*, 163–175.

(159) Flexer, V.; Brun, N.; Backov, R.; Mano, N. Designing Highly Efficient Enzyme-Based Carbonaceous Foams Electrodes for Biofuel Cells. *Energy Environ. Sci.* **2010**, *3* (9), 1302–1306.

(160) Mazurenko, I.; Monsalve, K.; Infossi, P.; Giudici-Orticoni, M.-T.; Topin, F.; Mano, N.; Lojou, E. Impact of Substrate Diffusion and Enzyme Distribution in 3D-Porous Electrodes: A Combined Electrochemical and Modelling Study of a Thermostable H 2/O 2 Enzymatic Fuel Cell. *Energy Environ. Sci.* **2017**, *10* (9), 1966–1982.

(161) Mazurenko, I.; Clément, R.; Byrne-Kodjabachian, D.; De Poulpiquet, A.; Tsujimura, S.; Lojou, E. Pore Size Effect of MgO-Templated Carbon on Enzymatic H2 Oxidation by the Hyperthermophilic Hydrogenase from Aquifex Aeolicus. *J. Electroanal. Chem.* **2018**, *812*, 221–226.

(162) Yu, Y.; Chen, Z.; He, S.; Zhang, B.; Li, X.; Yao, M. Direct Electron Transfer of Glucose Oxidase and Biosensing for Glucose Based on PDDA-Capped Gold Nanoparticle Modified Graphene/Multi-Walled Carbon Nanotubes Electrode. *Biosens. Bioelectron.* **2014**, *52*, 147–152.

(163) Bartlett, P. N.; Al-Lolage, F. A. There Is No Evidence to Support Literature Claims of Direct Electron Transfer (DET) for Native Glucose Oxidase (GOx) at Carbon Nanotubes or Graphene. *J. Electroanal. Chem.* **2018**, *819*, 26–37.

(164) Nasar, A.; Perveen, R. Applications of Enzymatic Biofuel Cells in Bioelectronic Devices – A Review. *Int. J. Hydrogen Energy* **2019**, *44* (29), 15287–15312. https://doi.org/10.1016/j.ijhydene.2019.04.182.

(165) Mayo, S. L.; Ellis, W. R.; Crutchley, R. J.; Gray, H. B. Long-Range Electron Transfer in Heme Proteins. *Science (80-.).* **1986**, *233* (4767), 948–952.

(166) Page, C. C.; Moser, C. C.; Chen, X.; Dutton, P. L. Natural Engineering Principles of Electron Tunnelling in Biological Oxidation–Reduction. *Nature* **1999**, *402* (6757), 47–52.

(167) Wang, J. Electrochemical Glucose Biosensors. *Chem. Rev.* **2008**, *108* (2), 814–825.

(168) Mano, N.; de Poulpiquet, A. O2 Reduction in Enzymatic Biofuel Cells. *Chem. Rev.* **2017**, *118* (5), 2392–2468.

(169) Stines-Chaumeil, C.; Roussarie, E.; Mano, N. The Nature of the Rate-Limiting

Step of Blue Multicopper Oxidases: Homogeneous Studies versus Heterogeneous. *Biochim. open* **2017**, *4*, 36–40.

(170) Yeoman, C. J.; Han, Y.; Dodd, D.; Schroeder, C. M.; Mackie, R. I.; Cann, I. K. O. Thermostable Enzymes as Biocatalysts in the Biofuel Industry. *Adv. Appl. Microbiol.* **2010**, *70*, 1–55.

(171) Salditt, P. Trends in Medical Device Design and Manufacturing. *Med. Electron. Symp.* **2004**, 186.

(172) Beilke, M. C.; Klotzbach, T. L.; Treu, B. L.; Sokic-Lazic, D.; Wildrick, J.; Amend, E. R.; Gebhart, L. M.; Arechederra, R. L.; Germain, M. N.; Moehlenbrock, M. J.; Sudhanshu; Minteer, S. D. Enzymatic Biofuel Cells. *Micro Fuel Cells* **2009**, 179–241. https://doi.org/10.1016/B978-0-12-374713-6.00005-6.

(173) Ahmad, R.; Sardar, M. Enzyme Immobilization: An Overview on Nanoparticles as Immobilization Matrix. *Biochem. Anal. Biochem.* **2015**, *4* (2), 1.

(174) Mateo, C.; Palomo, J. M.; Fernandez-Lorente, G.; Guisan, J. M.; Fernandez-Lafuente, R. Improvement of Enzyme Activity, Stability and Selectivity via Immobilization Techniques. *Enzyme Microb. Technol.* **2007**, *40* (6), 1451–1463.

(175) Du Toit, H.; Di Lorenzo, M. Glucose Oxidase Directly Immobilized onto Highly Porous Gold Electrodes for Sensing and Fuel Cell Applications. *Electrochim. Acta* **2014**, *138*, 86–92.

(176) Moses Phiri, M.; Wingrove Mulder, D.; Mason, S.; Christiaan Vorster, B. Facile

Immobilization of Glucose Oxidase onto Gold Nanostars with Enhanced Binding Affinity and Optimal Function. *R. Soc. open Sci.* **2019**, *6* (5), 190205.

(177) Kim, H.; Kwon, J.-Y. Enzyme Immobilization on Metal Oxide Semiconductors Exploiting Amine Functionalized Layer. *RSC Adv.* **2017**, *7* (32), 19656–19661.

(178) Casero, E.; Darder, M.; Pariente, F.; Lorenzo, E.; Martín-Benito, J.; Vázquez, L. Thiol-Functionalized Gold Surfaces as a Strategy to Induce Order in Membrane-Bound Enzyme Immobilization. *Nano Lett.* **2002**, *2* (6), 577–582.

(179) Santos, J. C. S. dos; Barbosa, O.; Ortiz, C.; Berenguer-Murcia, A.; Rodrigues, R. C.; Fernandez-Lafuente, R. Importance of the Support Properties for Immobilization or Purification of Enzymes. *ChemCatChem* **2015**, *7* (16), 2413–2432.

(180) Arana-Peña, S.; Carballares, D.; Cortés Corberan, V.; Fernandez-Lafuente, R. Multi-Combilipases: Co-Immobilizing Lipases with Very Different Stabilities Combining Immobilization via Interfacial Activation and Ion Exchange. The Reuse of the Most Stable Co-Immobilized Enzymes after Inactivation of the Least Stable Ones. *Catalysts* **2020**, *10* (10), 1207.

(181) Lee, W.-H.; Loo, C.-Y.; Van, K. L.; Zavgorodniy, A. V; Rohanizadeh, R. Modulating Protein Adsorption onto Hydroxyapatite Particles Using Different Amino Acid Treatments. *J. R. Soc. Interface* **2012**, *9* (70), 918–927.

(182) Hanefeld, U.; Gardossi, L.; Magner, E. Understanding Enzyme Immobilisation. *Chem. Soc. Rev.* **2009**, *38* (2), 453–468.

(183) Imam, H. T.; Marr, P. C.; Marr, A. C. Enzyme Entrapment, Biocatalyst Immobilization without Covalent Attachment. *Green Chem.* **2021**, *23* (14), 4980–5005.

(184) Liu, C.; Alwarappan, S.; Chen, Z.; Kong, X.; Li, C.-Z. Membraneless Enzymatic Biofuel Cells Based on Graphene Nanosheets. *Biosens. Bioelectron.* **2010**, *25* (7), 1829–1833.

(185) Kim, M. H.; An, S.; Won, K.; Kim, H. J.; Lee, S. H. Entrapment of Enzymes into Cellulose–Biopolymer Composite Hydrogel Beads Using Biocompatible Ionic Liquid. *J. Mol. Catal. B Enzym.* **2012**, *75*, 68–72.

(186) Gregoriadis, G.; Leathwood, P. D.; Ryman, B. E. Enzyme Entrapment in Liposomes. *FEBS Lett.* **1971**, *14* (2), 95–99.

(187) Nawaz, M. A.; Karim, A.; Bibi, Z.; Rehman, H. U.; Aman, A.; Hussain, D.; Ullah, M.; Qader, S. A. U. Maltase Entrapment Approach as an Efficient Alternative to Increase the Stability and Recycling Efficiency of Free Enzyme within Agarose Matrix. *J. Taiwan Inst. Chem. Eng.* **2016**, *64*, 31–38.

(188) Van Nguyen, K.; Minteer, S. D. Investigating DNA Hydrogels as a New Biomaterial for Enzyme Immobilization in Biobatteries. *Chem. Commun.* **2015**, *51* (66), 13071–13073.

(189) Zebda, A.; Gondran, C.; Le Goff, A.; Holzinger, M.; Cinquin, P.; Cosnier, S. Mediatorless High-Power Glucose Biofuel Cells Based on Compressed Carbon Nanotube-Enzyme Electrodes. *Nat. Commun.* **2011**, *2* (1), 1–6.

(190) El Ichi, S.; Zebda, A.; Laaroussi, A.; Reverdy-Bruas, N.; Chaussy, D.; Belgacem, M. N.; Cinquin, P.; Martin, D. K. Chitosan Improves Stability of Carbon Nanotube Biocathodes for Glucose Biofuel Cells. *Chem. Commun.* **2014**, *50* (93), 14535–14538.

(191) Barbosa, O.; Ortiz, C.; Berenguer-Murcia, Á.; Torres, R.; Rodrigues, R. C.; Fernandez-Lafuente, R. Glutaraldehyde in Bio-Catalysts Design: A Useful Crosslinker and a Versatile Tool in Enzyme Immobilization. *Rsc Adv.* **2014**, *4* (4), 1583–1600.

(192) Xia, H.; Kitazumi, Y.; Shirai, O.; Kano, K. Direct Electron Transfer-Type Bioelectrocatalysis of Peroxidase at Mesoporous Carbon Electrodes and Its Application for Glucose Determination Based on Bienzyme System. *Anal. Sci.* **2017**, *33* (7), 839–844.

(193) Bahar, T. Preparation of a Ferrocene Mediated Bioanode for Biofuel Cells by MWCNTs, Polyethylenimine and Glutaraldehyde: Glucose Oxidase Immobilization and Characterization. *Asia-Pacific J. Chem. Eng.* **2016**, *11* (6), 981–988.

(194) Huang, X.; Zhang, L.; Zhang, Z.; Guo, S.; Shang, H.; Li, Y.; Liu, J. Biosensors and Bioelectronics Wearable Biofuel Cells Based on the Classi Fi Cation of Enzyme for High Power Outputs and Lifetimes. *Biosens. Bioelectron.* **2019**, *124–125* (September 2018), 40–52. https://doi.org/10.1016/j.bios.2018.09.086.

(195) Eş, I.; Vieira, J. D. G.; Amaral, A. C. Principles, Techniques, and Applications of

Biocatalyst Immobilization for Industrial Application. *Appl. Microbiol. Biotechnol.* **2015**, *99* (5), 2065–2082.

(196) Sang, B. I.; Kwon, Y.; Kim, K. W.; Gu, M. B.; Kim, J.; Kim, J. H.; Kim, S. H.; Jia, H.; Hsiao, E.; Zhao, X.; Kim, B. C.; Oh, M.-K.; Nair, S.; Ahn, H.-K.; Kim, B.-S.; Lee, H.-J.; Ha, S.; Wang, P. Highly Stable Enzyme Precipitate Coatings and Their Electrochemical Applications. *Biosens. Bioelectron.* **2010**, *26* (5), 1980–1986. https://doi.org/10.1016/j.bios.2010.08.068.

(197) Gutierrez-Sanchez, C.; Pita, M.; Vaz-Dominguez, C.; Shleev, S.; De Lacey, A. L. Gold Nanoparticles as Electronic Bridges for Laccase-Based Biocathodes. *J. Am. Chem. Soc.* **2012**, *134* (41), 17212–17220.

(198) Gutierrez-Sanchez, C.; Ciaccafava, A.; Blanchard, P. Y.; Monsalve, K.; Giudici-Orticoni, M. T.; Lecomte, S.; Lojou, E. Efficiency of Enzymatic O2 Reduction by Myrothecium Verrucaria Bilirubin Oxidase Probed by Surface Plasmon Resonance, PMIRRAS, and Electrochemistry. *Acs Catal.* **2016**, *6* (8), 5482–5492.

(199) Vaz-Dominguez, C.; Campuzano, S.; Rüdiger, O.; Pita, M.; Gorbacheva, M.; Shleev, S.; Fernandez, V. M.; De Lacey, A. L. Laccase Electrode for Direct Electrocatalytic Reduction of O2 to H2O with High-Operational Stability and Resistance to Chloride Inhibition. *Biosens. Bioelectron.* **2008**, *24* (4), 531–537.

(200) Hou, C.; Yang, D.; Liang, B.; Liu, A. Enhanced Performance of a Glucose/O2 Biofuel Cell Assembled with Laccase-Covalently Immobilized Three-Dimensional Macroporous Gold Film-Based Biocathode and Bacterial Surface

Displayed Glucose Dehydrogenase-Based Bioanode. *Anal. Chem.* **2014**, *86* (12), 6057–6063.

(201) Shim, J.; Kim, G.-Y.; Moon, S.-H. Covalent Co-Immobilization of Glucose Oxidase and Ferrocenedicarboxylic Acid for an Enzymatic Biofuel Cell. *J. Electroanal. Chem.* **2011**, *653* (1–2), 14–20.

(202) Di Bari, C.; Shleev, S.; De Lacey, A. L.; Pita, M. Laccase-Modified Gold Nanorods for Electrocatalytic Reduction of Oxygen. *Bioelectrochemistry* **2016**, *107*, 30–36.

(203) Karawdeniya, B. I.; Damry, A. M.; Murugappan, K.; Manjunath, S.; Bandara, Y. M. N. D. Y.; Jackson, C. J.; Tricoli, A.; Neshev, D. Surface Functionalization and Texturing of Optical Metasurfaces for Sensing Applications. *Chem. Rev.* **2022**.

(204) Climent, V.; Zhang, J.; Friis, E. P.; Østergaard, L. H.; Ulstrup, J. Voltammetry and Single-Molecule in Situ Scanning Tunneling Microscopy of Laccases and Bilirubin Oxidase in Electrocatalytic Dioxygen Reduction on Au (111) Single-Crystal Electrodes. *J. Phys. Chem. C* **2012**, *116* (1), 1232–1243.

(205) Cheung, D. T.; Nimni, M. E. Mechanism of Crosslinking of Proteins by Glutaraldehyde I: Reaction with Model Compounds. *Connect. Tissue Res.* **1982**, *10* (2), 187–199.

(206) Li, Z.; Gao, F.; Gu, Z. Vertically Aligned Pt Nanowire Array/Au Nanoparticle Hybrid Structure as Highly Sensitive Amperometric Biosensors. *Sensors Actuators B Chem.* **2017**, *243*, 1092–1101.

(207) Rodrigues, R. C.; Berenguer-Murcia, Á.; Carballares, D.; Morellon-Sterling, R.; Fernandez-Lafuente, R. Stabilization of Enzymes via Immobilization: Multipoint Covalent Attachment and Other Stabilization Strategies. *Biotechnol. Adv.* **2021**, *52*, 107821.

(208) Gombin, D.; Klamár, G.; Krisch, J.; Polyák, B.; Szajáni, B. Effects of Carbodiimides Coupling Agents on the Properties of Immobilized Glucoamylases. *ACTA Biol.* **1999**, 69.

(209) Hashida, S.; Imagawa, M.; Inoue, S.; Ruan, K. H.; Ishikawa, E. More Useful Maleimide Compounds for the Conjugation of Fab'to Horseradish Peroxidase through Thiol Groups in the Hinge. *J. Appl. Biochem.* **1984**, *6* (1–2), 56–63.

(210) Song, J.; Lei, T.; Yang, Y.; Wu, N.; Su, P.; Yang, Y. Attachment of Enzymes to Hydrophilic Magnetic Nanoparticles through DNA-Directed Immobilization with Enhanced Stability and Catalytic Activity. *New J. Chem.* **2018**, *42* (11), 8458–8468.

(211) Hitaishi, V. P.; Clement, R.; Bourassin, N.; Baaden, M.; De Poulpiquet, A.; Sacquin-Mora, S.; Ciaccafava, A.; Lojou, E. Controlling Redox Enzyme Orientation at Planar Electrodes. *Catalysts* **2018**, *8* (5), 192.

(212) Holland, J. T.; Lau, C.; Brozik, S.; Atanassov, P.; Banta, S. Engineering of Glucose Oxidase for Direct Electron Transfer via Site-Specific Gold Nanoparticle Conjugation. *J. Am. Chem. Soc.* **2011**, *133* (48), 19262–19265.

(213) Zhang, L.; Vilà, N.; Klein, T.; Kohring, G.-W.; Mazurenko, I.; Walcarius, A.;

Etienne, M. Immobilization of Cysteine-Tagged Proteins on Electrode Surfaces by Thiol–Ene Click Chemistry. *ACS Appl. Mater. Interfaces* **2016**, *8* (27), 17591–17598.

(214) Lee, J. M.; Park, H. K.; Jung, Y.; Kim, J. K.; Jung, S. O.; Chung, B. H. Direct Immobilization of Protein G Variants with Various Numbers of Cysteine Residues on a Gold Surface. *Anal. Chem.* **2007**, *79* (7), 2680–2687.

(215) Li, Y.; Zhang, J.; Huang, X.; Wang, T. Construction and Direct Electrochemistry of Orientation Controlled Laccase Electrode. *Biochem. Biophys. Res. Commun.* **2014**, *446* (1), 201–205.

(216) Al-Lolage, F. A.; Meneghello, M.; Ma, S.; Ludwig, R.; Bartlett, P. N. A Flexible Method for the Stable, Covalent Immobilization of Enzymes at Electrode Surfaces. *ChemElectroChem* **2017**, *4* (6), 1528–1534.

(217) Gwenin, C. D.; Kalaji, M.; Williams, P. A.; Jones, R. M. The Orientationally Controlled Assembly of Genetically Modified Enzymes in an Amperometric Biosensor. *Biosens. Bioelectron.* **2007**, *22* (12), 2869–2875.

(218) Kovačević, G.; Ostafe, R.; Fischer, R.; Prodanović, R. Influence of Methionine Residue Position on Oxidative Stability of Glucose Oxidase from Aspergillus Niger. *Biochem. Eng. J.* **2019**, *146*, 143–149.

(219) Rüdiger, O.; Abad, J. M.; Hatchikian, E. C.; Fernandez, V. M.; De Lacey, A. L. Oriented Immobilization of Desulfovibrio Gi Gas Hydrogenase onto Carbon Electrodes by Covalent Bonds for Nonmediated Oxidation of H2. *J. Am. Chem.*

Soc. **2005**, *127* (46), 16008–16009.

(220) Olejnik, P.; Palys, B.; Kowalczyk, A.; Nowicka, A. M. Orientation of Laccase on Charged Surfaces. Mediatorless Oxygen Reduction on Amino-and Carboxyl-Ended Ethylphenyl Groups. *J. Phys. Chem. C* **2012**, *116* (49), 25911–25918.

(221) Martinez-Ortiz, J.; Flores, R.; Vazquez-Duhalt, R. Molecular Design of Laccase Cathode for Direct Electron Transfer in a Biofuel Cell. *Biosens. Bioelectron.* **2011**, *26* (5), 2626–2631.

(222) Rüdiger, O.; Gutiérrez-Sánchez, C.; Olea, D.; Pereira, I. A. C.; Vélez, M.; Fernández, V. M.; De Lacey, A. L. Enzymatic Anodes for Hydrogen Fuel Cells Based on Covalent Attachment of Ni-Fe Hydrogenases and Direct Electron Transfer to SAM-Modified Gold Electrodes. *Electroanal. An Int. J. Devoted to Fundam. Pract. Asp. Electroanal.* **2010**, *22* (7-8), 776–783.

(223) Dubois, L. H.; Nuzzo, R. G. Synthesis, Structure, and Properties of Model Organic Surfaces. *Annu. Rev. Phys. Chem.* **1992**, *43* (1), 437–463.

(224) Schwartz, D. K. Mechanisms and Kinetics of Self-Assembled Monolayer Formation. *Annu. Rev. Phys. Chem.* **2001**, *52* (1), 107–137.

(225) Santos, L.; Ghilane, J.; Lacroix, J. C. Formation of Mixed Organic Layers by Stepwise Electrochemical Reduction of Diazonium Compounds. *J. Am. Chem. Soc.* **2012**, *134* (12), 5476–5479.

(226) Hetemi, D.; Pinson, J. Surface Functionalisation of Polymers. *Chem. Soc. Rev.*

2017, *46* (19), 5701–5713.

(227)   Pita, M.; Gutierrez-Sanchez, C.; Olea, D.; Velez, M.; Garcia-Diego, C.; Shleev, S.; Fernandez, V. M.; De Lacey, A. L. High Redox Potential Cathode Based on Laccase Covalently Attached to Gold Electrode. *J. Phys. Chem. C* **2011**, *115* (27), 13420–13428.

(228)   Bouden, S.; Pinson, J.; Vautrin-Ul, C. Electrografting of Diazonium Salts: A Kinetics Study. *Electrochem. commun.* **2017**, *81*, 120–123.

(229)   dos Santos, J. C. S.; Rueda, N.; Torres, R.; Barbosa, O.; Goncalves, L. R. B.; Fernandez-Lafuente, R. Evaluation of Divinylsulfone Activated Agarose to Immobilize Lipases and to Tune Their Catalytic Properties. *Process Biochem.* **2015**, *50* (6), 918–927.

(230)   dos Santos, J. C. S.; Rueda, N.; Barbosa, O.; Fernández-Sánchez, J. F.; Medina-Castillo, A. L.; Ramón-Márquez, T.; Arias-Martos, M. C.; Millán-Linares, M. C.; Pedroche, J.; del Mar Yust, M. Characterization of Supports Activated with Divinyl Sulfone as a Tool to Immobilize and Stabilize Enzymes via Multipoint Covalent Attachment. Application to Chymotrypsin. *RSC Adv.* **2015**, *5* (27), 20639–20649.

(231)   de Andrades, D.; Graebin, N. G.; Kadowaki, M. K.; Ayub, M. A. Z.; Fernandez-Lafuente, R.; Rodrigues, R. C. Immobilization and Stabilization of Different β-Glucosidases Using the Glutaraldehyde Chemistry: Optimal Protocol Depends on the Enzyme. *Int. J. Biol. Macromol.* **2019**, *129*, 672–678.

(232) Tiago, L.; Peirce, S.; Rueda, N.; Marzocchella, A.; Gonçalves, L. R. B.; Rocha, M. V. P.; Fernandez-Lafuente, R. Ion Exchange of β-Galactosidase: The Effect of the Immobilization PH on Enzyme Stability. *Process Biochem.* **2016**, *51* (7), 875–880.

(233) Kwon, C. H.; Ko, Y.; Shin, D.; Kwon, M.; Park, J.; Bae, W. K.; Lee, S. W.; Cho, J. High-Power Hybrid Biofuel Cells Using Layer-by-Layer Assembled Glucose Oxidase-Coated Metallic Cotton Fibers. *Nat. Commun.* **2018**, *9* (1), 1–11.

(234) Betancor, L.; López-Gallego, F.; Hidalgo, A.; Alonso-Morales, N.; Dellamora-Ortiz, G.; Guisán, J. M.; Fernández-Lafuente, R. Preparation of a Very Stable Immobilized Biocatalyst of Glucose Oxidase from Aspergillus Niger. *J. Biotechnol.* **2006**, *121* (2), 284–289.

(235) Kolb, C.; Lindemann, N.; Wolter, H.; Sextl, G. 3D-Printing of Highly Translucent ORMOCER®-Based Resin Using Light Absorber for High Dimensional Accuracy. *J. Appl. Polym. Sci.* **2021**, *138* (3), 49691. https://doi.org/10.1002/app.49691.

(236) Jia, J.; Wang, B.; Wu, A.; Cheng, G.; Li, Z.; Dong, S. A Method to Construct a Third-Generation Horseradish Peroxidase Biosensor: Self-Assembling Gold Nanoparticles to Three-Dimensional Sol-Gel Network. *Anal. Chem.* **2002**, *74* (9), 2217–2223. https://doi.org/10.1021/ac011116w.

(237) Fernandez-Lafuente, R.; Rodriguez, V.; Guisán, J. M. The Coimmobilization of D-Amino Acid Oxidase and Catalase Enables the Quantitative Transformation of D-Amino Acids (D-Phenylalanine) into α-Keto Acids (Phenylpyruvic Acid). *Enzyme Microb. Technol.* **1998**, *23* (1–2), 28–33.

(238) Vieira, M. F.; Vieira, A. M. S.; Zanin, G. M.; Tardioli, P. W.; Mateo, C.; Guisán, J. M. β-Glucosidase Immobilized and Stabilized on Agarose Matrix Functionalized with Distinct Reactive Groups. *J. Mol. Catal. B Enzym.* **2011**, *69* (1–2), 47–53.

(239) Ramadan, A. A.; Gould, R. D.; Ashour, A. On the Van Der Pauw Method of Resistivity Measurements. *Thin Solid Films* **1994**, *239* (2), 272–275. https://doi.org/10.1016/0040-6090(94)90863-X.

(240) Shan, C.; Chen, F.; Yang, Q.; Li, Y.; Bian, H.; Yong, J.; Hou, X. High-Level Integration of Three-Dimensional Microcoils Array in Fused Silica. *Opt. Lett.* **2015**, *40* (17), 4050–4053. https://doi.org/10.1364/OL.40.004050.

(241) Espera, A. H.; Dizon, J. R. C.; Chen, Q.; Advincula, R. C. 3D-Printing and Advanced Manufacturing for Electronics. *Prog. Addit. Manuf.* **2019**, 1–23.

(242) Macdonald, E.; Salas, R.; Espalin, D.; Perez, M.; Aguilera, E.; Muse, D.; Wicker, R. B. 3D Printing for the Rapid Prototyping of Structural Electronics. *IEEE access* **2014**, *2*, 234–242.

(243) Kundu, A.; McCoy, L.; Azim, N.; Nguyen, H.; Didier, C. M.; Ausaf, T.; Sharma, A. D.; Curley, J. L.; Moore, M. J.; Rajaraman, S. Fabrication and Characterization of 3D Printed, 3D Microelectrode Arrays for Interfacing with a Peripheral Nerve-on-a-Chip. *ACS Biomater. Sci. Eng.* **2020**. https://doi.org/10.1021/acsbiomaterials.0c01184.

(244) Kim, N.-Y.; Adhikari, K. K.; Dhakal, R.; Chuluunbaatar, Z.; Wang, C.; Kim, E.-S. Rapid, Sensitive and Reusable Detection of Glucose by a Robust Radiofrequency

Integrated Passive Device Biosensor Chip. *Sci. Rep.* **2015**, *5* (1), 1–9.

(245) Kamath, R. R.; Madou, M. J. Three-Dimensional Carbon Interdigitated Electrode Arrays for Redox-Amplification. *Anal. Chem.* **2014**, *86* (6), 2963–2971.

(246) Hemanth, S.; Caviglia, C.; Keller, S. S. Suspended 3D Pyrolytic Carbon Microelectrodes for Electrochemistry. *Carbon N. Y.* **2017**, *121*, 226–234.

(247) Hu, X.-B.; Liu, Y.-L.; Wang, W.-J.; Zhang, H.-W.; Qin, Y.; Guo, S.; Zhang, X.-W.; Fu, L.; Huang, W.-H. Biomimetic Graphene-Based 3D Scaffold for Long-Term Cell Culture and Real-Time Electrochemical Monitoring. *Anal. Chem.* **2018**, *90* (2), 1136–1141.

(248) Santoro, F.; Schnitker, J.; Panaitov, G.; Offenhäusser, A. On Chip Guidance and Recording of Cardiomyocytes with 3D Mushroom-Shaped Electrodes. *Nano Lett.* **2013**, *13* (11), 5379–5384.

(249) Amato, L.; Heiskanen, A.; Caviglia, C.; Shah, F.; Zór, K.; Skolimowski, M.; Madou, M.; Gammelgaard, L.; Hansen, R.; Seiz, E. G. Pyrolysed 3D-Carbon Scaffolds Induce Spontaneous Differentiation of Human Neural Stem Cells and Facilitate Real-Time Dopamine Detection. *Adv. Funct. Mater.* **2014**, *24* (44), 7042–7052.

(250) Andresen, K. Ø.; Hansen, M.; Matschuk, M.; Jepsen, S. T.; Sørensen, H. S.; Utko, P.; Selmeczi, D.; Hansen, T. S.; Larsen, N. B.; Rozlosnik, N. Injection Molded Chips with Integrated Conducting Polymer Electrodes for Electroporation of Cells. *J. Micromechanics Microengineering* **2010**, *20* (5), 55010.

(251) Matteucci, M.; Heiskanen, A.; Zór, K.; Emnéus, J.; Taboryski, R. Comparison of Ultrasonic Welding and Thermal Bonding for the Integration of Thin Film Metal Electrodes in Injection Molded Polymeric Lab-on-Chip Systems for Electrochemistry. *Sensors* **2016**, *16* (11), 1795.

(252) Voldman, J.; Gray, M. L.; Toner, M.; Schmidt, M. A. A Microfabrication-Based Dynamic Array Cytometer. *Anal. Chem.* **2002**, *74* (16), 3984–3990.

(253) Lee, S.; Ahn, J. H.; Seo, J.-M.; Chung, H.; Cho, D.-I. Electrical Characterization of 3D Au Microelectrodes for Use in Retinal Prostheses. *Sensors* **2015**, *15* (6), 14345–14355.

(254) Kim, S.; Park, J.; Kang, K.; Park, C.-O.; Park, I. Direct Metal Micropatterning on Needle-Type Structures towards Bioimpedance and Chemical Sensing Applications. *J. Micromechanics Microengineering* **2014**, *25* (1), 15002.

(255) Siegel, A. C.; Bruzewicz, D. A.; Weibel, D. B.; Whitesides, G. M. Microsolidics: Fabrication of Three-dimensional Metallic Microstructures in Poly (Dimethylsiloxane). *Adv. Mater.* **2007**, *19* (5), 727–733.

(256) Helú, M. A. B.; Liu, L. Fused Deposition Modeling (FDM) Based 3D Printing of Microelectrodes and Multi-Electrode Probes. *Electrochim. Acta* **2021**, *365*, 137279. https://doi.org/10.1016/j.electacta.2020.137279.

(257) Wei, H.; Li, K.; Liu, W. G.; Meng, H.; Zhang, P. X.; Yan, C. Y. 3D Printing of Free-Standing Stretchable Electrodes with Tunable Structure and Stretchability. *Adv. Eng. Mater.* **2017**, *19* (11), 1700341.

(258) Nagarajan, B.; Hu, Z.; Song, X.; Zhai, W.; Wei, J. Development of Micro Selective Laser Melting: The State of the Art and Future Perspectives. *Engineering*. Elsevier Ltd August 1, 2019, pp 702–720. https://doi.org/10.1016/j.eng.2019.07.002.

(259) Grob, L.; Yamamoto, H.; Zips, S.; Rinklin, P.; Hirano-Iwata, A.; Wolfrum, B. Printed 3D Electrode Arrays with Micrometer-Scale Lateral Resolution for Extracellular Recording of Action Potentials. *Adv. Mater. Technol.* **2020**, *5* (3), 1900517. https://doi.org/10.1002/admt.201900517.

(260) Blasco, E.; Müller, J.; Müller, P.; Trouillet, V.; Schön, M.; Scherer, T.; Barner-Kowollik, C.; Wegener, M. Fabrication of Conductive 3D Gold-Containing Microstructures via Direct Laser Writing. *Adv. Mater.* **2016**, *28* (18), 3592–3595. https://doi.org/10.1002/adma.201506126.

(261) Kim, S. H.; Yeon, Y. K.; Lee, J. M.; Chao, J. R.; Lee, Y. J.; Seo, Y. B.; Sultan, M. T.; Lee, O. J.; Lee, J. S.; Yoon, S. Il; Hong, I. S.; Khang, G.; Lee, S. J.; Yoo, J. J.; Park, C. H. Precisely Printable and Biocompatible Silk Fibroin Bioink for Digital Light Processing 3D Printing. *Nat. Commun.* **2018**, *9* (1), 1–14. https://doi.org/10.1038/s41467-018-03759-y.

(262) Koffler, J.; Zhu, W.; Qu, X.; Platoshyn, O.; Dulin, J. N.; Brock, J.; Graham, L.; Lu, P.; Sakamoto, J.; Marsala, M.; Chen, S.; Tuszynski, M. H. Biomimetic 3D-Printed Scaffolds for Spinal Cord Injury Repair. *Nat. Med.* **2019**, *25* (2), 263–269. https://doi.org/10.1038/s41591-018-0296-z.

(263) Chen, X.; Liu, W.; Dong, B.; Lee, J.; Ware, H. O. T.; Zhang, H. F.; Sun, C. High-Speed 3D Printing of Millimeter-Size Customized Aspheric Imaging Lenses with Sub 7 Nm Surface Roughness. *Adv. Mater.* **2018**, *30* (18), 1705683. https://doi.org/10.1002/adma.201705683.

(264) Cui, Y.; Phang, I. Y.; Lee, Y. H.; Lee, M. R.; Zhang, Q.; Ling, X. Y. Multiplex Plasmonic Anti-Counterfeiting Security Labels Based on Surface-Enhanced Raman Scattering. *Chem. Commun.* **2015**, *51* (25), 5363–5366. https://doi.org/10.1039/c4cc08596e.

(265) Yang, Y.; Chen, Z.; Song, X.; Zhang, Z.; Zhang, J.; Shung, K. K.; Zhou, Q.; Chen, Y. Biomimetic Anisotropic Reinforcement Architectures by Electrically Assisted Nanocomposite 3D Printing. *Adv. Mater.* **2017**, *29* (11), 1605750. https://doi.org/10.1002/adma.201605750.

(266) Martin, J. J.; Fiore, B. E.; Erb, R. M. Designing Bioinspired Composite Reinforcement Architectures via 3D Magnetic Printing. *Nat. Commun.* **2015**, *6* (1), 1–7. https://doi.org/10.1038/ncomms9641.

(267) Yang, Y.; Li, X.; Chu, M.; Sun, H.; Jin, J.; Yu, K.; Wang, Q.; Zhou, Q.; Chen, Y. Electrically Assisted 3D Printing of Nacre-Inspired Structures with Self-Sensing Capability. *Sci. Adv.* **2019**, *5* (4), eaau9490. https://doi.org/10.1126/sciadv.aau9490.

(268) Mu, Q.; Wang, L.; Dunn, C. K.; Kuang, X.; Duan, F.; Zhang, Z.; Qi, H. J.; Wang, T. Digital Light Processing 3D Printing of Conductive Complex Structures. *Addit.*

Manuf. **2017**, *18*, 74–83. https://doi.org/10.1016/j.addma.2017.08.011.

(269) Ni, R.; Qian, B.; Liu, C.; Liu, X.; Qiu, J. A Cross-Linking Strategy with Moderated Pre-Polymerization of Resin for Stereolithography. *RSC Adv.* **2018**, *8* (52), 29583–29588.

(270) Schuster, M.; Turecek, C.; Mateos, A.; Stampfl, J.; Liska, R.; Varga, F. Evaluation of Biocompatible Photopolymers II: Further Reactive Diluents. *Monatshefte fur Chemie* **2007**, *138* (4), 261–268. https://doi.org/10.1007/s00706-007-0609-2.

(271) Heller Christian A4 - Schwentenwein, Martin A4 - Russmüller, Günter A4 - Koch, Thomas A4 - Moser, Doris A4 - Schopper, Christian A4 - Varga, Franz A4 - Stampfl, Jürgen A4 - Liska, Robert, C. A.-H. Vinylcarbonates and Vinylcarbamates: Biocompatible Monomers for Radical Photopolymerization Part A Polymer Chemistry. *J. Polym. Sci.* **2011**, *v. 49* (3), 650-661–2011 v.49 no.3. https://doi.org/10.1002/pola.24476.

(272) Ferracane, J. L.; Greener, E. H. The Effect of Resin Formulation on the Degree of Conversion and Mechanical Properties of Dental Restorative Resins. *J. Biomed. Mater. Res.* **1986**, *20* (1), 121–131.

(273) Jan, C. M.; Nomura, Y.; Urabe, H.; Okazaki, M.; Shintani, H. The Relationship between Leachability of Polymerization Initiator and Degree of Conversion of Visible Light-cured Resin. *J. Biomed. Mater. Res. An Off. J. Soc. Biomater. Japanese Soc. Biomater. Aust. Soc. Biomater.* **2001**, *58* (1), 42–46.

(274) Liu, X.; Zhou, X.; Li, Y.; Zheng, Z. Surface-Grafted Polymer-Assisted Electroless

Deposition of Metals for Flexible and Stretchable Electronics. *Chem. - An Asian J.* **2012**, *7* (5), 862–870. https://doi.org/10.1002/asia.201100946.

(275) Shin, I.; Park, M. 3D Printed Conductive Patterns Based on Laser Irradiation. *Phys. Status Solidi Appl. Mater. Sci.* **2017**, *214* (7). https://doi.org/10.1002/pssa.201600943.

(276) Tang, X.; Cao, M.; Bi, C.; Yan, L.; Zhang, B. Research on a New Surface Activation Process for Electroless Plating on ABS Plastic. *Mater. Lett.* **2008**, *62* (6–7), 1089–1091. https://doi.org/10.1016/j.matlet.2007.07.055.

(277) Mondin, G.; Lohe, M. R.; Wisser, F. M.; Grothe, J.; Mohamed-Noriega, N.; Leifert, A.; Dörfler, S.; Bachmatiuk, A.; Rümmeli, M. H.; Kaskel, S. Electroless Copper Deposition on (3-Mercaptopropyl)Triethoxysilane-Coated Silica and Alumina Nanoparticles. *Electrochim. Acta* **2013**, *114*, 521–526. https://doi.org/10.1016/j.electacta.2013.10.055.

(278) Matinlinna, J. P.; Lung, C. Y. K.; Tsoi, J. K. H. Silane Adhesion Mechanism in Dental Applications and Surface Treatments: A Review. *Dent. Mater.* **2018**, *34* (1), 13–28. https://doi.org/10.1016/j.dental.2017.09.002.

(279) Stumpf, M.; Travitzky, N.; Greil, P.; Fey, T. Sol-Gel Infiltration of Complex Cellular Indirect 3D Printed Alumina. *J. Eur. Ceram. Soc.* **2018**, *38* (10), 3603–3609.

(280) Xiao, S.; Xu, P.; Peng, Q.; Chen, J.; Huang, J.; Wang, F.; Noor, N. Layer-by-Layer Assembly of Polyelectrolyte Multilayer onto PET Fabric for Highly Tunable Dyeing with Water Soluble Dyestuffs. *Polymers (Basel).* **2017**, *9* (12), 735.

(281) Wang, J.; Li, J.; Wei, J. Adsorption Characteristics of Noble Metal Ions onto Modified Straw Bearing Amine and Thiol Groups. *J. Mater. Chem. A* **2015**, *3* (35), 18163–18170. https://doi.org/10.1039/c5ta05371d.

(282) Kang, T.; Park, Y.; Yi, J. Highly Selective Adsorption of Pt2+ and Pd2+ Using Thiol-Functionalized Mesoporous Silica. *Ind. Eng. Chem. Res.* **2004**, *43* (6), 1478–1484. https://doi.org/10.1021/ie030590k.

(283) Petkov, N.; Stock, N.; Bein, T. Gold Electroless Reduction in Nanosized Channels of Thiol-Modified SBA-15 Material. *J. Phys. Chem. B* **2005**, *109* (21), 10737–10743. https://doi.org/10.1021/jp050429i.

(284) Pita, M.; Abad, J. M.; Vaz-Dominguez, C.; Briones, C.; Mateo-Martí, E.; Martín-Gago, J. A.; del Puerto Morales, M.; Fernández, V. M. Synthesis of Cobalt Ferrite Core/Metallic Shell Nanoparticles for the Development of a Specific PNA/DNA Biosensor. *J. Colloid Interface Sci.* **2008**, *321* (2), 484–492.

(285) Kelly, C. N.; Francovich, J.; Julmi, S.; Safranski, D.; Guldberg, R. E.; Maier, H. J.; Gall, K. Fatigue Behavior of As-Built Selective Laser Melted Titanium Scaffolds with Sheet-Based Gyroid Microarchitecture for Bone Tissue Engineering. *Acta Biomater.* **2019**, *94*, 610–626.

(286) Alizadeh-Osgouei, M.; Li, Y.; Vahid, A.; Ataee, A.; Wen, C. High Strength Porous PLA Gyroid Scaffolds Manufactured via Fused Deposition Modeling for Tissue-Engineering Applications. *Smart Mater. Med.* **2021**, *2*, 15–25.

(287) Nguyen, B. D.; Han, S. C.; Jung, Y. C.; Kang, K. Design of the P-Surfaced Shellular,

an Ultra-Low Density Material with Micro-Architecture. *Comput. Mater. Sci.* **2017**, *139*, 162–178.

(288) Philips'Gloeilampenfabrieken, O. A Method of Measuring Specific Resistivity and Hall Effect of Discs of Arbitrary Shape. *Philips Res. Rep* **1958**, *13* (1), 1–9.

(289) Hsu, C.-W.; Wang, W.-Y.; Wang, K.-T.; Chen, H.-A.; Wei, T.-C. Manipulating the Adhesion of Electroless Nickel-Phosphorus Film on Silicon Wafers by Silane Compound Modification and Rapid Thermal Annealing. *Sci. Rep.* **2017**, *7* (1), 1–11.

(290) Angelova, P.; Solel, E.; Parvari, G.; Turchanin, A.; Botoshansky, M.; Gölzhäuser, A.; Keinan, E. Chemisorbed Monolayers of Corannulene Penta-Thioethers on Gold. *Langmuir* **2013**, *29* (7), 2217–2223.

(291) Peters, S.; Peredkov, S.; Neeb, M.; Eberhardt, W.; Al-Hada, M. Size-Dependent XPS Spectra of Small Supported Au-Clusters. *Surf. Sci.* **2013**, *608*, 129–134. https://doi.org/10.1016/j.susc.2012.09.024.

(292) Courjean, O.; Mano, N. Recombinant Glucose Oxidase from Penicillium Amagasakiense for Efficient Bioelectrochemical Applications in Physiological Conditions. *J. Biotechnol.* **2011**, *151* (1), 122–129.

(293) Bankar, S. B.; Bule, M. V; Singhal, R. S.; Ananthanarayan, L. Glucose Oxidase—an Overview. *Biotechnol. Adv.* **2009**, *27* (4), 489–501.

(294) Viswanathan, S.; Li, P.; Choi, W.; Filipek, S.; Balasubramaniam, T. A.;

Renugopalakrishnan, V. Protein–Carbon Nanotube Sensors: Single Platform Integrated Micro Clinical Lab for Monitoring Blood Analytes. In *Methods in Enzymology*; Elsevier, 2012; Vol. 509, pp 165–194.

(295) Zucca, P.; Fernandez-Lafuente, R.; Sanjust, E. Agarose and Its Derivatives as Supports for Enzyme Immobilization. *Molecules* **2016**, *21* (11), 1577.

(296) Mateo, C.; Fernández-Lorente, G.; Abian, O.; Fernández-Lafuente, R.; Guisán, J. M. Multifunctional Epoxy Supports: A New Tool to Improve the Covalent Immobilization of Proteins. The Promotion of Physical Adsorptions of Proteins on the Supports before Their Covalent Linkage. *Biomacromolecules* **2000**, *1* (4), 739–745.

(297) Mateo, C.; Abian, O.; Fernández-Lorente, G.; Pedroche, J.; Fernández-Lafuente, R.; Guisan, J. M. Epoxy Sepabeads: A Novel Epoxy Support for Stabilization of Industrial Enzymes via Very Intense Multipoint Covalent Attachment. *Biotechnol. Prog.* **2002**, *18* (3), 629–634.

(298) López-Gallego, F.; Fernandez-Lorente, G.; Rocha-Martin, J.; Bolivar, J. M.; Mateo, C.; Guisan, J. M. Stabilization of Enzymes by Multipoint Covalent Immobilization on Supports Activated with Glyoxyl Groups. In *Immobilization of Enzymes and Cells*; Springer, 2013; pp 59–71.

(299) Guisán, J. Aldehyde-Agarose Gels as Activated Supports for Immobilization-Stabilization of Enzymes. *Enzyme Microb. Technol.* **1988**, *10* (6), 375–382.

(300) Fernandez-Lafuente, R.; Rosell, C. M.; Rodriguez, V.; Guisan, J. M. Strategies for

Enzyme Stabilization by Intramolecular Crosslinking with Bifunctional Reagents. *Enzyme Microb. Technol.* **1995**, *17* (6), 517–523.

(301) López-Gallego, F.; Betancor, L.; Mateo, C.; Hidalgo, A.; Alonso-Morales, N.; Dellamora-Ortiz, G.; Guisán, J. M.; Fernández-Lafuente, R. Enzyme Stabilization by Glutaraldehyde Crosslinking of Adsorbed Proteins on Aminated Supports. *J. Biotechnol.* **2005**, *119* (1), 70–75.

(302) Magnan, E.; Catarino, I.; Paolucci-Jeanjean, D.; Preziosi-Belloy, L.; Belleville, M. P. Immobilization of Lipase on a Ceramic Membrane: Activity and Stability. *J. Memb. Sci.* **2004**, *241* (1), 161–166.

(303) Tukel, S. S.; Alptekin, O. Immobilization and Kinetics of Catalase onto Magnesium Silicate. *Process Biochem.* **2004**, *39* (12), 2149–2155.

(304) Batool, R.; Kazmi, S. A. R.; Khurshid, S.; Saeed, M.; Ali, S.; Adnan, A.; Altaf, F.; Hameed, A.; Batool, F.; Fatima, N. Postharvest Shelf Life Enhancement of Peach Fruit Treated with Glucose Oxidase Immobilized on ZnO Nanoparticles. *Food Chem.* **2022**, *366*, 130591.

(305) Yabuki, S.; Mizutani, F.; Sato, Y.; Hirata, Y. Immobilization of Polyglutamate-Glucose Oxidase onto a Cysteamine-Modified Gold Electrode. *Sensors Actuators B Chem.* **2003**, *91* (1–3), 187–190.

(306) Bezbradica, D. I.; Mateo, C.; Guisan, J. M. Novel Support for Enzyme Immobilization Prepared by Chemical Activation with Cysteine and Glutaraldehyde. *J. Mol. Catal. B Enzym.* **2014**, *102*, 218–224.

(307) Mateo, C.; Abian, O.; Bernedo, M.; Cuenca, E.; Fuentes, M.; Fernandez-Lorente, G.; Palomo, J. M.; Grazu, V.; Pessela, B. C. C.; Giacomini, C. Some Special Features of Glyoxyl Supports to Immobilize Proteins. *Enzyme Microb. Technol.* **2005**, *37* (4), 456–462.

(308) Ait Braham, S.; Hussain, F.; Morellon-Sterling, R.; Kamal, S.; Kornecki, J. F.; Barbosa, O.; Kati, D. E.; Fernandez-Lafuente, R. Cooperativity of Covalent Attachment and Ion Exchange on Alcalase Immobilization Using Glutaraldehyde Chemistry: Enzyme Stabilization and Improved Proteolytic Activity. *Biotechnol. Prog.* **2019**, *35* (2), e2768.

(309) Bolivar, J. M.; Woodley, J. M.; Fernandez-Lafuente, R. Is Enzyme Immobilization a Mature Discipline? Some Critical Considerations to Capitalize on the Benefits of Immobilization. *Chem. Soc. Rev.*

(310) Fuentes, M.; Batalla, P.; Grazu, V.; Pessela, B. C. C.; Mateo, C.; Montes, T.; Hermoso, J. A.; Guisan, J. M.; Fernandez-Lafuente, R. Mixed Ion Exchange Supports as Useful Ion Exchangers for Protein Purification: Purification of Penicillin G Acylase from Escherichia Coli. *Biomacromolecules* **2007**, *8* (2), 703–707.

(311) Xiao, X.; McGourty, K. D.; Magner, E. Enzymatic Biofuel Cells for Self-Powered, Controlled Drug Release. *J. Am. Chem. Soc.* **2020**, *142* (26), 11602–11609.

(312) Xiao, X.; Conghaile, P. Ó.; Leech, D.; Ludwig, R.; Magner, E. A Symmetric Supercapacitor/Biofuel Cell Hybrid Device Based on Enzyme-Modified

Nanoporous Gold: An Autonomous Pulse Generator. *Biosens. Bioelectron.* **2017**, *90*, 96–102.

(313) Xiao, X.; Conghaile, P. Ó.; Leech, D.; Ludwig, R.; Magner, E. An Oxygen-Independent and Membrane-Less Glucose Biobattery/Supercapacitor Hybrid Device. *Biosens. Bioelectron.* **2017**, *98*, 421–427.

(314) Xiao, X.; Ulstrup, J.; Li, H.; Zhang, J.; Si, P. Nanoporous Gold Assembly of Glucose Oxidase for Electrochemical Biosensing. *Electrochim. Acta* **2014**, *130*, 559–567.

(315) Khatami, S. H.; Vakili, O.; Ahmadi, N.; Soltani Fard, E.; Mousavi, P.; Khalvati, B.; Maleksabet, A.; Savardashtaki, A.; Taheri-Anganeh, M.; Movahedpour, A. Glucose Oxidase: Applications, Sources, and Recombinant Production. *Biotechnol. Appl. Biochem.* **2021**.

(316) Bauer, J. A.; Zámocká, M.; Majtán, J.; Bauerová-Hlinková, V. Glucose Oxidase, an Enzyme "Ferrari": Its Structure, Function, Production and Properties in the Light of Various Industrial and Biotechnological Applications. *Biomolecules* **2022**, *12* (3), 472.

(317) Kornecki, J. F.; Carballares, D.; Tardioli, P. W.; Rodrigues, R. C.; Berenguer-Murcia, Á.; Alcántara, A. R.; Fernandez-Lafuente, R. Enzyme Production of D-Gluconic Acid and Glucose Oxidase: Successful Tales of Cascade Reactions. *Catal. Sci. Technol.* **2020**, *10* (17), 5740–5771.

(318) Chung, Y.; Ahn, Y.; Kim, D.-H.; Kwon, Y. Amide Group Anchored Glucose Oxidase Based Anodic Catalysts for High Performance Enzymatic Biofuel Cell. *J. Power*

Sources **2017**, *337*, 152–158.

(319)   Reuillard, B.; Le Goff, A.; Agnes, C.; Holzinger, M.; Zebda, A.; Gondran, C.; Elouarzaki, K.; Cosnier, S. High Power Enzymatic Biofuel Cell Based on Naphthoquinone-Mediated Oxidation of Glucose by Glucose Oxidase in a Carbon Nanotube 3D Matrix. *Phys. Chem. Chem. Phys.* **2013**, *15* (14), 4892–4896.

(320)   Kawai, T.; Saito, K.; Lee, W. Protein Binding to Polymer Brush, Based on Ion-Exchange, Hydrophobic, and Affinity Interactions. *J. Chromatogr. B* **2003**, *790* (1–2), 131–142.

(321)   Dziennik, S. R.; Belcher, E. B.; Barker, G. A.; DeBergalis, M. J.; Fernandez, S. E.; Lenhoff, A. M. Nondiffusive Mechanisms Enhance Protein Uptake Rates in Ion Exchange Particles. *Proc. Natl. Acad. Sci.* **2003**, *100* (2), 420–425.

(322)   Levison, P. R. Large-Scale Ion-Exchange Column Chromatography of Proteins: Comparison of Different Formats. *J. Chromatogr. B* **2003**, *790* (1–2), 17–33.

(323)   Vazquez-Ortega, P. G.; Alcaraz-Fructuoso, M. T.; Rojas-Contreras, J. A.; López-Miranda, J.; Fernandez-Lafuente, R. Stabilization of Dimeric β-Glucosidase from Aspergillus Niger via Glutaraldehyde Immobilization under Different Conditions. *Enzyme Microb. Technol.* **2018**, *110*, 38–45.

(324)   Lv, P.; Feng, Q.; Wang, Q.; Li, G.; Li, D.; Wei, Q. Biosynthesis of Bacterial Cellulose/Carboxylic Multi-Walled Carbon Nanotubes for Enzymatic Biofuel Cell Application. *Materials (Basel).* **2016**, *9* (3), 183.

(325) Shakeel, N.; Ahamed, M. I.; Ahmed, A.; Rahman, M. M.; Asiri, A. M. Functionalized Magnetic Nanoparticle-Reduced Graphene Oxide Nanocomposite for Enzymatic Biofuel Cell Applications. *Int. J. Hydrogen Energy* **2019**, *44* (52), 28294–28304.

(326) Hu, Q.; Rance, G. A.; Trindade, G. F.; Pervan, D.; Jiang, L.; Foerster, A.; Turyanska, L.; Tuck, C.; Irvine, D. J.; Hague, R. The Influence of Printing Parameters on Multi-Material Two-Photon Polymerisation Based Micro Additive Manufacturing. *Addit. Manuf.* **2022**, *51*, 102575.

(327) Ferracane, J. L.; Greener, E. H. Fourier Transform Infrared Analysis of Degree of Polymerization in Unfilled Resins—Methods Comparison. *J. Dent. Res.* **1984**, *63* (8), 1093–1095.

(328) Shin, W. S.; Li, X. F.; Schwartz, B.; Wunder, S. L.; Baran, G. R. Determination of the Degree of Cure of Dental Resins Using Raman and FT-Raman Spectroscopy. *Dent. Mater.* **1993**, *9* (5), 317–324.

(329) Kabatc, J.; Ortyl, J.; Kostrzewska, K. New Kinetic and Mechanistic Aspects of Photosensitization of Iodonium Salts in Photopolymerization of Acrylates. *Rsc Adv.* **2017**, *7* (66), 41619–41629.

(330) Sudagar, J.; Tamilarasan, R.; Sanjith, U.; Rajendran, R.; Kumar, R. Electroless Deposition of Nanolayered Metallic Coatings. *Nanoscaled Film. Layers* **2017**, 28–50.

(331) Ali, A.; Jamal, R.; Abdiryim, T. One-Pot Self-Assembly Preparation of Thiol-

Functionalized Poly (3, 4-Ethylenedioxythiophene) Hollow Nanosphere/Au Composites, and Their Electrocatalytic Properties. *RSC Adv.* **2021**, *11* (53), 33425–33430.

(332) Muench, F. Electroless Plating of Metal Nanomaterials. *ChemElectroChem* **2021**, *8* (16), 2993–3012.

(333) Lović, J.; Stevanović, S.; Nikolić, N. D.; Petrović, S.; Vuković, D.; Prlainović, N.; Mijin, D.; Ivić, M. A.; Avramov, I. Glucose Sensing Using Glucose Oxidase-Glutaraldehyde-Cysteine Modified Gold Electrode. *Int. J. Electrochem. Sci* **2017**, *12*, 5806–5817.

(334) Baranowska, M.; Slota, A. J.; Eravuchira, P. J.; Alba, M.; Formentin, P.; Pallarès, J.; Ferré-Borrull, J.; Marsal, L. F. Protein Attachment to Silane-Functionalized Porous Silicon: A Comparison of Electrostatic and Covalent Attachment. *J. Colloid Interface Sci.* **2015**, *452*, 180–189.

(335) Chuah, Y. J.; Kuddannaya, S.; Lee, M. H. A.; Zhang, Y.; Kang, Y. The Effects of Poly (Dimethylsiloxane) Surface Silanization on the Mesenchymal Stem Cell Fate. *Biomater. Sci.* **2015**, *3* (2), 383–390.

(336) Babaei, M.; Bonakdar, S.; Nasernejad, B. Selective Biofunctionalization of 3D Cell-Imprinted PDMS with Collagen Immobilization for Targeted Cell Attachment. *Sci. Rep.* **2022**, *12* (1), 1–9.

(337) Sharma, S.; Conrad, J. C. Attachment from Flow of Escherichia Coli Bacteria onto Silanized Glass Substrates. *Langmuir* **2014**, *30* (37), 11147–11155.

https://doi.org/10.1021/la502313y.

(338) Mori, S.; Kitta, Y.; Sakamoto, H.; Takamura, E.; Suye, S. Electrochemical Characteristics of a Gold Nanoparticle-Modified Controlled Enzyme–Electrode Contact Junction Electrode. *Biotechnol. Lett.* **2021**, *43* (5), 1037–1042.

(339) Guiseppi-Elie, A.; Lei, C.; Baughman, R. H. Direct Electron Transfer of Glucose Oxidase on Carbon Nanotubes. *Nanotechnology* **2002**, *13* (5), 559.

(340) Schubart, I. W.; Göbel, G.; Lisdat, F. A Pyrroloquinolinequinone-Dependent Glucose Dehydrogenase (PQQ-GDH)-Electrode with Direct Electron Transfer Based on Polyaniline Modified Carbon Nanotubes for Biofuel Cell Application. *Electrochim. Acta* **2012**, *82*, 224–232.

(341) Deore, B.; Sampson, K. L.; Lacelle, T.; Kredentser, N.; Lefebvre, J.; Young, L. S.; Hyland, J.; Amaya, R. E.; Tanha, J.; Malenfant, P. R. L. Direct Printing of Functional 3D Objects Using Polymerization-Induced Phase Separation. *Nat. Commun.* **2021**, *12* (1), 1–12.

(342) Chi, J.; Yu, H. Water Electrolysis Based on Renewable Energy for Hydrogen Production. *Chinese J. Catal.* **2018**, *39* (3), 390–394.

(343) Toghyani, S.; Fakhradini, S.; Afshari, E.; Baniasadi, E.; Jamalabadi, M. Y. A.; Shadloo, M. S. Optimization of Operating Parameters of a Polymer Exchange Membrane Electrolyzer. *Int. J. Hydrogen Energy* **2019**, *44* (13), 6403–6414.

(344) Modak, A.; Bhanja, P.; Dutta, S.; Chowdhury, B.; Bhaumik, A. Catalytic Reduction

of CO 2 into Fuels and Fine Chemicals. *Green Chem.* **2020**, *22* (13), 4002–4033.

(345) Foster, S. L.; Bakovic, S. I. P.; Duda, R. D.; Maheshwari, S.; Milton, R. D.; Minteer, S. D.; Janik, M. J.; Renner, J. N.; Greenlee, L. F. Catalysts for Nitrogen Reduction to Ammonia. *Nat. Catal.* **2018**, *1* (7), 490–500.

(346) Wan, Y.; Xu, J.; Lv, R. Heterogeneous Electrocatalysts Design for Nitrogen Reduction Reaction under Ambient Conditions. *Mater. Today* **2019**, *27*, 69–90.

(347) Lee, J. K.; Lee, C.; Fahy, K. F.; Kim, P. J.; LaManna, J. M.; Baltic, E.; Jacobson, D. L.; Hussey, D. S.; Stiber, S.; Gago, A. S. Spatially Graded Porous Transport Layers for Gas Evolving Electrochemical Energy Conversion: High Performance Polymer Electrolyte Membrane Electrolyzers. *Energy Convers. Manag.* **2020**, *226*, 113545.

(348) De Angelis, S.; Schuler, T.; Charalambous, M. A.; Marone, F.; Schmidt, T. J.; Büchi, F. N. Unraveling Two-Phase Transport in Porous Transport Layer Materials for Polymer Electrolyte Water Electrolysis. *J. Mater. Chem. A* **2021**, *9* (38), 22102–22113.

(349) Ly, T. T.; Ruan, Y.; Du, B.; Jia, P.; Zhang, H. Fibre-Optic Surface Plasmon Resonance Biosensor for Monoclonal Antibody Titer Quantification. *Biosensors* **2021**, *11* (10), 383.

(350) Bathla, P.; Kennedy, J. 3D Printed Structured Porous Treatments for Flow Control around a Circular Cylinder. *Fluids* **2020**, *5* (3), 136.

(351) Domínguez-Bajo, A.; Rosa, J. M.; González-Mayorga, A.; Rodilla, B. L.; Arché-Núñez, A.; Benayas, E.; Ocón, P.; Pérez, L.; Camarero, J.; Miranda, R. Nanostructured Gold Electrodes Promote Neural Maturation and Network Connectivity. *Biomaterials* **2021**, *279*, 121186.

(352) Milton, R. D.; Cai, R.; Abdellaoui, S.; Leech, D.; De Lacey, A. L.; Pita, M.; Minteer, S. D. Bioelectrochemical Haber–Bosch Process: An Ammonia-producing H2/N2 Fuel Cell. *Angew. Chemie Int. Ed.* **2017**, *56* (10), 2680–2683.

(353) Cai, R.; Minteer, S. D. Nitrogenase Bioelectrocatalysis: From Understanding Electron-Transfer Mechanisms to Energy Applications. *ACS Energy Lett.* **2018**, *3* (11), 2736–2742.